Dissertation
submitted to the
Combined Faculties of the Natural Sciences and Mathematics
of the Ruperto-Carola-University of Heidelberg, Germany
for the degree of
Doctor of Natural Sciences

Put forward by
Manuel Gerken
born in: Frankfurt am Main, Germany
Oral examination: Mai 18th, 2022

Exploring p-wave Feshbach Resonances in Ultracold Lithium and Lithium - Cesium Mixtures

Referees: **Prof. Dr. Matthias Weidemüller**
Prof. Dr. Selim Jochim

Abstract

This thesis reports on the exploration of p-wave Feshbach resonances in ultracold ^{6}Li and ^{6}Li-^{133}Cs gases where the pair rotation angular momentum is $l = 1$. An improved experimental apparatus is presented, allowing atom loss spectroscopy with a magnetic field resolutions down to several milli-Gauss on three ^{6}Li and five ^{6}Li-^{133}Cs Feshbach resonances. A doublet structure is observed for the first time on three ^{6}Li p-wave Feshbach resonances. We assign the splittings to spin-spin interactions where the projection of the pair rotation angular momentum m_l splits the resonance into $m_l = 0$ and $|m_l| = 1$. For the first time we report on observation of spin-rotation interaction on three ^{6}Li-^{133}Cs p-wave Feshbach resonances. Here the pair-rotation couples to the atomic spins, leading to an additional splitting of the $m_l = -1$ and $m_l = +1$ projections. Via coupled channel calculations we determine the dimensionless spin rotation constant to be $|\gamma| = 0.566(50) \times 10^{-3}$. With a simple model we show that the strength of spin-rotation coupling depends significantly on the short-range part of the electron wave functions, highlighting the potential of Feshbach resonances to provide precise information on electron and nuclear wave functions at short internuclear distance. In an additional exploratory study of losses close to a single component Fermi p-wave Feshbach resonance we find changes in qualitative loss behavior depending on the density and temperature of the gas. We separate two regimes depending on the dominance of either elastic or inelastic collisions showing three- or two-body loss behavior, respectively. Collisional losses with possible cooling efficiencies similar to classic evaporative cooling are predicted.

Zusammenfassung

Diese Arbeit präsentiert die Untersuchung von p-Wellen Feshbach-Resonanzen in ultrakalten ^{6}Li und ^{6}Li-^{133}Cs Gasen, bei denen der Molekül-Rotationsdrehimpuls $l = 1$ beträgt. Es wird eine Verbesserung des experimentellen Aufbaus vorgestellt, der Atomverlustspektroskopie mit einer Magnetfeldauflösungen bis zu wenigen Milli-Gauß bei drei ^{6}Li und fünf ^{6}Li-^{133}CsFeshbach-Resonanzen ermöglicht. Bei drei ^{6}Li p-Wellen Feshbach-Resonanzen wird zum ersten Mal eine Doppelstruktur beobachtet. Wir führen die Aufspaltung auf Spin-Spin-Wechselwirkungen zurück, wobei die Projektion des Molekül-Rotationsdrehimpulses m_l die Resonanz in $m_l = 0$ und $|m_l| = 1$ aufspaltet. Zum ersten Mal beobachten wir die Spin-Rotations-Wechselwirkung bei drei ^{6}Li-^{133}Cs p-Wellen Feshbach-Resonanzen. Hier koppelt die Molekül-Rotation an die atomaren Spins, was zu einer zusätzlichen Aufspaltung der $m_l = -1$ und $m_l = +1$ Projektionen führt. Mittels einer $Coupled - Channel$ Modellierung bestimmen wir die dimensionslose Spinrotationskonstante $|\gamma| = 0.566(50) \times 10^{-3}$. Anhand eines einfachen Modells zeigen wir, dass die Stärke der Spin-Rotations-Kopplung signifikant von den elektronischen Wellenfunktionen bei kurzem Kernabstand abhängt. Dies hebt das Potenzial der Feshbach-Resonanzen hervor, präzise Informationen über Elektronen- und Kernwellenfunktionen bei kurzem Kernabstand zu erhalten. In einer zusätzlichen explorativen Studie über Verluste in der Nähe eines ein komponentigen Fermi p-Wellen Feshbach-Resonanz, finden wir qualitative Veränderungen im Verlustverhalten in Abhängigkeit von Dichte und Temperatur des Gases. Wir unterscheiden zwei Regime, in denen entweder elastische oder unelastische Stöße dominieren, die ein Drei- bzw. Zweikörper-Verlustverhalten aufzeigen. Kollisionsverluste mit einer mögliche Kühleffizienz ähnlich der klassischen Verdunstungskühlung werden vorhergesagt.

Parts of this thesis are based on the following manuscripts and publications:

- **Observation of dipolar splittings in high-resolution atom-loss spectroscopy of ^{6}Li p-wave Feshbach resonances**
  M. Gerken, B. Tran, S. Häfner, E. Tiemann, B. Zhu, M. Weidemüller
  Physical Review A **100**, 050701(R) (2019)

- **Observation of spin-rotation coupling in p-wave Feshbach resonances**
  B. Zhu, S. Häfner, B. Tran, M. Gerken, J. Ulmanis, E. Tiemann, M. Weidemüller
  Manuscript in preparation

- **Qualitative change in loss behavior in single component Fermi gases close to p-wave Feshbach resonances**
  M. Gerken, K. Welz, B. Zhu, B. Tran, E. Lippi, L. Chomaz, M. Weidemüller
  Manuscript in preparation

Furthermore, the author contributed to the following publications:

- **Scattering of two heavy Fermi polarons: resonances and quasibound states**
  T. Enss, B. Tran, M. Rautenberg, M. Gerken, E. Lippi, M. Drescher, B. Zhu, M. Weidemüller, M. Salmhofer
  Physical Review A **102**, 063321 (2020)

- **Fermions meet two bosons – the heteronuclear Efimov effect revisited**
  B. Tran, M. Rautenberg, M. Gerken, E. Lippi, B. Zhu, J. Ulmanis, M. Drescher, M. Salmhofer, T. Enss, M. Weidemüller
  Brazilian Journal of Physics **51**, 316–322 (2021)

Contents

Introduction

Discriminating physical regimes is at the core of progress and understanding in physics as a natural science. Ultracold gases have proven to provide an excellent platform for the exploration of the most diverse physical regimes. From the measurement of the gravitational red-shift [Bothwell et al., 2022] to the simulation of vacuum fluctuations by phononic excitations in a Bose-Einstein-Condensate (BEC) [Rentrop et al., 2016], ultracold gases access regimes through control of almost every relevant physical parameter such as dimensions, temperature, densities and interactions under high isolation from the environment [Bloch et al., 2008].

Feshbach resonances have been one of the most striking and productive features in ultracold gases [Chin et al., 2010]. Named after Hermann Feshbach for the development of a theory for resonant scattering in nuclear physics [Feshbach, 1958] and introduced to quantum gases by Inouye et al. [1998] and Courteille et al. [1998], this tool allows the control of inter-particle interactions. By changing the relative energy of the scattering state in an open channel and a bound molecular state in a closed channel, the scattering phase shift can be changed giving complete control over the inter-atomic interactions. Tuning the relative energy is either possible via optical coupling [Fedichev et al., 1996; Theis et al., 2004; Cetina et al., 2016], change in scattering energy [Boesten et al., 1997; DeMarco et al., 1999] or by exploiting the different magnetic moments of the channels by applying a magnetic field [Moerdijk et al., 1995].

In broad s-wave Feshbach resonances, scattering of two colliding atoms with relative angular momentum $l = 0$, the scattering length a fully describes the phase shift of the scattering wave [Chin et al., 2010]. A series of success stories originate from the magnetic control of scattering in the universal regime where a is the only relevant length scale of the system. The production of a BEC of weakly bound dimers of Fermi atoms with size $a/2$ was achieved for positive a [Jochim et al., 2003; Zwierlein et al., 2003; Greiner et al., 2003]. Later, the understanding of the BEC-BCS crossover would be one of the greatest achievements in ultracold gases [Bartenstein et al., 2004; Kinast et al., 2004; Chin et al., 2004; Partridge et al., 2005; Zwierlein et al., 2005]. A continuous change of bound dimers on the positive side of the Feshbach resonance to Cooper pairs on the negative side of the resonance allowed deep insights into pairing mechanisms. Different progress has been made in few-body physics where three particles form the famous Efimov states, an infinite series of resonant three-body bound states of size λa, where λ is a universal scaling parameter [Naidon and Endo, 2017]. These states have been observed in a series

of different systems and lead to precise investigations of the universal regime [Kraemer et al., 2006; Lompe et al., 2010; Berninger et al., 2011; Ulmanis et al., 2016; Johansen et al., 2017]. Also the creation of Feshbach molecules has been studied in great detail [Wu et al., 2012; Heo et al., 2012; Cumby et al., 2013; Köppinger et al., 2014; Wang et al., 2015]. They proved to be beneficial for the study of chemical reactions, where the reaction energy can be changed from exothermic to endothermic by preparing particular molecular states [Ye et al., 2018; Hoffmann et al., 2018]. Feshbach molecules are also used as the first step in the production of molecules in the electronic and vibrational ground state via stimulated adiabatic Raman sideband passage [Ni et al., 2008; Molony et al., 2014; Takekoshi et al., 2014; Park et al., 2015; Guo et al., 2016]. Feshbach resonances were also used to probe many-body physics in the polaron scenario, where single impurities are immersed in a Fermi sea (Fermi polaron) or BEC (Bose polaron) simulating the famous "Fröhlich polaron" problem [Fröhlich, 1954; Kohstall et al., 2012; Hu et al., 2016; Cetina et al., 2016; Jørgensen et al., 2016; Yan et al., 2020; Fritsche et al., 2021].

In narrow s-wave Feshbach resonances another length scale comes into play. If the effective range $1/k_e$, describing the effective length scale of the inter atomic potential, becomes comparable to the thermal de Brogli wavelength of the atoms, the scattering process can no longer be described in terms of only the scattering length a and the universal regime breaks down [Gurarie and Radzihovsky, 2007; Johansen et al., 2017]. While narrow resonances are of large interest to theory due to the validity of simple two channel models [Gurarie and Radzihovsky, 2007], the resonances are difficult to exploit experimentally, compared to broad resonances, due to large losses accompanying strong interactions [Li et al., 2018]. Nevertheless, a few studies have been performed close to narrow ^{6}Li s-wave resonance at 542 G where Hazlett et al. [2012]; Wang et al. [2013] studied losses and the breakdown of universality. In another recent study losses near the resonances has been used to cool atomic samples via recombinational cooling [Peng et al., 2021].

Broad and narrow s-wave Feshbach resonances have been characterized, studied and exploited in great detail in ultracold ^{6}Li-^{133}Cs systems. Observation through atom loss spectroscopy, thermalization through elastic collisions, detailed analysis using different theoretical models and radio frequency association of Feshbach dimers lead to very accurate determination of the resonance poles, positions and resonance widths Repp et al. [2013]; Tung et al. [2013]; Pires et al. [2014a]; Ulmanis et al. [2015]; Johansen et al. [2017]. With the help of these measurements, the long range part of these interaction potentials were accurately determined Repp et al. [2013]; Ulmanis et al. [2015]. The precise characterization of the resonances was used for detailed studies of aforementioned Efimov resonances, of special interest in high mass-imbalanced systems due to a small scaling factor λ Tung et al. [2014]; Pires et al. [2014b]; Ulmanis [2017]. Furthermore, Johansen et al. [2017] performed investigations of van der Waals universality comparing the Efimov states at Feshbach resonances with different widths. In another study it was shown that the ^{6}Li-^{133}Cs interactions lead to a shift in the ^{133}Cs-^{133}Cs interactions and that the interspecies interaction could be used to trap ^{6}Li within a ^{133}Cs BEC [DeSalvo et al., 2017, 2019].

In p-wave Feshbach resonances the relative angular momentum of the colliding atoms is $l = 1$. These resonances are usually of narrow nature due to the centrifugal barrier of the interacting potential [Gurarie and Radzihovsky, 2007]. In single component Fermi gases s-wave interactions are suppressed due to Pauli blocking, making p-wave scattering the dominant interaction process [DeMarco et al., 1999]. This makes strongly interacting p-wave gases especially interesting for single component Fermi gases. For example the enriched phase diagram in the superfluid phase [Gurarie et al., 2005] plays an essential role inside neutron stars [Page et al., 2011; Shternin et al., 2011]. A Fermi polaron close to a p-wave resonance is also expected to show a more complex state structure compared to the s-wave case [Levinsen et al., 2012]. Efimov states, however do not exist for $l = 1$ resonances [Nishida, 2012]. As for narrow s-wave resonances, p-wave resonances are accompanied by large losses making their exploitation difficult and scarce to date.

Nevertheless, p-wave Feshbach resonances have been observed and studied in different ultracold gas systems DeMarco et al. [1999]; Regal et al. [2003]; Zhang et al. [2004]; Dong et al. [2016]. Next to studies surrounding p-wave Feshbach molecules [Gaebler et al., 2007; Waseem et al., 2016; Zhou and Cui, 2017; Bazak and Petrov, 2018; Duda et al., 2022], loss processes and scaling laws were studied extensively [Regal et al., 2003; Zhang et al., 2004; Schunck et al., 2005; Waseem et al., 2017]. Especially single component Fermi gases in the hyperfine ground state are of special interest due to suppression of two-body losses [Waseem et al., 2018; Yoshida et al., 2018; Waseem et al., 2019]. Confinement to less than three spatial dimensions also leads to a reduction of losses [Günter et al., 2005; Marcum et al., 2020]. The contact relation was investigated by [Luciuk et al., 2016] showing universal behavior close to a p-wave resonance. Ticknor et al. [2004] observed a multiplet structure of the p-wave resonance in ultracold ^{40}K attributed to spin-spin interactions. The molecular state inducing the resonance carries the $l = 1$ angular momentum as a molecular rotation and the projection of the rotation onto the magnetic field leads to the splitting of the $m_l = 0$, $m_l = \pm, 1$ allowing individual control of the different rotational projections.

This thesis reports on the exploration of p-wave Feshbach resonances in ultracold ^{6}Li and ^{6}Li-^{133}Cs gases. An improved experimental apparatus is presented, allowing atom loss spectroscopy with resolutions down to several milli-Gauss on three ^{6}Li and five ^{6}Li-^{133}Cs Feshbach resonances. A doublet structure, that we assign to spin-spin interactions, is observed for the first time on three ^{6}Li p-wave Feshbach resonances. For the first time we report on the observation of spin-rotation interaction on three ^{6}Li-^{133}Cs p-wave Feshbach resonances. Here, the pair-rotation couples to the atomic spins, leading to an additional splitting of the $m_l = -1$ and $m_l = +1$ projections. With a simple model we show that the strength of spin-rotation coupling depends significantly on the short range part of the electronic wave functions. In an exploratory study of losses close to a single component Fermi p-wave Feshbach resonance we find changes in qualitative loss behavior depending on the density and temperature of the gas. We describe collisional cooling due to three-body losses or out of equilibrium momentum distributions due to two-body loss behavior.

This thesis is divided into two parts. In the first part we focus on the presentation of the improved experimental preparation and characterization of ultracold ^{6}Li and ^{6}Li-^{133}Cs samples for the investigation of p-wave Feshbach resonances. Chapter 1 gives an overview of the experimental apparatus starting from the vacuum system and the magnetic field creation, describing also the optical cooling and trapping techniques and conclude with the radio-frequency system and the absorption imaging for detection. Chapter 2 presents the experimental sequence and characterization of the improved creation of a degenerate ^{6}Li sample. Additionally, details of the experimental sequence for the creation of an ultracold ^{6}Li-^{133}Cs mixture are given. Chapter 3 discusses the improved calibration of the magnetic field landscape, essential for the high precision measurements in the vicinity of the p-wave resonances. In the second part of the thesis we present the exploration of ^{6}Li and ^{6}Li-^{133}Cs p-wave Feshbach resonances. After an introduction into atomic collision, containing the basics of scattering and Feshbach resonances in chapter 4, we present our findings on spin-spin interactions in ^{6}Li and ^{6}Li-^{133}Cs resonances and their temperature dependence in chapter 5. Chapter 6 reports on the measurements of spin-rotation splitting on three ^{6}Li-^{133}Cs p-wave Feshbach resonances and their temperature dependence. A simple model, estimating the spin-rotation coupling constant γ is presented. In the last chapter 7 we present the exploratory study of losses in a single component Fermi gas in the hyperfine ground state.

Part I

An Improved Experimental Lithium-Cesium Platform

1. Experimental Apparatus

Before going into details of the improved setup we give an introduction to the basic experimental apparatus used for the preparation of the ultracold Lithium and Lithium-Cesium samples. Parts of the experimental setup have been described previously in Repp [2013]; Pires [2014]; Ulmanis [2017]; Häfner [2017]. Figure 1.1 shows a modular overview of the experimental apparatus. The system is separated into six (almost) independent sub-systems which are the vacuum system, magnetic field coils, optical cooling systems, systems for optical trapping, radio-frequency systems and the detection system. Each of the modules consist of further sub-systems that are presented in the following sections. Parts of the experimental apparatus that are not included here are environment systems such as room temperature stabilization, water cooling or control systems such as experimental control and experimental monitoring systems. In the following description we follow the route of the atoms from the hot oven at several hundreds of K to the detection at several hundreds of nK.

1.1 Vacuum System

Figure 1.2 shows an overview of the vacuum chamber of the Lithium-Cesium experiment.

The double species oven is the first part of the vacuum system. It follows a similar design as used in Stan and Ketterle [2005] and is shown in figure 1.2 as (a). It is used for the creation of two atomic beams. Despite the large difference in vapor pressure for both species [Gehm, 2003; Steck, 2002] we achieve separat control over the atomic flux by operating the two different oven chambers containing the different species at different temperatures. Typically temperatures are $T_{Li} = 635\,\mathrm{K}$ and $T_{Cs} = 375\,\mathrm{K}$. The atomic beams leave the oven through a nozzle with a diameter of 10 mm. Due to the large mass difference between ^{6}Li and ^{133}Cs and the two operation temperatures this results in atomic fluxes of $\Phi_{Li} = 5 \times 10^{15}\mathrm{atomss}^{-1}$ and $\Phi_{Cs} = 1 \times 10^{14}\mathrm{atomss}^{-1}$ and mean atomic velocities of $\bar{v}_{Li} = 1600\,\mathrm{m\,s}^{-1}$ and $\bar{v}_{Cs} = 250\,\mathrm{m\,s}^{-1}$. The pressure in the oven region is approximately $p \approx 1 \times 10^{-3}$mbar and is maintained by a turbo molecular pump. The oven chamber is followed by a differential pumping stage consisting of a 103 mm long tube with a diameter of 7 mm, directly connected to an ion getter pump (IGP).

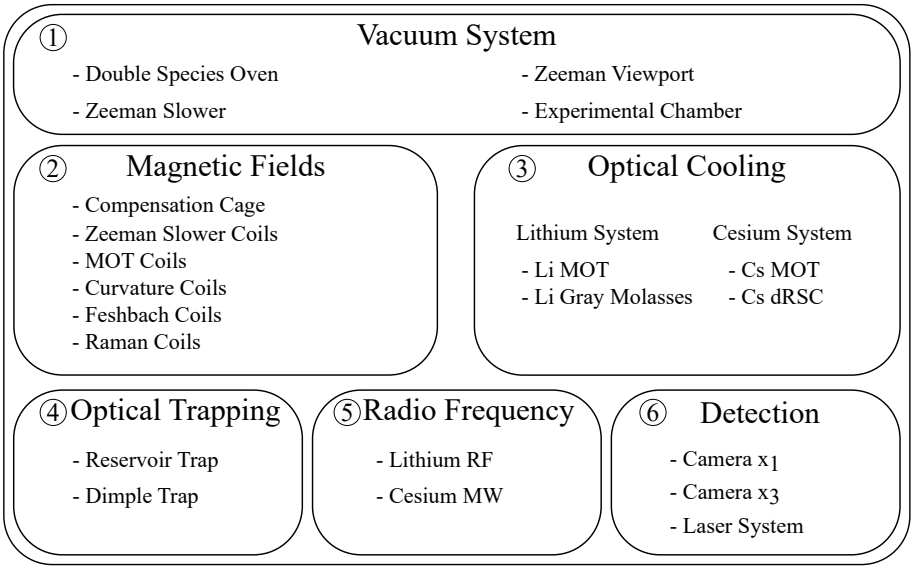

Figure 1.1: Modular overview of the experimental apparatus presented in the following sections: the Vacuum system (1), the magnetic field coils (2), the systems for optical cooling of ^{6}Li and ^{133}Cs (3), the optical dipole trapping laser systems (4), the radio-frequency systems for ^{6}Li and ^{133}Cs spin flips (5) and the detection systems for absorption imaging at low and high magnetic field (6).

The Zeeman slower follows the differential pumping stage and is effectively another differential pumping stage of a length of a 500 mm at a diameter of 10 mm ((b) in figure 1.2). It additionally consists of magnetic field coils and optical light explained in sections 1.2 and section 1.3.

The experimental chamber is the heart of the experiment and follows the Zeeman slower. In figure 1.2 it is marked as (c). Due to the two differential pumping stages between oven and experimental chamber, we are able to hold a difference in pressure of more than five orders of magnitude. An Ion getter pump (IGP), a Titanium Sublimation pump (TiSub) and a non-evaporable getter coating [Benvenuti et al., 1999] hold a pressure as low as 10^{-11}mbar. Optical access to the center of the experimental chamber is provided via four CF63 and two CF40 viewports in horizontal direction at a distance of ∼130 mm from the center. In vertical direction two custom made CF150 reentrant viewports are placed ∼19.5 mm away from the center. This allows for large NA optical access and for magnetic coil placement close to the atoms for the generation of large magnetic fields. All viewports are anti-reflection coated at the wavelength of ^{6}Li (670 nm), ^{133}Cs (852 nm) and the wavelength of common optical dipole traps (1064 nm). Suprasil 3001 glass is used for the viewports to minimize infrared light absorption.

The slower viewport closes the vacuum system ((d) in figure 1.2). It grants optical access to the Zeeman slower. To minimize viewport coating by the atomic beam that is directed directly at the viewport, the window is heated to temperatures of 485 K.

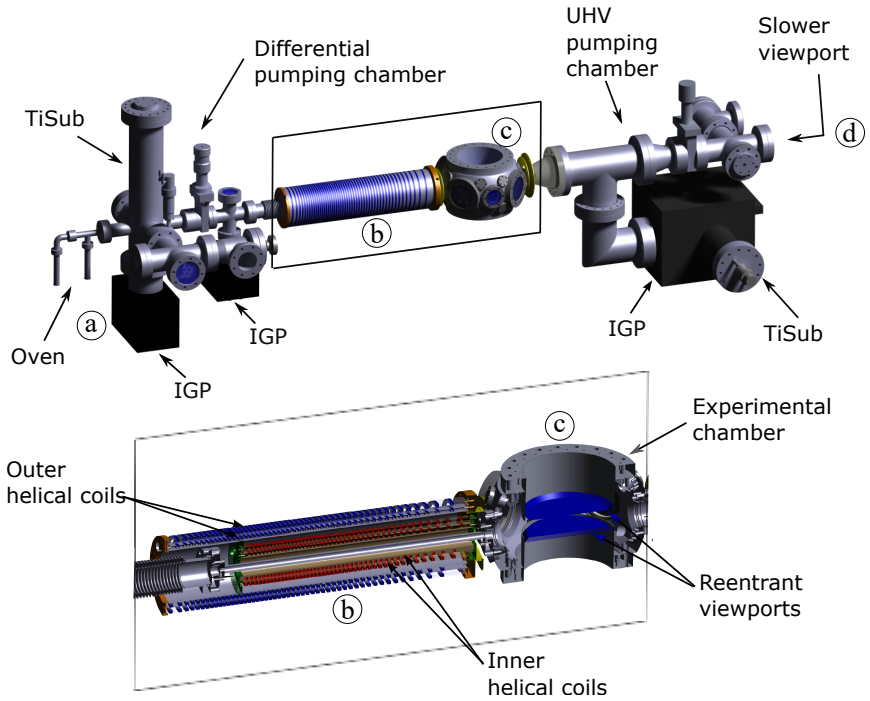

Figure 1.2: Overview of the vacuum system of the ^{6}Li-^{133}Cs experiment. The upper panel shows the whole vacuum system. (Starting from the left) First the double species oven including an Ion-getter-pump (IGP) and a Titanium Sublimation pump (TiSub) (a) followed by a differential pumping stage and another IGP separating the oven vacuum from the high vacuum. Then comes the Zeeman slower (b) that also acts as a differential pumping stage. The experimental chamber (c) is the heart of the experiment with optical access from eight viewports. On the right side of the chamber a set of IGP and TiSub pumps generate the ultra high vacuum with pressures of 10^{-11}mbar. They are followed by the Slower viewport (d). The lower panel shows a cross section of the Zeeman slower including the four different coils and the experimental chamber with the reentrant viewports close to the chamber center. Picture adapted from Repp [2013].

Overall the vacuum system allows for the generation of a ^{6}Li and ^{133}Cs atomic beam into an experimental chamber at a pressure of 10^{-11}mbar with very good optical access and large magnetic fields.

1.2 Magnetic Fields

Besides optical control of atoms, we also use magnetic fields to control the atomic samples. A detailed discussion of the impact of magnetic fields on atoms is given in chapter 3. Here we introduce the magnetic field coils in our experiment that are used for Zeeman deceleration, magneto-optical trapping, magnetic field compensation, Raman sideband cooling of ^{133}Cs and scattering control via Feshbach resonances (see chapter 4.2). The most important coils are depicted in figure 1.3.

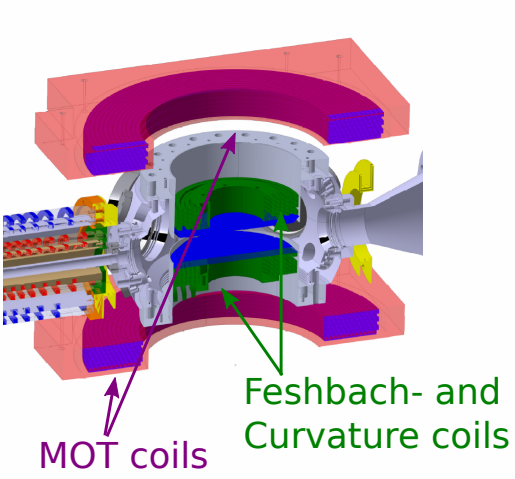

Figure 1.3: Feshbach- and MOT-coil setup around experimental chamber. The MOT coils are located far away from the experimental chamber. The Feshbach coils and the curvature coils are situated as close as possible to the center of the vacuum chamber at a distance of 31.5 mm from the center. Switching times for the MOT coils are >10 ms, for the Feshbach coils ∼1 ms and for the curvature coils ∼1 ms. Picture adapted from Repp [2013].

The Zeeman slower coils are a set of four interleaved helical coils that are situated around the 1 m long Zeeman slower tube shown in the lower part of figure 1.2. Their purpose is the generation of magnetic gradients along the tube for either ^{6}Li or ^{133}Cs to provide an deceleration scheme as used in a Zeeman slower [Phillips and Metcalf, 1982]. A detailed description of our double species Zeeman slower is given in [Repp, 2013]. The principle works as follows: the Doppler shift on an atomic resonance frequency is compensated by the Zeeman shift of the magnetic field inside the Zeeman slower such that the applied optical beam along the slower is at resonance with the atomic resonance frequency. The optical pressure leads to slowing of the atoms and the decreasing magnetic field induced Zeeman shift leads again to a precise compensation of the Doppler shift. Thus the atoms are slowed along the Zeeman slower until they reach the center of the experimental chamber. The ideal magnetic field profile between ^{6}Li and ^{133}Cs differs by a factor 4.7 Repp [2013]. This is provided by our double species Zeeman slower following the design of Bell et al. [2010]. An additional adaption coil generates a smooth transition from the Zeeman slower to the magnetic gradient field of the Magneto-Optical-Trap (MOT) coils to minimize transversal expansion of the atomic beam [Schünemann et al., 1998]. The whole Zeeman slower coil system is water cooled to optimize heat dissipation.

The compensation cage is used for the compensation of the earth magnetic field and other external magnetic fields from outside the experimental system. The cage consists of three pairs of coils situated in the three spatial dimensions around the experimental chamber. A coil consists of a rectangle with dimensions of 800mm×1380mm×660mm. The vertical coils consist of 100 windings and the horizontal coil pairs consist of 100 and 150

windings. The coil pairs can each provide magnetic fields at the center of the experimental chamber of up to 2 G. The calibration of this cage is discussed in chapter 3.3. The fields are only changed following a new calibration which are preformed approximately every half year.

The MOT coils generate a quadrupole field for the MOT and can be seen in figure 1.3 in red. The pair of coils consist of 6 layers of 12 windings with a minimal radius of 100 mm at a distance of 204 mm from each other around the center of the experimental chamber. They are setup in an anti-Helmholtz configuration providing gradients of $\partial B_{Cs}/\partial z = 9.5\,\mathrm{G\,cm^{-1}}$ and $\partial B_{Li}/\partial z = 31\,\mathrm{G\,cm^{-1}}$ at currents of $I_{Cs} = 30\mathrm{A}$ and $I_{Li} = 97.7\mathrm{A}$ for the ^{133}Cs- and ^{6}Li-MOT respectively. Additionally the gradient provided by the MOT coils leads to a smooth Zeeman deceleration from the Zeeman slower up to the center of the experimental chamber. The MOT coils are also cooled by water flowing through the hollow core wire to minimize heating. Due to the large size of the coil pair and the large inductance, the switching times of the MOT coils are limited to $> 10\,\mathrm{ms}$. This large switching time is problematic for applications like gray molasses cooling of ^{6}Li. Repp [2013] provides more details on the implementation of the MOT coils.

The Curvature coils are another set of anti-Helmholtz coils generating magnetic quadrupole fields around the center of the experimental chamber of up to $\partial B/\partial z = 100\,\mathrm{G\,cm^{-1}}$. They consist of two layers with two windings and are both placed within the Feshbach coils (see below and figure 1.3) at a distance of 63 mm from each other. The low inductance leads to fast switching times of $1 - 2\,\mathrm{ms}$. After loading the MOT using the MOT coils, the atoms are transfered to the quadrupole field provided by the curvature coils to effectively switch the quadrupole field before cooling ^{6}Li with gray molasses cooling or ^{133}Cs with degenerate Raman sideband cooling (dRSC).

The Feshbach coils provide large magnetic fields of up to 1200 G at the center of the experimental chamber for the control of intra- and interspecies scattering length via Feshbach resonances (see chapter 4.2). Figure 1.3 shows the configuration of the Feshbach coils as implemented in the experiment. The coils are placed inside the recess of the reentrant viewports. Both coils consist of 24 windings, 4 windings in axial directions and 6 in radial direction with a minimal inner radius of 39.1 mm. The distance from the center of the chamber and the coils is 31.5 mm. The helix configuration and the point symmetric configuration of both coils assures a homogeneous field in the center of the coil setup. Distance of 5 mm between the windings provide space for glass fiber tubes for water cooling. The profiles of the inner coils are milled into a peek mount with a CNC milling machine to provide maximal precision and consistency. The outer layers are milled into a low viscosity epoxy used to glue the wire. Heat is dissipated by water cooling using an industrial water cooler pumping water at 10 bar through a hollow core wire with a round inner hole of 2.8 mm inner diameter and a quadratic cross section of $4\,\mathrm{mm} \times 4\,\mathrm{mm}$. The temperature is stabilized to $\Delta T < 0.3\,\mathrm{K}$. This reduces changes in resulting resistance

and thermal expansion which would lead to changes in the magnetic field. A Delta SM 15-400 power supply creates currents up to 400 A at voltages up to 15 V. A current transducer (Ultrastab 866 Precision Current Transducer) is used to monitor and stabilize the actual current using a PID feedback loop. We use MOSFET switches for fast switching of the current. To reach maximal magnetic field stability an experimental sequence with a certain magnetic field function needs to be constantly repeated for roughly 12 h. Then a thermal equilibrium is reached within that experimental sequence. The experimental control system is running on a 16bit channel limiting the magnetic field control resolution to ≈ 20 mG. The precise calibration of the magnetic field and the magnetic field landscape around the center is presented in chapter 3.

The Raman coils and offset coils are three sets of coils arranged in Helmholtz configuration in three spatial directions. They are used to generate small homogeneous magnetic offset fields to either displace the center of gradient fields (displace the MOT cloud), generate a field for degenerate Raman sideband cooling or to add experimental resolution to the Feshbach field. Placed either around the CF63 viewports or the CF150 viewports of the main chamber the coil pairs generate fields of $150-300\text{mG A}^{-1}$ at switching times of $1-2$ms. The coil pair mounted in vertical direction can provide magnetic fields of $\pm$2G with theoretical resolutions of 0.2mG. This is used to provide an increase in magnetic field resolution used for atom loss spectroscopy of part II of this thesis.

1.3 Optical Cooling

In this section we present the optical cooling used on ^{6}Li and ^{133}Cs during the preparation of ultracold ^{6}Li and ^{6}Li-^{133}Cs mixtures. MOT cooling methods are standard methods that can be found in several books [Foot, 2005; Weidemüller and Zimmermann, 2003]. A more detailed description of the setup and the laser systems can be found in Repp [2013]; Pires [2014] and Häfner [2017].

Optical cooling for ^{6}Li and ^{133}Cs is performed in different stages. First stage is the deacceleration in the Zeeman slower. The hot atoms emitted by the effusive oven (see section 1.1) are decelerated by a combination of a gradient magnetic field (see section 1.2) and red detuned light on the D2-line for both species (marked at "Li+Cs Slower" in figure 1.4). After the slowing of the fast atoms, the atoms are trapped in the MOT consisting of a magnetic quadrupole field (see section 1.2) and three counter propagating beams in σ^+ and σ^- polarization for each species. In figure 1.4 these beams are called "Li MOT" and "Cs MOT" beams. Beams are coupled out in linear polarization from Schäfter+Kirchhoff fiber couplers and pass through quarter-wave plates (green elements in figure 1.4) to generate the circular polarized light. Lithium beams are retroflected in all three dimensions. Cesium beams are generated by six fiber couplers. Temperatures in the MOT reach approximately $T_{Li} = 300\,\mu$K and $T_{Cs} = 10\,\mu$K. Due to the non resolved hyperfine structure in ^{6}Li red detuned MOT light does not lead to sub-Doppler cooling.

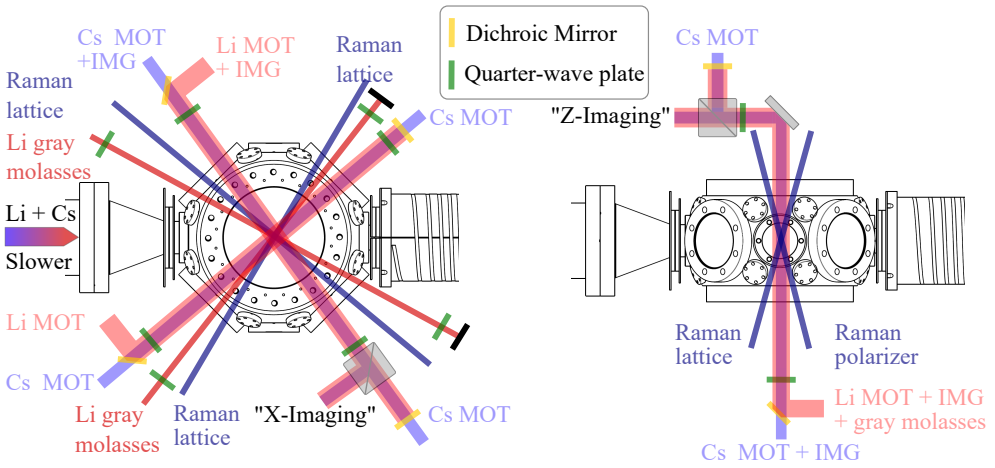

Figure 1.4: Overview over optical cooling beams at the experimental chamber. Left side shows the top view, right side shows the side view. Red beams belong to the ^{6}Li setup, blue beams belong to the ^{133}Cs setup. ^{6}Li cooling consists of a Zeeman cooling beam, Doppler cooling (broad red beams), gray molasses cooling (small dark red beams) and imaging beams (overlapped with Doppler cooling beams). ^{133}Cs cooling consists of Zeeman cooling beam, Doppler cooling (broad blue beams), Raman lattice and polarizer beams (small dark blue beams) and imaging beams (overlapped with Doppler cooling beams). Picture adapted from Repp [2013].

However, for ^{133}Cs the red detuned MOT light cools the atoms below the Doppler limit [Lett et al., 1988].

Gray molasses cooling on ^{6}Li is used to cool the atoms down to 40 µK within a few ms. The working principle, implementation and characterization are presented in chapter 2.1.

Degenerate Raman sideband cooling on ^{133}Cs leads to cooling down to the recoil temperature. The setup follows Kerman et al. [2000]; Treutlein et al. [2001]. An optical lattice consisting of three beams (see figure 1.4) detuned by 9 GHz from resonance is used to confine the atoms. The different total angular momentum projections m_f of the ^{133}Cs ground state atoms are shifted via a small magnetic field on the order of 100 mG such that the Zeeman shift equals the trapping frequency of the optical lattice. By applying a Raman polarizer, the atoms are pumped into the lowest vibrational state of the $m_f = 3$ state. We reach spin polarizations in the $m_f = 3$ state of 85% at temperatures below 1 µK. Details are given in Repp [2013].

Finally the setup is used for atom imaging (see section 1.6) in x_1- and in x_3- direction. Imaging beams are separated from MOT beams via polarizing beam splitters. After optical cooling we end up with approximately $N_{Li} = 4 \times 10^7$ ^{6}Li atoms and $N_{Cs} = 4 \times 10^7$ ^{133}Cs at temperatures of $T_{Li} = 40$ µK and $T_{Cs} = 1$ µK.

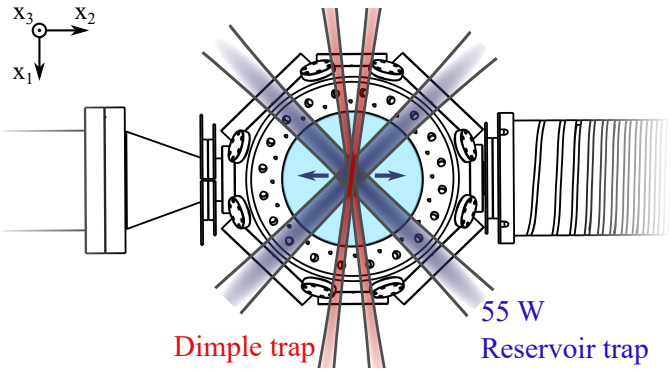

Figure 1.5: Experimental chamber and optical dipole traps in the ^{6}Li-^{133}Cs experiment from top view. The Dimple trap (red) has two 60 µm beams overlapped at an angle of 8° and a power of up to 120 W. The Reservoir trap (blue) has two 300 µm beams intersecting at 90° with a power of up to 55 W. It can be moved by 1 mm using a Piezo mirror. Picture adapted from Repp [2013].

1.4 Optical Trapping

Optical dipole traps are essential tools in ultracold atom experiments [Grimm et al., 2000]. Strong optical fields induce electric dipole moments in neutral atoms which retroactively interacts with the optical field. The electric dipole $\tilde{p}$ of an atom through induced by an AC-light field $\tilde{E}$ is given by $\tilde{p} = \alpha(\lambda)\tilde{E}$ where $\alpha(\lambda)$ is the polarizability leading to the potential

$$U_{dip} = -\frac{1}{2\epsilon_0 c}\,\mathrm{Re}(\alpha(\lambda))I \tag{1.1}$$

where $I = 2\epsilon_0 c|\tilde{E}|^2$ is the intensity of the light field, ϵ_0 the vacuum permittivity and c the speed of light.The polarizability $\alpha(\lambda)$ is species, state, wavelength and polarization dependent, however the effects of state and polarization dependence are neglected here. The potential now only depends on the wavelength λ and the light field $I(\vec{r})$, where $\vec{r} = (x_1, x_2, x_3)$. For a Gaussian beam propagating in x_1 direction with power P and beam waist w, the intensity distribution $I(\vec{r})$ is given by

$$I(\vec{r}) = \frac{2P}{\pi w(x_1)^2}\exp\left(-\frac{2x_2^2}{w(x_1)^2}\right)\exp\left(-\frac{2x_3^2}{w(x_1)^2}\right) \tag{1.2}$$

where $w(x_1) = w_0(1+(\frac{\lambda x_1}{\pi w_0^2})^2)^{1/2}$ is the beam waist along the beam and w_0 is the beam waist at the focus. For a crossed beam trap with an angle β between the two beams, the trap depth is given by

$$U_0 = -\frac{P\,\mathrm{Re}(\alpha(\lambda))}{\pi\epsilon_0 c w_0^2} \tag{1.3}$$

Writing the potential in a harmonic approximation as $U_{dip}(\vec{r}) = 1/2m\sum_{i=1}^{3}\omega_{x_i}^2 x_i^2$, where m is the mass and ω_{x_i} is the trapping frequency gives the trapping frequencies

$$\omega_{x_1} = \sqrt{\frac{4\cos(\beta/2)^2 U_0}{m w_0^2}} \qquad \omega_{x_2} = \sqrt{\frac{4\sin(\beta/2)^2 U_0}{m w_0^2}} \qquad \omega_{x_3} = \sqrt{\frac{4U_0}{m w_0^2}} \tag{1.4}$$

In the experiment we use two different dipole traps, both at a wavelength of 1064 nm. Both traps are presented in detail in Pires [2014]; Ulmanis [2017] and Häfner [2017]. The trap geometries are shown in figure 1.5.

The Reservoir trap is shown in blue in figure 1.5. Its purpose is to load the optically cooled ^{133}Cs into the trap and to act as a reservoir during the dimple trick. The two beams intersect at 90° and the focus beam waist is 300 µm at a maximal power of 55 W. The trap can be moved by 1 mm while it is loaded with ^{133}Cs atoms using a Piezo mirror. This mechanism is used to overlap ^{6}Li and ^{133}Cs.

The Dimple trap consists of two beams intersecting at an angle of 8.4° and with a focus beam waist of 60 µm and a maximal power of 120 W. The trap fulfills the task of loading the optically cooled ^{6}Li into the trap and to act as a dimple trick for ^{133}Cs [Pinkse et al., 1997; Stamper-Kurn et al., 1998]. In section 2.2 we discuss spatial modulation of the Dimple trap for enhanced loading of ^{6}Li.

1.5 Radio-frequency

Radio-frequency signals can be used for population control of hyperfine states, radio-frequency spectroscopy [Ulmanis et al., 2015] or magnetic field calibration [Häfner, 2017]. Here we introduce the ^{6}Li radio-frequency (rf) and ^{133}Cs microwave (mw) systems. In chapter 3 we go deeper into details and present magnetic field calibrations by driving splin flip transitions using the following setups:

The ^{6}Li radio-frequency setup is used for the creation of frequencies between 10 MHz and 80 MHz. The setup is explained in detail in Häfner [2017]. The rf signal is generated by an Agilent E4421B signal generator. The signal shape can be formed by mixing the rf signal with an external pulse shape. An interlock protects the rf antenna, situated inside the vacuum, from overheating (see [Filzinger, 2018]). A ZHL-100W-52+ amplifier from Mini Circuits creates rf powers up to 100 W.

The ^{133}Cs microwave setup is used for the creation of frequencies between 9 GHz and 13 GHz. The mw signal is generated by a Rohde & Schwarz SMA100B signal generator and amplified by a ZVE-3W-183+ Mini Circuits amplifier. A WR90 horn antenna from Tactron Elektronik with a 15 dB gain is used as output.

Both signal sources are referenced to an SRS FS725 — 10 MHz Rb frequency standard for long term stabilization.

1.6 Detection

Absorption imaging techniques are a common tool to extract information about the atomic clouds [Ketterle et al., 1999]. By shining resonant light onto the atoms and recording the absorbed light with a CCD camera the atom number, the atomic distribution and the sample temperature can be reconstructed. Here we give an overview on the detection method and our detection setup.

When shining resonant light onto an atomic cloud and recording the light intensity on a CCD ship one gets an intensity distribution $I_{abs}(x_1, x_2)$ called absorption image. Recording a second picture without the atoms leads to the so called division picture $I_{div}(x_1, x_2)$. A final picture without light gives a background picture $I_{bac}(x_1, x_2)$. Using Beer's law $I(x_3) = I_0 \exp(-\sigma x_3)$ where I_0 is the initial light intensity, σ is the absorption cross section and x_3 is the direction of the light beam, we can reconstruct the initial atomic column density distribution $n(x_1, x_2) = \int n(x_1, x_2, x_3) dx_3$ in the direction of the incident light with

$$n(x_1, x_2) = -\frac{1}{\sigma} \ln \left(\frac{I_{abs}(x_1, x_2) - I_{bac}(x_1, x_2)}{I_{div}(x_1, x_2) - I_{bac}(x_1, x_2)} \right) \tag{1.5}$$

By fitting a two dimensional Gaussian function to the column density distribution we extract the atom number N and the cloud sizes σ_{x_1} and σ_{x_2} from the absorption image. By studying the ballistic expansion of the cloud after release from a trap, we also extract the temperature T of the system via

$$T = \frac{m}{k_B t^2} (\sigma(t)^2 - \sigma(t=0)^2) \tag{1.6}$$

where t is the time after the release of the atoms from the trap called time of flight (tof), $\sigma(t)$ is the cloud size at time t, m is the atomic mass and k_B is the Boltzmann constant.

The setup of the imaging system in our experiment can be found in Repp [2013]; Pires [2014] and Häfner [2017].

Cameras x_1 and x_3 allow for absorption imaging in x_1 and x_3 direction (see figure 1.4) enabling access to all the spatial dimensions of the atomic cloud. Additionally this allows for simultaneous imaging of ^{6}Li and ^{133}Cs.

The laser systems create resonant light for both species at magnetic fields from 0 G up to 1200 G allowing for high-field imaging. The setups are explained in detail in Heck [2012]; Schönhals [2013].

Since resonant light is destructive for a trapped atomic cloud, we also use the imaging light for the cleaning of single ^{6}Li spin states by applying a short light pulse on resonance of the desired spin state.

2. Improved Cooling and Trapping of Lithium and Lithium-Cesium

In this chapter we describe an improved production of a degenerate ^{6}Li sample and the preparation sequence for an ultracold ^{6}Li-^{133}Cs mixture. The newly implemented gray molasses cooling on ^{6}Li as a sub-Doppler cooling scheme improves the starting conditions for the loading of the optical dipole trap an thereby also the resulting final conditions of the atomic sample. We go through the improved preparation sequence for ^{6}Li step by step starting with the working principle, implementation and characterization of gray molasses cooling in section 2.1. Afterwards, we report on the modulated dipole trap for enhanced dipole trap loading in section 2.2. We present the characterization of forced evaporative cooling and the final degenerate ^{6}Li sample in section 2.3. We close the chapter with a summary of the preparation sequences for an ultracold ^{6}Li sample and an ultracold ^{6}Li-^{133}Cs mixture in sections 2.4 and 2.5 respectively.

2.1 Gray Molasses Cooling

The standard optical cooling schemes used for alkali atoms are limited in ^6Li due to the unresolved hyperfine splitting of the $2^2P_{3/2}$ excited states [Lett et al., 1988]. Additionally, the light mass of Lithium leads to a rather high Doppler temperature of around 140 µK leading to an overall high limit of the optical cooling temperature. In the past two techniques have been developed to reduce the limit of optical cooling of ^{6}Li. The first method is Narrow-line cooling on the $2^2S_{1/2} \rightarrow 3^2P_{3/2}$ transition at 323 nm. Due to the reduced linewidth of the transition, the Doppler temperature reduces to 18 µK. This method has been implemented successfully in ^{6}Li experiments [McKay et al., 2011; Duarte et al., 2011] and lead to optical cooling to temperatures of less than 60 µK. The other method is gray molasses cooling. Using the D_1-line and a combination of Sysiphus cooling [Castin et al., 1991] and velocity selective coherent population trapping (VSCPT) [Grynberg and Courtois, 1994; Weidemüller et al., 1994], this method lead to temperatures around 40 µK in ^{6}Li for different groups [Grier et al., 2013; Burchianti et al., 2014; Gerken, 2016]. In this section we present the working principle of gray molasses cooling, the experimental implementation and characterization. The work in this section is based on Gerken [2016].

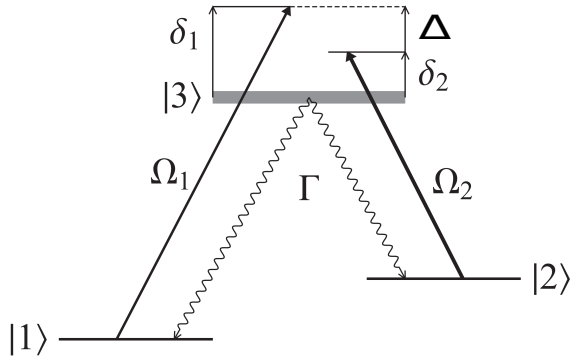

Figure 2.1: Three-level Λ scheme with two ground states $|1\rangle$, $|2\rangle$ and an excited state $|3\rangle$ coupled by two light fields Ω_1 and Ω_2 detuned from resonance by δ_1 and δ_2 respectively. For $\delta_1 = \delta_2$ this configuration leads to a dark state $|\Psi_D\rangle$ and a bright state $|\Psi_B\rangle$ configuration as described in the text. Figure adapted from Grier et al. [2013]

Dressed state picture in three-level Λ configuration presents a good model system to understand the base principles of gray molasses cooling including a combination of Sisyphus like cooling, a dark state and VSCPT. Figure 2.1 shows a three-level system in Λ configuration, consisting of two ground states $|1\rangle$, $|2\rangle$ and an excited state $|3\rangle$ coupled by two light fields with Rabi frequencies Ω_1 and Ω_2, detuned by δ_1 and δ_2 from the excited state, respectively. In the case of $\delta_1 = \delta_2$ the Hamiltonian H in the dressed state picture is given by

$$H = H_{kin} + H_0 + V = H_{kin} + \frac{\hbar}{2}\begin{pmatrix} 0 & 0 & \Omega_1 \\ 0 & 0 & \Omega_2 \\ \Omega_1 & \Omega_2 & -2\delta_1 \end{pmatrix} \tag{2.1}$$

,

where $H_{kin} = \frac{1}{2}mv^2$, H_0 and V give the kinetic energy, the bare energies of the states and the light coupling, respectively. The diagonalized Hamiltonian gives the new basis with a dark and a bright state $|\Psi_D\rangle$ and $|\Psi_B\rangle$

$$|\Psi_D\rangle = \frac{1}{\sqrt{\Omega_1^2 + \Omega_2^2}}(\Omega_2 |1\rangle - \Omega_1 |2\rangle) \tag{2.2}$$

,

$$|\Psi_B\rangle = \frac{1}{\sqrt{\Omega_1^2 + \Omega_2^2}}(\Omega_2 |1\rangle + \Omega_1 |2\rangle) \tag{2.3}$$

.

Here for $H_{kin} = 0$, $|\Psi_D\rangle$ does not experience a light shift $E_D = 0$, $|\Psi_B\rangle$ instead couples to the bright state $|3\rangle$ and experiences a light shift of $E_B = \frac{\Omega_1^2+\Omega_2^2}{\delta_1}$. Including a kinetic energy term that is non-zero $H_{kin} \neq 0$ the detunings δ_1 and δ_2 are Doppler shifted and

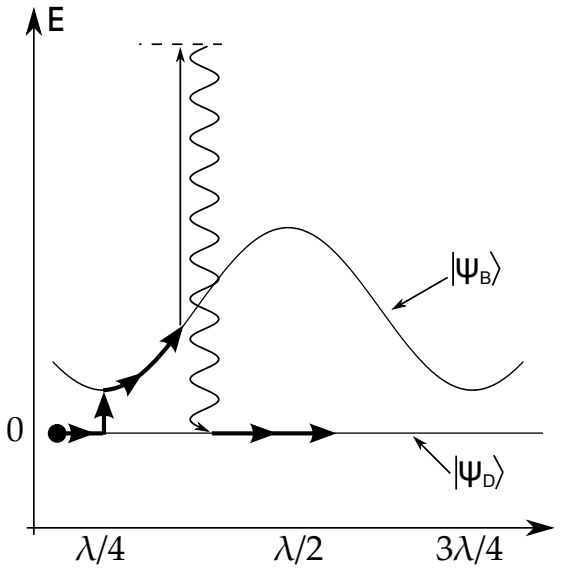

Figure 2.2: A spatially dependent polarization for a three-level λ system as shown in figure 2.1 with a positive detuning $\delta_1 = \delta_2 > 0$ leads to a spatially dependent light shift of the bright state $|\Psi_B\rangle$. Atoms in a moving frame experience velocity selective coupling from the dark state $|\Psi_D\rangle$ to the bright state $|\Psi_B\rangle$ as shown in equation 2.4. Atoms climb the potential hill and decay back to the dark state leading to loss of kinetic energy. Figure taken from Rio Fernandes et al. [2012]

.

the dark state picture breaks down. The dark state $|\Psi_D\rangle$ experiences a velocity dependent coupling to the bright state $|\Psi_B\rangle$ given by

$$P_{|\Psi_D\rangle \to |\Psi_B\rangle} = 2 \left(\frac{\Omega_1 \Omega_2}{\sqrt{\Omega_1^2 + \Omega_2^2}} vm \frac{k}{\hbar} \right)^2 \delta_1 \frac{\delta_1}{(\Omega_1^2 + \Omega_2^2)} \tag{2.4}$$

where k is the wavenumber of the transition, v is the velocity of the atom [Papoff et al., 1992]. The coupling probability increases with v^2 [Dalibard and Cohen-Tannoudji, 1989] and the inverse of the bright state light shift E_B. The light field alone does not lead to cooling. A spatially dependent light field however, leads to the expected results.

A Polarization gradient field leads to a more complex system. The light coupling between different hyperfine states $\left|f, m_f\right\rangle$ and $\left|f', m'_f\right\rangle$ is polarization dependent leading to a polarization dependent light shift. A light field with spatially dependent polarization leads to a dark and bright state configuration as shown in figure 2.2. Polarization gradient light fields can be generated in different ways. One way is used in a Magneto-Optical-trap (MOT) where two counter propagating beams are in σ^+-σ^- configuration for all three spatial dimensions. Another method are two counter propagating beams in horizontal and vertical polarization. The spatially dependent phase shift will then lead to a change

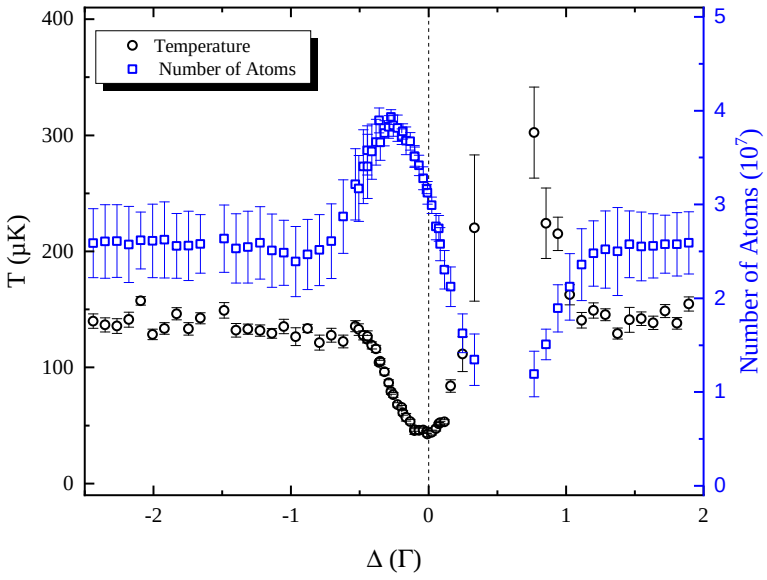

Figure 2.3: Temperature T (black circles) and number of atoms N (blue squares) after 1 ms of gray molasses cooling as a function of the relative detuning Δ in units of Γ with $\delta_{cool} = 4\Gamma$, $I_{cool} = 15 I_{sat}$ and $I_{rep} = 0.75 I_{sat}$. At the Raman condition $\Delta = 0$, a capture efficiency of 80% and a temperature of $T = 42\,\mu\text{K}$ are reached. For $\Delta = -0.25\Gamma$ 100% of the atoms are trapped at a temperature of $T = 80\,\mu\text{K}$. Taken from Gerken [2016]

of the polarization along the beam axis with a period of half the wavelength [Dalibard and Cohen-Tannoudji, 1989].

The process of a moving atom in the dark state, coupling to the bright state at low bright state light shift E_B via VSC, climbing up the potential hill, decaying to the dark state can be repeated several times. The process will stop when the velocity of the particle is reduced such that the coupling probability goes to zero. Within the three level model the theoretical limit is at $\vec{v} = 0$, small compared to the Doppler limit or even the recoil limit [Esslinger et al., 1996]. Off-resonant coupling and imperfect polarization however lead to coupling of the dark state to the bright state and limit the temperature. Nevertheless the nature of gray-molasses cooling leads to a population of the coherent dark state as a final stage of the cooling process leading to the name of VSCPT [Arimondo, 1991].

The Experimental implementation and characterization on ^{6}Li in our experiment is presented in Gerken [2016]. Three counter propagating beams in σ^+-σ^- configuration consisting of two frequencies $f_{|f=1/2\rangle \to |f'=3/2\rangle}$ and $f_{|f=3/2\rangle \to |f'=3/2\rangle}$ on the D_1 line at intensities I_{cool} and I_{rep} respectively, both detuned by Δ from resonance where implemented. The light is switched on for a short pulse of $t = 1\,\text{ms}$at zero magnetic field after the MOT phase. An improved version of the optical setup is presented in A.1. It

is important to note, that a magnetic field would disturb the cooling scheme very easily. Considering a Zeeman shift, on the order of the line width $\hbar\Gamma$ of the optical transitions, would lead to the breakdown of the coherent dark state. This is already the case for magnetic fields on the order of $B = 1\,\mathrm{G}$ [Gerken, 2016]. Because of this, extra care has been taken for a fast switching of the magnetic quadrupole field of the MOT but also the zero field calibration (see chapter 3).

Figure 2.3 shows the final temperature T and atom number N after $t = 1\,\mathrm{ms}$ of gray molasses cooling from an initial MOT consisting of $N_0 = 4 \times 10^7$ atoms at a temperature of $T_0 = 240\,\mu\mathrm{K}$. The intensities were set to $I_{cool} = 15 I_{sat}$ and $I_{rep} = 0.75 I_{sat}$ where I_{sat} is given by $I_{sat} = \Gamma\hbar f_0^3/3c^2$ where f_0 is the transition frequency of the D_1 line. The x-axis shows the relative detuning $\Delta = \delta_1 - \delta_2$. At a relative detuning of $\Delta = 0$ we achieved temperatures of $42\,\mu\mathrm{K}$ at a capture efficiency of 80%. Considering no significant expansion during the cooling cycle, this corresponds to a gain in phase space density by a factor of approximately 10.

2.2 Dipole Trap Loading

Loading an atomic cloud into an optical dipole trap is a crucial point for the preparation of ultracold gases [Grimm et al., 2000]. Particular care has to be taken to achieve good mode-matching between trap and free atom cloud, meaning good overlap in real space and momentum space. After having discussed the implementation of gray molasses cooling of ^{6}Li we now describe changes implemented on the dipole trap loading. We start by discussing what good mode-matching exactly means. Then we describe the setup of the optical dipole trap and the setup of the trap modulation.

Mode-Matching describes the adjustment of two different phase-space distributions. Efficient loading of an optical dipole trap can be understood as a projection of the phase-space distribution $\bar{\omega}(\vec{r}, \vec{p})$ onto the volume of the dipole trap. The number of loaded atoms is estimated by

$$N_{load} = \int \bar{\omega}(\vec{r}, \vec{p}) \mathrm{d}\vec{r} \mathrm{d}\vec{p} \tag{2.5}$$

where $\bar{\omega}(\vec{r}, \vec{p})$ is the phase space distribution of the atomic cloud as a function of the position $\vec{r}$ and momentum $\vec{p}$. For a thermalized gas at temperature T one can divide the phase-space-density into a spatial density $n(\vec{r})$ and a Maxwell-Boltzmann distribution at a temperature T. The integral limits are given by the trap volume V and the trap depth U_0 (see chapter 1.4). The number of loaded atoms N_{load} into the trap is then given by [Luiten et al., 1996]

$$N_{load} = n_0 V \left[\mathrm{Erf}\left(\sqrt{\frac{U_0}{k_B T}} \right) - \frac{2}{\sqrt{\pi}} \sqrt{\frac{U_0}{k_B T}} \exp\left(\frac{-U_0}{k_B T} \right) \right] \tag{2.6}$$

Here n_0 is the peak density, k_B is the Boltzmann and $\mathrm{Erf}(x) = 2/\sqrt{\pi}\int_0^x \exp\left(-x^2\right)\mathrm{d}x$ is the error function. The integral over the density can be replaced by $n_0 V$ if the trap volume is small compared to the initial cloud size. In this model one can see, that maximizing the volume V and the trap depth U_0 leads to a maximum number of loaded atoms. However, there are limitations to the model. If the volume V is chosen larger than the initial cloud, non-adiabatic expansion of the cloud will lead to a reduction in phase-space-density [Ketterle et al., 1999]. If U_0 becomes large compared to the average kinetic energy of the atoms, converting potential energy into kinetic energy will lead to heating of the gas. Limited laser power leads to a forced compromise between V and U. V can be estimated by the beam waists of the trap giving $V = 2w_{x_1}2w_{x_2}2w_{x_3}$. Equation 1.3 shows how V and U_0 are related. This leads to an optimized loading for a maximal volume at a trap depth of approximately $U_0 \approx 10T_0$. The change in the initial temperature T_0 of the atomic cloud due to gray molasses cooling requires a new evaluation of the optimal trap volume. In the following section we discuss the dipole trap setup and spatial modulation scheme we use to achieve the needed trap volume at the given trap depth.

The time Averaged Potentials is an effective trapping seen by the atoms caused by fast changing potential compared to the reaction time of the atoms. A fast changing potential $U(\vec{x_1})$ will lead to a potential $U_{Avg}(\vec{x_1})$ under the following circumstances.

Atoms being exposed to an optical potential $U(\vec{x_1})$ react to the potential on a timescale given by the trapping frequencies $t = 2\pi/\omega_{x_1}$. If the potential undergoes slow changes in time $U(\vec{x_1(t)})$ with $t \ll 2\pi/\omega_{x_1}$, then the atoms are exposed to the initial potential characterized by ω_{x_1} but with a moving center position $U_0(\vec{x_1}(t))$. If however the changes of the potential are fast compared to the trap frequencies meaning $t \gg 2\pi/\omega_{x_1}$, then the atoms feel a new potential. As discussed in Roy et al. [2016], the resulting potential $U_{Avg}(x_1)$ can be approximated by an harmonic potential if the modulation function $\mathrm{ModFct}(t)$ solves the equation

$$\frac{1}{3A_{Mod}^3}\mathrm{ModFct}(t)^3 - \mathrm{ModFct}(t) + v_0 t = 0 \tag{2.7}$$

where A_{Mod} is the modulation amplitude and v_0 is an integration constant defined by the modulation frequency f_{Mod} and A_{Mod}. The resulting potential will thus lead to trapping frequencies $\omega_{A_{Mod}}$.

The Modulation setup is an extension of the dipole trap setup introduced in chapter 1.4. To understand the implementation of the spatial modulation of this trap, we present a more detailed description of the dipole trap setup which has been described previously in Pires [2014]; Ulmanis [2017]; Häfner [2017]. We use a 200 W Yb-doped fiber laser (IPG YLR-200-LP-WC) at a wavelength of 1064 nm with two back reflected crossed beams at a crossing angle of $\beta = 8.4°$ with a beam waist of 60 µm. With a maximum power of 120 W at the position of the atoms, this leads to a trap depth of approximately $U_0/k_B \approx 2$ mK. The intensity can be tuned via two acousto-optical-modulators (AOM) (CRYSTAL TECHNOLOGY, 3110-197), one in horizontal and one in vertical direction. By varying

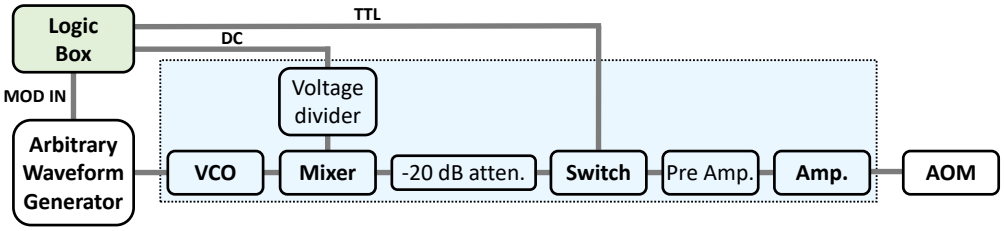

Figure 2.4: Schematic of AOM control dipole trap modulation setup. The logic box is controlled via the experimental control system. The arbitrary waveform generator produces the modulation signal send to the VCO. The power of the dipole trap is controlled via a mixer can be turned on and off via a switch. Figure taken from Neiczer [2018].

the frequency applied to the horizontal AOM, the refractive angle and thus the beam path changes. Figure 2.5 shows a schematic picture of the beam path at three different AOM frequencies. The center or crossing point of the two beams indicate the position of the dipole trap. By tuning the AOM frequency the center of the dipole trap is changed along the first beam. The setup of the AOM driver is presented in figure 2.4. The AOMs are driven by radio-frequency signals $f_{AOM}(V_{VCO})$ on the range of 100 MHz to 120 MHz supplied by Mini-Circuits ZX95-200+VCOs. Here the input voltage V_{VCO} determines the frequency f_{AOM}. The signal is amplified with powers between 0 W and 3 W. An arbitrary waveform generator (RIGOL DG4000) generates the input voltage V_{VCO}. By applying a periodic signal with frequency f_{Mod} to the VCO, one gets an AOM frequency f_{AOM} that changes with the modulation frequency f_{Mod}. This leads to a periodic change of the trap position. For a modulation frequency fast compared to the trapping frequencies, this leads to a time averaged potential. With this setup we increase the axial size of the trap up to a factor of four by applying a triangle shaped modulation waveform.

The experimental characterization of the dipole trap loading with a modulated trap is presented in figure 2.6. The figures show the normalized temperature of the loaded cloud T/T_0, the normalized number of loaded atoms N/N_0 and the normalized phase space density ρ/ρ_0 in the trap in dependence of the normalized axial size σ/σ_0. The power of the trap is kept at a maximum of 120 W. The initial values (corresponding to no modulation) are given by $N_0 = 1 \times 10^6$, $T_0 = 120\,\mu\text{K}$, $\rho_0 = 3 \times 10^{-5}$ and $\sigma_0 = 260\,\mu\text{m}$. A decrease of the temperature is explained by the decrease in trap depth with an increasing trap size (see equation 1.3) and reaches a minimum of $0.5T_0$. The increase in atom number is caused by the increase in volume (see equation 2.6) and reaches a maximum of $2.3N_0$. The PSD increases up to a factor of 2.3 while loading. Even though the atom number increases and the temperature decreases for large axial sizes, the PSD decreases due to the decrease in trap frequency (and thereby atom density).

With the improved dipole trap loading, we end the trap loading with 2×10^6 atoms in each spin state at a temperature of $T = 70\,\mu\text{K}$ with a PSD of $\rho = 7 \times 10^{-5}$.

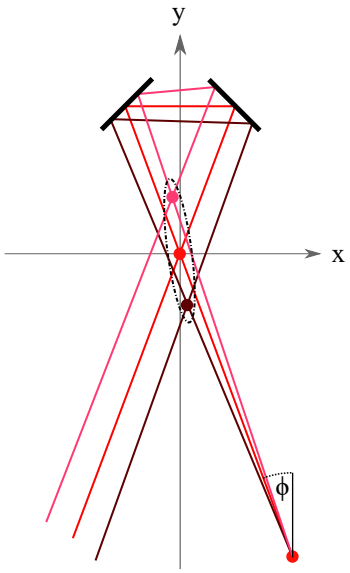

Figure 2.5: Beam path of the modulated crossed optical dipole trap. The beams leave from the AOM depicted by the red dot at the lower right and are reflected at the mirrors depicted by the solid black lines. The crossing point of the optical dipole trap is translated by adjusting the diffraction angle ϕ after the ATOM via frequency f_{AOM} tuning. The crossing position of the respective beams is depicted by the colored dots at the crossing points. The black dot dashed line depicts the size of the arising modulated trap.

2.3 Creation of a Bose-Einstein-Condensate of ^{6}Li

For the creation of a quantum degenerate sample of ^{6}Li we need to increase the phase-space density by more then four orders of magnitude. Forced evaporation on ^{6}Li is a favorable cooling process to achieve this. Due to the suppression of inelastic loss processes even at diverging scattering length, a fast and efficient forced evaporation leads to huge increase in PSD with comparably small loss in atom number. The evaporation efficiency is defined by [Ketterle and Druten, 1996]

$$\gamma_{evap} = \frac{\log\left(\frac{\rho}{\rho_0}\right)}{\log\left(\frac{N_0}{N}\right)} \tag{2.8}$$

describing the logarithmic increase in PSD over the decrease of atoms. Figure 2.7 shows the PSD of ^{6}Li over the number of atoms during the evaporation sequence. The red numbers indicate the evaporation efficiency γ_{evap} during the different experimental dipole trap power ramps. The evaporation is started of with an increase of a factor of 600 in the PSD while loosing a factor of 3 in atoms with $\gamma_{evap} = 5.8$. The evaporation ramp is followed by a 100 ms adiabatic ramp down of the modulation amplitude. Adiabaticity has been assured via a two way ramp confirming preservation of the initial condition. The decrease in phase space density can be explained by a change in the potential shape

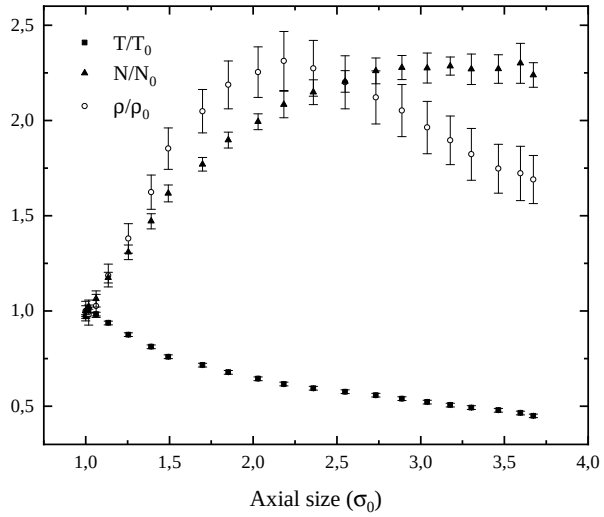

Figure 2.6: Dipole trap loading of ^{6}Li with a modulated trap. The x-axis shows the axial size of the trap in dependence of the initial trap size σ_0. The axial size depends on the modulation amplitude while the radial sizes of the trap stay almost constant. Shown are the temperature T normalized over the initial temperature of the trap without modulation T_0 in solid squares, the Atom number N normalized over the initial atom number N_0 in solid triangles and the phase-space-density (PSD) ρ over the initial PSD ρ_0 in open circles. The error bars are given by standard deviation of the measurements. For a modulation that leads to twice the axial size of the dipole trap, the temperature decreases by a factor of 1.6 while the atom number increases by a factor of 2 and the PSD increases by a factor 2.3.

described by β_{trap} [Walraven, 2010]

$$U(\vec{r}) = \omega_0 |\vec{r}|^{3/\beta_{trap}} \tag{2.9}$$

The triangle shape of the modulated trap leads to $\gamma_{trap0} = 3$ whereas the unmodulated trap in a standard harmonic shape follows $\beta_{trap} = 3/2$. [1] The decrease in PSD can thus be explained by a change in the potential form.

A ^{6}Li Bose-Einstein-Condensate (BEC) is reached after a further evaporation ramp following the modulation turn off. With a positive scattering length of the double component ^{6}Li gas we reach a BEC of ^{6}Li dimers [Jochim et al., 2003]. Figure 2.8 shows an integrated density profile of the BEC fitted with a Gaussian function (green) and a parabolic density distribution (teal) [Ketterle and Zwierlein, 2008] after a time of flight of 10 ms at a scattering length of $a_{LiLi} \approx 2000\, a_0$. The lower picture shows the corresponding

[1] For an adiabatic change of the trap shape, the change in PSD is given by [Walraven, 2010]

$$\frac{\rho}{\rho_0} = \frac{\exp\left(5/2 + \beta_{trap} + S/(Nk_B)\right)}{\exp\left(5/2 + \gamma_{trap0} + S/(Nk_B)\right)} \tag{2.10}$$

where the entropy S and the atom number N stay constant and k_B is the Boltzmann constant.

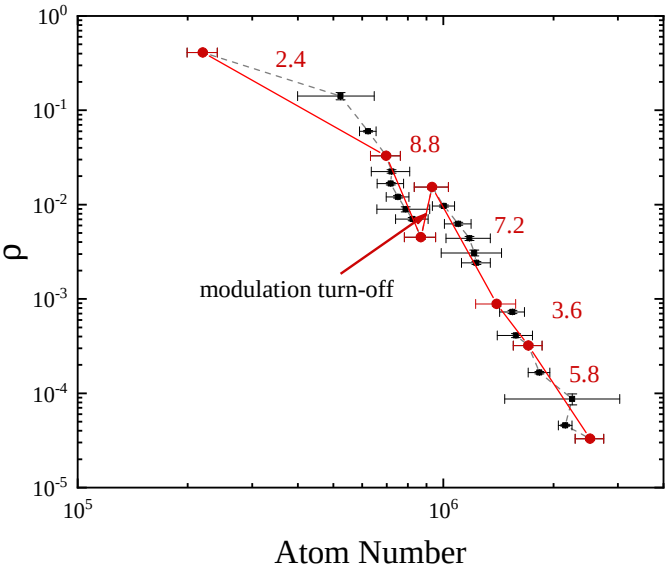

Figure 2.7: Phase-space-density ρ over atom number for evaporative cooling of ^{6}Li in a cigar shaped spatially modulated dipole trap. With an initial condition of 2.5×10^6 atoms at a PSD of 3×10^{-5} the cloud is evaporated to a final condition of 5×10^5 atoms at a PSD of 0.1. The values in red are evaporation efficiencies given by equation 2.8. Overall the PSD is increased by five orders of magnitude while loosing one order of magnitude in atoms. The modulation turn-off is performed as an adiabatic ramp of the modulation amplitude.

absorption picture. With the described sequence we achieve ^{6}Li-BECs of 3×10^5 atoms with a condensate fraction of 50%.

2.4 Preparation of ultracold ^{6}Li

Here we present the resulting experimental sequence for the preparation of an ultracold ^{6}Li sample from the information presented in the previous sections. The presented sequence has been used for the data presented in part II of this thesis. We prepare thermal ^{6}Li samples of 3×10^4 atoms at temperatures between 300 µK and 100 µK.

Figure 2.9 shows a schematic time line of the experimental preparation. We start by loading a ^{6}Li MOT for 2 s, transferring the cloud from the quadrupole field of the MOT coils to the quadrupole field of the curvature coils. After fast switching of the magnetic field we apply a 5 ms gray molasses light pulse with an intensity ramp in the last millisecond. During this stage the dipole trap is already turned on at 120 W with the optimized modulation amplitude. After the optical cooling we jump to a magnetic field of 890 G with a $|1/2, 1/2\rangle$-$|1/2, -1/2\rangle$ scattering length of $a_{LiLi} = -8800\, a_0$. After 2 s forced evaporative cooling by ramping the trap power to 3 W, we adiabatically ramp the spatial trap modulation down within 100 ms followed by another 3 s forced evaporation ramp to the final trap power. At this point we jump to a magnetic field of 920 G where we apply

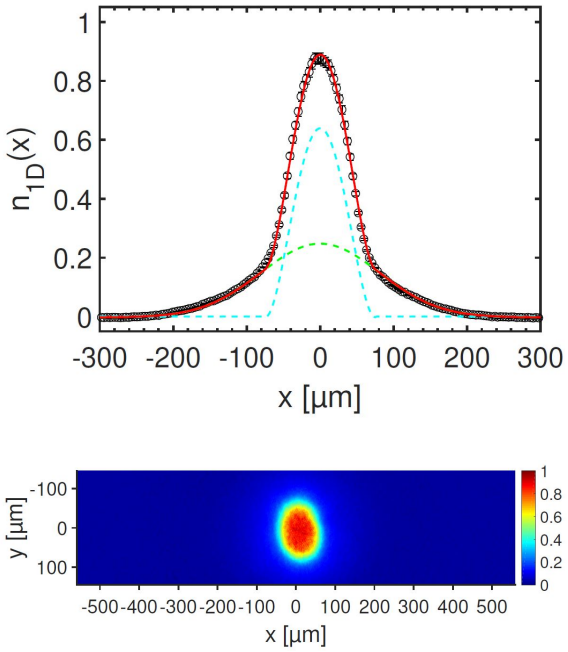

Figure 2.8: ^{6}Li Bose-Einstein-Condensate after 10 ms time of flight at a scattering length of $a_{LiLi} \approx 2000\, a_0$. Upper figure shows one dimensional column density with a Bimodal fit (red) consisting of a Gaussian function (green) and a parabolic function (teal). The total dimer number is 3×10^5 at a condensate fraction of $f = 0.5$. The lower figure shows the absorption image taken from the top. The condensed part and the thermal part of the cloud can be distinguished by eye. Figure taken from Neiczer [2018].

a short light pulse to clean the sample from either the $|1/2, 1/2\rangle$ state, the $|1/2, -1/2\rangle$ state, or we don't apply a light pulse if we want to keep both spin states. We end up with Lithium either in the $|1/2, -1/2\rangle$ the $|1/2, 1/2\rangle$ or both states in the dimple trap at temperatures between $140 - 300$nK, atom numbers of $N = 3 \times 10^4$ in one spin state at densities of $n_0 = 1.6(1) \times 10^{11}\text{cm}^{-3}$, $T/T_F = 0.53(4)$. A jump 1 G above the magnetic field of interest is followed by a short hold time of 50 ms for the magnetic field to stabilize. Then we go to the magnetic field where we perform atom loss spectroscopy and hold it there for a time t_{hold}. Finally we jump to a magnetic field of 920 G and perform absorption imaging to extract atom number and sample temperature. An experimental cycle has a duration of approximately $\sim$8 s.

2.5 Preparation of an ultracold ^{6}Li-^{133}Cs mixture

In this section we present the experimental sequence used for the preparation of an ultracold ^{6}Li-^{133}Cs mixture used in the experiments presented in part II of this thesis. With this sequence we achieve final mixture temperatures between 800 µK and 200 µK.

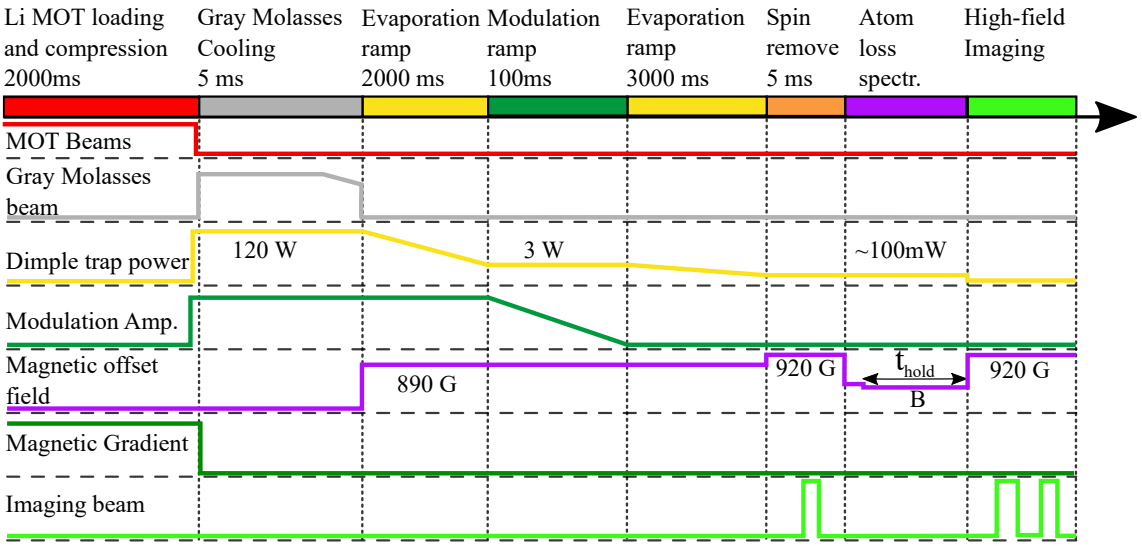

Figure 2.9: Schematic presentation of the preparation sequence for an ultracold sample of ^{6}Li atoms at a temperature down to 100 nK. Dimple trap powers and modulation amplitude over time within the sequence as well as the magnetic offset and gradient field.

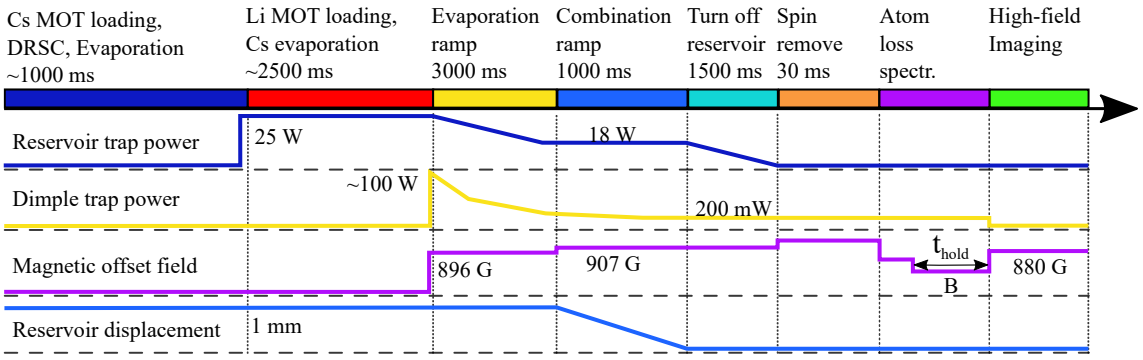

Figure 2.10: Schematic presentation of the preparation sequence for an ultracold sample of ^{6}Li-^{133}Cs atoms at a temperature down to 200 nK. Reservoir trap and Dimple trap powers over time within the sequence as well as the magnetic offset field and the reservoir trap displacement from the dimple trap. Figure adapted from Häfner [2017].

Figure 2.10 shows a schematic time line of the experimental preparation. We start by loading a ^{133}Cs MOT via the double species Zeeman slower 1 mm away from the center of the experimental chamber. Afterwards we compress the MOT by increasing the magnetic gradient and by further detuning the cooling light from resonance. Due to the natural sub-Doppler cooling of ^{133}Cs on the D2-line [Drewsen et al., 1994], we achieve temperatures of approximately 8 µK at an atom number of 4×10^7 after 1 s loading time. Continuing with dRSC [Vuletic et al., 1998; Kerman et al., 2000; Treutlein et al., 2001], the ^{133}Cs atoms are pumped to the lowest energy state $\left|f_{Cs} = 3, m_f = 3\right\rangle$ and further cooled down to temperatures below 1 µK . At this point we turn on the reservoir trap at approximately

30 W. Due to the gravitational potential acting on ^{133}Cs, the atoms are heated during the loading process. After quarter trap period increments we apply dRSC light pulses. In total we apply three pulses. We end up with 2×10^6 atoms at a temperature of 2 µK at a density of approximately $1 \times 10^{13}\mathrm{cm}^{-3}$ inside the reservoir trap. A small magnetic offset field of 4.5 G is applied to maintain the spin polarization of 85%. The ^{133}Cs atoms are stored in the reservoir trap while the ^{6}Li MOT is loaded for 2.5 s. After the compression of the MOT, the atoms are optically pumped into the lowest hyperfine states $f_{Li} = 1/2$ and loaded into the dimple trap, situated at the center of the experimental chamber. The loading of the trap is performed at a magnetic field of 896 G where ^{6}Li thermalization is fast. Within three seconds we perform forced evaporative cooling on ^{6}Li and ^{133}Cs separately at scattering length of $a_{LiLi} \approx -8000\, a_0$ and $a_{CsCs} \approx 320\, a_0$. At a magnetic field of 907 G and interspecies scattering length of $a_{LiCs} \approx 100\, a_0$ we move the reservoir trap within 1 s by 1 mm with the Piezo mirror to overlap ^{6}Li and ^{133}Cs. Thermalization between ^{6}Li and ^{133}Cs leads to sympathetic cooling of ^{133}Cs. Overlapping both species is concluded by slowly turning off the reservoir trap within 1.5 s. After applying a resonant light pulse to one of the ^{6}Li spin states we end up with an ultracold spin polarized mixture of $Li|1/2, 1/2> + Cs|3, 3>$ or $Li|1/2, -1/2> + Cs|3, 3>$ with 5×10^4 ^{133}Cs and 3×10^4 ^{6}Li at temperatures between $200 - 850$nK in the dimple trap. A jump 1 G above the magnetic field of interest is followed by a short hold time of 50 ms for the magnetic field to stabilize. Then we go to the magnetic field where we perform atom loss spectroscopy and hold it there for a time t_{hold}. Finally we jump to a magnetic field of 880 G and perform absorption imaging on both species to extract atom number and sample temperature. An experimental cycle has a duration of approximately ≈10 s.

3. Calibrating the magnetic field landscape

Magnetic fields are an essential part of the ultracold ^{6}Li-^{133}Cs experiment. We have already seen in section 2.1, that magnetic fields can be destructive or necessary for certain cooling schemes. As we will see in section 4.2, magnetic fields are a powerful tool to control inter particle scattering and molecule-state energy via Feshbach resonances[Chin et al., 2010]. Thus, magnetic field control is at the heart of the investigations on p-wave Feshbach resonances presented in part II of this thesis.

The magnetic field landscape of our experiment has already been discussed in previous work [Repp, 2013; Pires, 2014; Ulmanis, 2017; Häfner, 2017]. Thus we focus on new insights and developments. In this chapter we introduce the behavior of ^{6}Li and ^{133}Cs in a magnetic field and methods for magnetic field calibration via rf spin flip of ^{6}Li and ^{133}Cs (sections 3.1 and 3.2). We present compensation of external magnetic fields in section 3.3 and a precise characterization of the Feshbach field landscape in section 3.4. Finally we conclude on the magnetic field uncertainty on measurements presented in part II (section 3.5).

An exact knowledge of the magnetic field landscape is key for precision measurements on magnetic fields dependence. Atoms themselves can be used to determine the magnetic field with very high precision. By measuring atomic transitions and knowing their magnetic field dependence one can extract the value of the magnetic field. Optical transitions are a possible and simple method. Due to large optical line width on the order of MHz however, the calibration of fields between 0 G and 1200 G are usually limited to a precision of $\Delta B = 3$ G. A more sophisticated and precise method is the measurement of a rf transition, meaning the transition from one hyperfine state of the ground state manifold into another. Figure 3.1a and 3.1b, show the ground state manifold for ^{6}Li and ^{133}Cs respectively, at magnetic fields between 0 G and 1000 G, calculated using the well known Breit-Rabi formula [Breit and Rabi, 1931]. In the case of ^{6}Li the energy behavior can be separated into two parts: at fields between 0 G and a few tens of Gauss, the total angular momentum f with the projection m_f onto the magnetic field axis, is a good quantum number. This regime is called the Zeeman regime. At fields larger then a few hundred Gauss we are in the Pschen-Back regime where j and m_j, the total electronic angular momentum and its projection onto the magnetic field axis, are good quantum numbers. Nevertheless it is common to remain with the f and m_f quantum numbers in this regime

due to a bijectiv assignment. The inset shows the behavior of the energy difference between the state $^6\mathrm{Li}\left|f = 1/2, m_f = 1/2\right\rangle$ (black), and $^6\mathrm{Li}\left|f = 1/2, m_f = -1/2\right\rangle$ (red), with linear behavior within both regimes. In the case of ^{133}Cs and fields between 0 G and 1200 G the energy behavior only acts within the Zeeman regime due to the large hyperfine interaction. The inset shows the energy difference between the $^{133}\mathrm{Cs}|4, +4\rangle$ (red) and the $^{133}\mathrm{Cs}|3, +3\rangle$ (blue) state. In the following we call $^6\mathrm{Li}|1/2, 1/2\rangle{=}|1\rangle$ and $^6\mathrm{Li}|1/2, -1/2\rangle{=}|2\rangle$.

3.1 Lithium rf spectroscopy

The Breit-Rabi formula introduced in the previous section can be used to determine the magnetic field in a very precise manner. Using a Lithium rf spin flip, transferring atoms from state $|2\rangle$ to state $|1\rangle$ or vise versa by applying an electromagnetic fields on the scale of $h \times 75\,\mathrm{MHz}$, the magnetic field can be determined with relative precision down to $\Delta B/B = 10^{-6}$. Two examples for these magnetic field measurements are presented in figure 3.2a and 3.2b. We start by preparing a sample of ^{6}Li atoms as described in section 2 with N_0 around 3×10^4 to 8×10^4 atoms in the $|1\rangle$ spin state at a magnetic field B_0. We then apply a rf pulse at a certain frequency f with a power that transfers into a Rabi frequency Ω_0 for a time τ. By scanning the frequency we transfer a certain number of atoms $N_0 - N$ to the state $|2\rangle$. The remaining number of atoms in state $|1\rangle$ is given by the line shape

$$N(f) = N_0 \left[1 - \Omega_0^2 \left(\frac{\sin\big(\Omega_{\mathrm{eff}}(f)/2 \times \tau\big)}{\Omega_{\mathrm{eff}}(f)}\right)^2\right], \tag{3.1}$$

where $\Omega_{\mathrm{eff}} = \sqrt{\Omega_0^2 + (2\pi\delta)^2}$ is the effective Rabi frequency with $\delta = f - f_0$, the detuning from the atomic resonance frequency f_0. By fitting the number of atoms detected in state $|1\rangle$ with equation 3.1 we extract a resonance frequency f_0 from the measurements. Using the Breit-Rabi formula we translate this into a magnetic field. Figure 3.2a shows a typical uncertainty for f_0 on the order of 40 Hz. Figure 3.2b shows a typical uncertainty for f_0 on the order of 1 Hz. Due to the difference of the energy on the magnetic field $\partial E/\partial B|_{B_0}$ both uncertainties translate to magnetic field uncertainties of 1 mG.

When calibrating the magnetic field for a measurement, we take three to six rf-spectra in dependence of a magnetic field control parameter within the range of the performed experiment. A magnetic field is thus attributed to a control parameter value. The magnetic field is then given by a linear interpolation of the control parameters. Interpolation uncertainties typically yield magnetic field uncertainties of 10 mG.

3.2 Cesium mw spectroscopy

Similar to a magnetic field calibration with Lithium, Cesium can be used to extract the magnetic field from a microwave spin flip spectrum taken at frequencies between 9.1 GHz

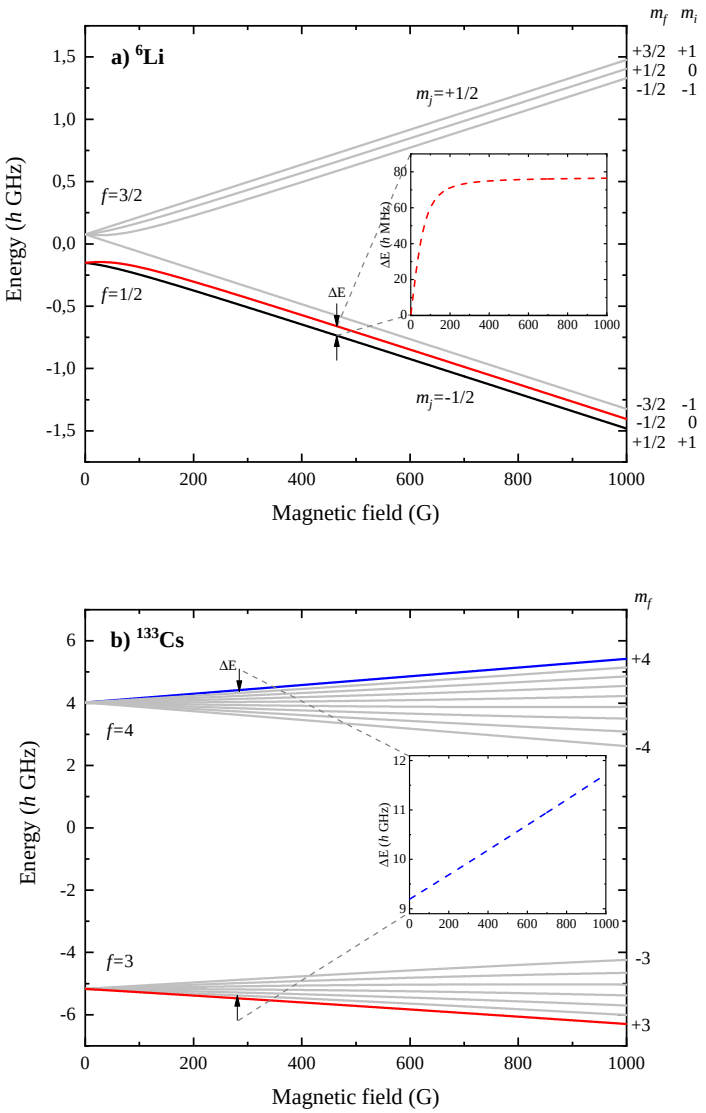

Figure 3.1: Energy of hyperfine states of a) ^{6}Li and b) ^{133}Cs in their electronic ground state in dependence of the magnetic field. f represents the total angular momentum, j the total electronic angular momentum and i presents the total nuclear spin. m_f, m_j and m_i represent their respective projection onto the magnetic field axis. In a) the highlighted curves present the $^6\mathrm{Li}|1/2, 1/2\rangle{=}|1\rangle$ (black) and $^6\mathrm{Li}|1/2, -1/2\rangle{=}|2\rangle$ (red) states. The inset shows their energy difference in dependence of the magnetic field. The Zeeman regime only holds only for small fields up to tens of Gauss. The Paschen-Back regime holds only for fields larger then few hundred Gauss where the energy splitting is between $h \times 74\,\mathrm{MHz}$ and $h \times 77\,\mathrm{MHz}$. In b) the highlighted curves present the $^{133}\mathrm{Cs}|3, +3\rangle$ (red) and $^{133}\mathrm{Cs}|4, +4\rangle$ (blue) states. The inset shows their energy difference in dependence of the magnetic field. Due to the large hyperfine splitting of ^{133}Cs we remain in the Zeeman regime over the whole field range between 0 G and 1000 G where the splitting is given by $h \times 9.193\,\mathrm{GHz}$ and $h \times 11.721\,\mathrm{GHz}$.

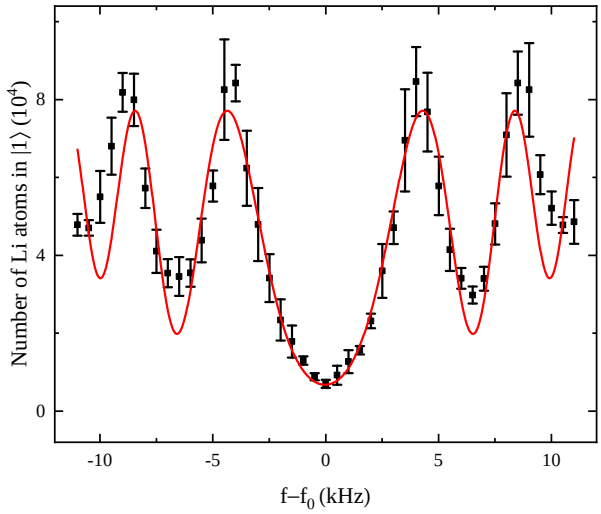

(a)

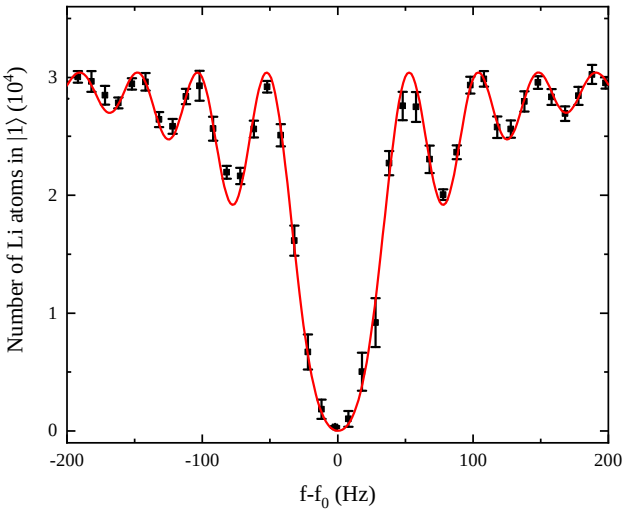

(b)

Figure 3.2: Radio-frequency spectroscopy of the ^{6}Li $|2\rangle$ to $|1\rangle$ transition. The plots show the remaining number of Li atoms in state $|1\rangle$ versus the frequency detuning $f - f_0$ from atomic resonance f_0. The red line is a fit of equation 3.1 to the measurements performed with an rf-pulse length of $\tau = 0.5$ms (a) and $\tau = 25$ms (b). We extract resonance frequencies of $f_0 = 70.269\,49(4)$ MHz (a) and $f_0 = 76.165\,892(1)$ MHz (b), corresponding to magnetic fields of $B_0 = 184.801(1)$ G (a) and $B_0 = 764.169(1)$ G (b), and on-resonance Rabi frequencies of $\Omega_0 = 2\pi \times 11.19(1)$kHz (a) and $\Omega_0 = 2\pi \times 60.3(2)$Hz (b). The data are averaged over at least 6 measurements and the error bars represent the standard error of the mean.

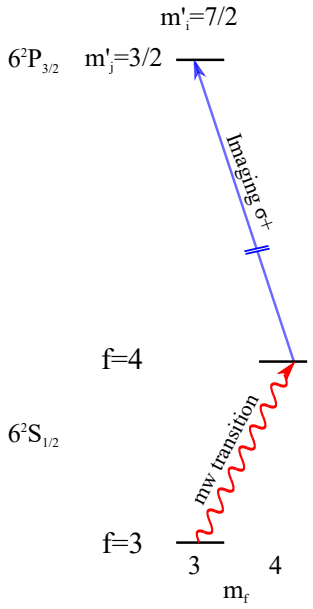

Figure 3.3: Schematic representation of Cesium detection during the magnetic field calibration at high fields. Atoms in the ^{133}Cs $6^2S_{1/2}|3,+3\rangle$ state are transfered to the $|4,+4\rangle$ state via microwave pulse (red). The absorption imaging is then performed on the imaging transition (blue) from $6^2S_{1/2}|4,+4\rangle$ to $6^2P_{3/2}\left|J'=3/2, m_{J'}=3/2\right\rangle$.

and 12 GHz. We start by preparing a sample of ^{133}Cs atoms as described in section 2.5 in the $|3,+3\rangle$ state. By applying a mw pulse at frequency f with a power corresponding to a Rabi frequency Ω_0 and a pulse length of τ, the atoms in state $\left|f=3,m_f\right\rangle$ can be transfered to states $\left|f'=4,m_{f'}=m_f\pm 0,1\right\rangle$. Assigning atomic transitions to measured resonances allows for the determination of the magnetic field.

Detection of atoms in state $|4,+4\rangle$ is performed via absorption spectroscopy. Figure 3.3 shows the optical transitions used for absorption imaging of ^{133}Cs at non zero magnetic fields. A mw signal (red) is used to transfer the atoms from the $6^2S_{1/2}|3,+3\rangle$ to the $6^2S_{1/2}|4,+4\rangle$. The optical transition (blue) is used for absorption imaging. Figure 3.4 shows the normalized number of Cesium atoms in the $|4,+4\rangle$ state after a mw transition from $|3,+3\rangle$ with frequency f with $f_0 = 9.192\,631\,77$ GHz, the exact transition frequency at zero field. The earth magnetic field is here already compensated as described in the following section 3.3. The line shows a Lorentzian function with a detuning from the zero field frequency of $f - f_0 = 750(60)$ Hz and a width of 2 kHz. The frequency detuning translates into a magnetic field uncertainty of $B = 0.30(3)$mG. Figure 3.4 shows Rabi oscillations on resonance. The Rabi frequency is deduced by fitting a sinus curve $N(t) = N_0 \sin(\Omega_0 t/2)^2$ where we extract $\Omega_0 = 2\pi \times 1.8(1)$Hz.

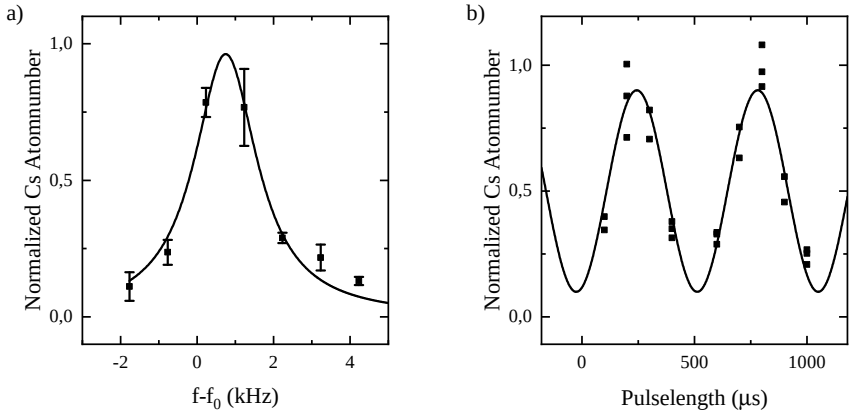

Figure 3.4: Cesium mw spin flip from $|3,+3\rangle$ to $|4,+4\rangle$ with a pulse length of $\tau = 250\,\mu s$. a) Normalized number of atoms depending on $f - f_0$ where $f_0 = 9.192\,631\,77\,\text{GHz}$ is the resonance frequency at zero field. The Lorenz curve shows a width of $w = 2.0(3)\,\text{kHz}$ and a center position detuned by $f - f_0 = 750(60)\,\text{Hz}$. This translates into a magnetic field uncertainty of $B = 0.30(3)\text{mG}$. b) Shows the corresponding Rabi oscillations on resonance with a Rabi frequency of $\Omega_0 = 2\pi \times 1.8(1)\text{kHz}$.

3.3 Zero Field Calibration

Even without applied magnetic fields, the earth magnetic field and other sources, lead to a non zero field at the position of the atomic cloud. For gray molasses cooling of Lithium we have seen, that a magnetic field above 1 G can already disturb the coherent dark state and lead to heating instead of cooling. DRSC is relying on a matching between the Zeeman shift energy and the harmonic oscillator energy levels. This magnetic field is usually on the order of 100 mG in x_3 direction [Vuletic et al., 1998; Han et al., 2000; Weber, 2003]. The earth magnetic field itself is on the order of 0.5 G in Heidelberg [Harcken, 2021]. Other sources of magnetic fields e. g. Ion pumps for the ultra high vacuum lead to additional factors that need to be compensated. Here we present the careful calibration of compensation fields for the compensation of stray magnetic fields using the compensation coils described in chapter 1.2.

The Zeeman shift depends on the absolute value of the magnetic field

$$\left|\vec{B}\right| = \sqrt{B_{x_1}^2 + B_{x_2}^2 + B_{x_3}^2} \tag{3.2}$$

where B_{x_i} are the field components in three spatial directions. We apply a small magnetic field B_0 on the order of 200 mG in one direction, change the compensation B_{x_i} in another direction and look how the mw transition frequency depends on the applied compensation field. By finding the minimum of the function

$$B^2 = B_0^2 + B_{x_i}^2 \tag{3.3}$$

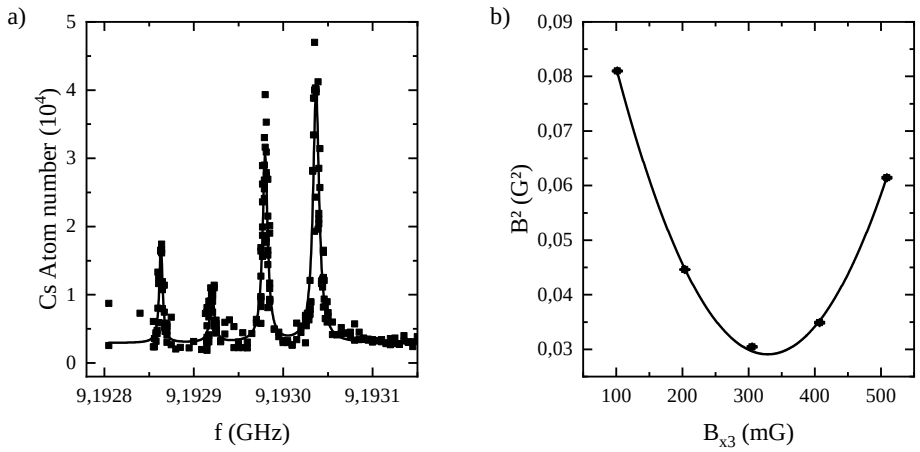

Figure 3.5: Calibration of magnetic field compensation via Cesium mw spin flip. a) shows an example spin flip for atoms transfered from $|3,3\rangle \rightarrow |4,4\rangle$, $|3,3\rangle \rightarrow |4,3\rangle$, $|3,3\rangle \rightarrow |4,2\rangle$ and $|3,2\rangle \rightarrow |4,3\rangle$ overlapped, $|3,2\rangle \rightarrow |4,2\rangle$ (left to right). The extracted magnetic field is $B = 165(1)\,\mathrm{mG}$. b) A total field calibration in vertical direction with an applied offset field of $171(1)\,\mathrm{mG}$ in other directions and a compensation at $B_{x_3} = 329(3)\,\mathrm{mG}$.

we find the value of the magnetic field component in the compensation direction. Figure 3.5a shows a spin flip measurement to extract the magnetic field by assigning the peaks to different transitions (see caption). Figure 3.5b shows a calibration example for the magnetic field in vertical direction, where the magnetic field is compensated when applying a field of $B_{x_3} = 329(3)\,\mathrm{mG}$. For north-south direction we measure $B_{x_1} = 234(4)\,\mathrm{mG}$ and in east-west direction we measure $B_{x_2} = 83(4)\,\mathrm{mG}$. The absolute value of the compensated magnetic field is $B_{total} = 412(6)\,\mathrm{mG}$.

3.4 Feshbach tomography

The experiments presented in part II of this thesis are performed either at magnetic fields between 150 G and 220 G for ^{6}Li , or between 700 G and 900 G for ^{6}Li-^{133}Cs. The magnetic field for these experiments is provided by the Feshbach coils described in chapter 1.2. A precise knowledge of the magnetic field landscape, the stability and the position of the atoms within this landscape is required to perform measurements with high magnetic field precision. Here we present a detailed description of the Feshbach coil magnetic field landscape using Cesium mw spectroscopy.

We perform tomographic measurements of the Feshbach fields in all three spatial directions. We create an ultracold cloud of Cesium atoms at different positions within the magnetic field landscape by changing the position of the reservoir trap. By applying a Cesium mw spin flip as described in the previous sections, we measure the magnetic field at a certain position. Due to a large expansion of the atomic cloud of approximately 170 µm within a spatially dependent magnetic field, only a slice of the atomic distribution

is transfered to the other spin state. By looking at the position of the transfered slice relative to the position on the camera, one gets an immediate measurement of a position dependent spin flip frequency f. This frequency is transfered into a magnetic field using the Breit-Rabi formula. Figure 3.6 shows the magnetic field tomography measurement in x_3 direction with a mw pulse length of 35 µs and maximal mw power. The position of the atomic slices is determined by the center position of a Gaussian fit to the atomic optical density distribution on the absorption picture. Points within 10 pixels (∼40 µm) are binned together. The pixel size is calibrated via the gravitational acceleration of an atomic cloud without external fields. Each point consists of at least 20 measurements and we show the standard error. The line is a quadratic fit yielding a center magnetic field of $B_0 = 1074.945(1)\,\mathrm{G}$ and a curvature factor of $\alpha = 274(6)\,\mathrm{m}^{-2}$ where the spatially dependent magnetic field is given by

$$\vec{B}(\vec{r}) = B_0 \begin{pmatrix} -\alpha x_1 x_3 \\ -\alpha x_2 x_3 \\ 1 + \alpha\left(x_3^2 - \frac{x_1^2+x_2^2}{2}\right) \end{pmatrix} \tag{3.4}$$

We perform a similar measurements in x_1, x_2 direction shown in figure 3.7. Here the calibration of the camera pixel size was performed comparing the expansion of a thermalized cloud in time of flight with the expansion in vertical direction. By situating the atomic cloud in the center of the Feshbach field we minimize the magnetic field uncertainty due to the curvature of the field. The magnetic field dependence on the current in the center of the field yields a calibration of $2.8033(5)\,\mathrm{G\,A^{-1}}$. We check the magnetic field calibration by calculating the field landscape using elliptic integrals [Bergeman et al., 1987]. We calculate an magnetic field dependence on the current of $2.8032\,\mathrm{G\,A^{-1}}$ and a curvature factor of $\alpha = 286(2)\mathrm{m}^{-2}$ which are in good agreement with our measurements.

The curvature of the Feshbach field induces a magnetic potential on atoms. With $E_{pot} = \mu\left|\vec{B}\right|$ where $\mu = \frac{dE}{dB}$ is the magnetic moment of the atoms. The lowest order of the potential landscape is of second order. Thus the potential landscape can be characterized by trapping frequencies similar to optical potentials given by

$$\omega_{x_{1/2}} = \sqrt{\frac{\alpha\mu B_0}{m}} \qquad\qquad \omega_{x_3} = \sqrt{2\frac{\alpha\mu B_0}{m}} \tag{3.5}$$

3.5 Magnetic Field Uncertainty

We finally summarize the previously obtained information to evaluate the total magnetic field uncertainty and their limitations:

- **Field inhomogeneities** are induced, as outlined above, by the curvature of the Feshbach field. The non optimal Helmholtz configuration leads to a non homogeneous field at the center of the coils. For an optimized atomic cloud position at the center of the coils we give an upper limit on the magnetic field curvature along the cloud of up to 8 mG at fields of 935 G.

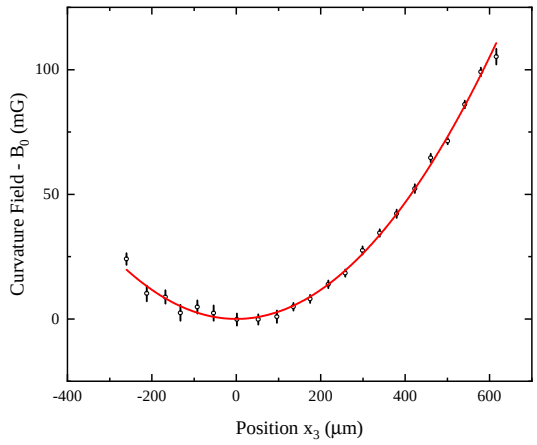

Figure 3.6: Tomography of the Feshbach magnetic field in x_3 direction. A fit to the data yields a center magnetic field of $B_0 = 1074.945(1)\,\mathrm{G}$ and a field curvature factor of $\alpha = 274(6)\,\mathrm{G\,m^{-2}}$. Each point consists of at least 20 measurements. The shown error is given by the standard error.

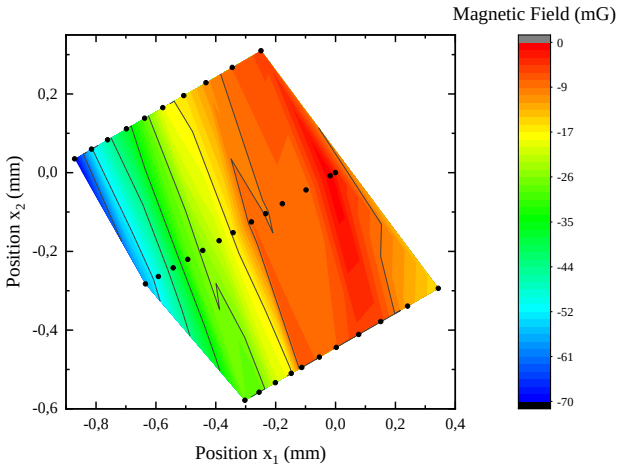

Figure 3.7: Tomography of the Feshbach magnetic field in x_1, x_2 directions. Each point consists of at least 20 measurements. The positions are presented relative to the center of the Feshbach field which is saddle point.

- **Long-term stability** are induced by field fluctuations over the course of one experiment consisting of multiple measurements. One experimental run takes about 8 s for pure Lithium samples and up to 15 s for ^{6}Li-^{133}Cs experiments. One measurement including magnetic field calibration can take up to several hours. During this time the thermal equilibrium of the magnetic field coils might change or the position of the optical dipole traps might fluctuate. These effects lead to a fluctuation of the

magnetic field over several experimental runs. The extensive characterization of the stability of the magnetic field leads to a maximum deviation from the mean of up to 8 mG [Ulmanis, 2017].

- **The length of the experimental sequence** as well as the current inducing the magnetic field have a large impact on the thermal equilibrium of the magnetic field coils. The energy dissipation leads to a difference in temperature which might alter the alignment and resistance of the magnetic field coils leading to changes of the field at the position of the atomic cloud. We minimize these effects by running one particular sequence for several hours to reach an equilibrium before taking a measurement. We estimate the effects on the field value to be up to 8 mG [Ulmanis, 2017].

- **The switching time** of the magnetic fields describes the characteristic time from the digital switching of the currents to the time where to magnetic field value is reached. The behavior of the magnetic field is described by the function $\Delta B \exp(-t/\tau)$ where ΔB is the step in the magnetic field and $\tau = 5(1)$ ms is the characteristic switching time given by the inductance of the coils. To separate this time from the hold time during an atom loss measurement we jump the field close to the resonance position we want to investigate. After a stabilization time of ≈ 20 ms we perform the final step to the measurement position. For this we use the Raman coils (see section 1.2), a pair of coils with smaller inductance. We reach the final magnetic field value within < 1 ms.

To evaluate to total systematic magnetic field uncertainty we take all of these effects into account. We assume them to be uncorrelated and thus take their quadratic sum. For measurements at magnetic fields around 180 G we end up with uncertainties of 10 mG. For fields around 700 G we calculate systematic uncertainties of 16 mG.

Summary

In summary we have presented our experimental apparatus for the production of an ultracold sample of ^{6}Li and a ^{6}Li-^{133}Cs mixture. We presented the ultra high vacuum setup that sets the environment for the ultracold atom experiment. We introduced the magnetic and electric fields used in the experiment for the manipulation and cooling of the atoms and presented our detection method. In the second chapter a closer look has been taken at the experimental sequence for the improved production of a degenerate ^{6}Li sample. An introduction to gray molasses cooling on the D_1-line of ^{6}Li as an optical sub-Doppler cooling method has been given. We presented the improved dipole trap loading via a spatially modulated optical dipole trap and the subsequent evaporative cooling into a degenerate ^{6}Li sample. We present the sequence for the production of a thermal ultracold ^{6}Li sample at temperatures between 100 nK and 300 nK and a sequence for the production of a thermal ultracold ^{6}Li-^{133}Cs mixture at temperatures between 900 nK and 200 nK. In the third chapter we investigated the magnetic field landscape of the experiment acting on the

atomic cloud. After introducing magnetic field dependent ^{6}Li radio-frequency and ^{133}Cs microwave spin-flip spectroscopy we presented our method for compensation of stray magnetic fields. Finally we presented the investigation of the curvature of the Feshbach field and we discussed the resulting magnetic field accuracies and concluded on absolute accuracies of 10 mG and 16 mG for measurements around magnetic fields of 180 G and 700 G respectively. The results of the first part of this thesis lay the ground for the experimental investigation of p-wave Feshbach resonances presented in the second part of the thesis.

Part II

Exploring p-wave Feshbach Resonances

4. Introduction to Atomic Collisions

In this chapter we introduce basic concepts of scattering theory and Feshbach resonances to lay the groundwork for the following studies of spin-spin and spin-rotation coupling in p-wave Feshbach resonances of ^{6}Li-^{133}Cs. We start by introducing basic scattering theory of atomic collisions at ultra low kinetic energies in section 4.1. We continue by introducing Feshbach resonances 4.2 followed by the description of the system Hamilton in 4.3 and finally the methods of measuring Feshbach resonances in section 4.4.

4.1 Basics of scattering theory

The concepts of inter atomic scattering at ultra low kinetic energies are well established.The presented introduction into inter atomic scattering theory closely follows the treatment of Dalibard [1999]. Other introductions and treatments of atomic two-body collisions at ultra low kinetic energy can be consulted for further information [Landau and Lifshitz, 1965; Jochain, 1983; Sakurai and Napolitano, 1994; Ketterle et al., 1999].

Scattering theory describes the interaction of two approaching atoms. Thus, the change of incoming states into outgoing states. The states interact via a potential $V(\vec{R})$ and a Hamiltonian in the center of mass frame

$$\left[-\frac{\hbar^2}{2\mu}\vec{\nabla}^2 + V(\vec{R})\right]\Psi(\vec{R}) = \frac{\hbar^2 k^2}{2\mu}\Psi(\vec{R}) \tag{4.1}$$

Here $\left|\vec{R}\right|$ is the inter particle separation, $\mu = m_1 m_2/(m_1+m_2)$ is the reduced mass of the atomic components, $\hbar$ is the Planck constant and $k = \sqrt{2\mu E/\hbar^2}$ is the wave vector given by the energy $E = E_{kin} + V(\vec{R})$. The energy of the system is chosen in a way, that for large inter atomic separations $|\vec{R}| = R \gg R_0$, where R_0 is the effective range of the potential $V(\vec{R})$, the potential energy vanishes $V(R \gg R_0) = 0$. For large atomic separation $R \gg R_0$ the solutions of equation 4.1 can be separated into an incoming plane wave $\Psi_i(R) = \mathrm{e}^{ikR}$ with momentum k and a scattered spherical wave $\Psi_f(R) = f(k,\phi)\frac{\mathrm{e}^{ikR}}{R}$ with amplitude $f(k,\phi)$

$$\Psi(R) = e^{ikR} + f(k,\phi)\frac{\mathrm{e}^{ikR}}{R} \tag{4.2}$$

The momentum dependent scattering cross-section into a solid angle Ω is then given by $d\sigma(k)/d\Omega = |f(k,\phi)|^2$. In the case of neutral atoms $V(\vec{R})$ can be described by a short-ranged isotropic Born-Oppenheimer molecular potential. In this case the wave function can be expand in spherical harmonics $Y_l^m(\phi,\psi)$:

$$\Psi(R) = \sum_{l=0}^{\infty} \sum_{m_l=-l}^{l} Y_l^{m_l}(\phi,\psi) \frac{\chi_{k,l,m_l}(R)}{R} \tag{4.3}$$

Here l is the relative angular momentum, m_l is its projection and $\chi_{k,l,m_l}(R)$ is the radial wave function depending on the wave number k. When solving the Hamilton from equation 4.1 using this wave function (4.3), we obtain the scattering amplitude for large R:

$$f(k,\phi) = \frac{1}{2ik} \sum_{l=0}^{\infty} (2l+1)(\mathrm{e}^{2i\delta_l(k)} - 1) P_l(\cos(\phi)) \tag{4.4}$$

Here $P_l(\cos(\phi))$ are the Legendre polynomials and $\delta_l(k)$ is the phase shift between the incoming and outgoing wave. The scattering amplitudes angular distribution depends only on the relative angular momentum l.

The radial part of the wave function $R_l = \chi_l(R)/R$ can be obtained by solving the Hamiltonian from equation 4.1 and inserting the angular solution from equation 4.4:

$$\left(\frac{d^2}{dR^2} + \frac{2}{R}\frac{d}{dR} - \frac{2\mu}{\hbar^2}\left[E - V_l(R)\right] \right) R_l(R) = 0 \tag{4.5}$$

Here $V_l(R) = V(R) + \frac{\hbar^2 l(l+1)}{2\mu R^2}$ is the total inter atomic Born-Oppenheimer potential including the centrifugal barrier for $l > 0$ (shown in figure 4.3b)). A simplified equation can be found when substituting $\chi_l(R) = R \cdot R_l(R)$, $\epsilon = 2\mu E/\hbar^2$ and $\tilde{V}(R) = 2\mu V_l(R)/\hbar^2$:

$$\frac{d^2}{dR^2}\chi_l(R) + \left[\epsilon - \tilde{V}(R)\right] \chi_l(R) = 0 \tag{4.6}$$

with the solution

$$\chi_l(R) \sim \sin\left(kR - l\frac{\pi}{2} + \delta_l(k) \right) \tag{4.7}$$

Here the scattering phase shift $\delta_l(k)$ is a measure of the effect of the whole potential on the collision. For collision energies E small compared the centrifugal barrier hight, the particle will not interact with the short range potential $V(R)$ and will simply be reflected at the centrifugal barrier. Therefore, we expect that for partial waves with $l > 0$ the scattering induced by $V(R)$ can be neglected at low scattering energies. Th phase shift scales as $\delta_l(k) \propto k^{2l+1}$ for low collisional energies $k \to 0$ [Wigner, 1948]. For a van-der-Waals potential with $V(R) \propto R^{-6}$, the scattering phase shift can be described as [1]

[1] The scaling $\delta_l(k) \propto k^{2l+1}$ is only valid for $l = 0$ and $l = 1$ for van-der-Waals potentials. Otherwise for $l > 1$ the scaling is given by $\delta_l(k) \propto k^4$ [Dalibard, 1999].

[Dalibard, 1999; Chin et al., 2010]

$$k^{2l+1}\cot(\delta_l(k)) = -\frac{1}{a_l} + \frac{1}{2}R_0^{1-2l}k^2 \tag{4.8}$$

Here a_0 is the so called s-wave scattering length with dimension m^{-1} and $a_1 = V_p$ is the p-wave scattering volume with dimension m^{-3}. [2]

To evaluate the scattering cross-section $\sigma(k)$ we need to take quantum statistics into account. For Bosonic particles we need to fulfill the symmetrization of the particle wavefunction. Fermionic particles need to fulfill the anti-symmetrization of the particle wavefunction. In terms of the differential cross-section this means $d\sigma(k)/d\Omega = |f(k,\phi) \pm f(k,\pi-\phi)|^2$. Where $+$ is used for Bosons and $-$ for Fermions. This means twice the contribution in the total scattering cross-section from the contributing partial waves even(odd) and an extinction of odd(even) partial waves for Bosons(Fermions)

$$\sigma_l(k) = \frac{8\pi}{k^2}\sum_l (2l+1)\sin^2(\delta_l(k)) \tag{4.9}$$

For Bosons(Fermions) the sum is only taken over even(odd) l. This leads to a total s-wave, cross-section of

$$\sigma_s(k) = \begin{cases} \frac{4\pi a^2}{1+k^2a^2} & \text{for distinguishable particles,} \\ \frac{8\pi a^2}{1+k^2a^2} & \text{for idendtical bosons,} \\ 0 & \text{for identical fermions} \end{cases} \tag{4.10}$$

For identical fermions only partial waves with $l = 1, 3, ..$ contribute to the cross-section. For the case that $k^2a^2 \gg 1$ is called unitarity regime and the cross-section becomes independent on a and only depends on the collisional energy k^2.

For p-wave elastic collisions for distinguishable particles the cross-section can be written as:

$$\sigma_p(k) = \frac{12\pi}{k_e^2}\frac{k^4}{(k^2 - \frac{1}{V_p k_e})^2 + \gamma_e^2/4} \tag{4.11}$$

where V_p is the scattering volume, k_e is one over the effective range and γ_e is a resonance width that we will further discussed in chapter 7.1.

In the following, we will give an introduction to Feshbach resonances. There we will see how the scattering volume V_p can be tuned via magnetic field.

4.2 Feshbach Resonances

Feshbach resonances have been studied in great detail [Chin et al., 2010; Gurarie and Radzihovsky, 2007; Timmermans et al., 1999; Köhler et al., 2006; Hutson and Soldán, 2006; Duine and Stoof, 2003]. In this section, we restrict our self to the description on

[2] We will later use $k_e = 1/R_0$ as another definition of the effective range

magnetically tunable Feshbach resonances with special focus on p-waveresonances, closely following the work of Moerdijk et al. [1995]. We start by introducing the effective Hamiltonian H of the system consisting of two parts. H_0 has Eigenstates of the form $\left|\{\alpha\beta\}\right\rangle$ that we call channels. For large inter atomic separation the states $|\alpha\rangle$ and $|\beta\rangle$ correspond to the internal states of single atoms α and β. V is an interaction, coupling the different channels. The scattering state Ψ is expand in the bases $\left|\{\alpha\beta\}\right\rangle$ with the atomic separation $\vec{R}$ dependent coefficient $\psi_{\{\alpha\beta\}}(\vec{R})$.

$$\Psi = \sum_{\{\alpha\beta\}} \psi_{\{\alpha\beta\}}(\vec{R}) \left|\{\alpha\beta\}\right\rangle \tag{4.12}$$

Using this bases be obtain a set of coupled differential equations for $\psi_{\{\alpha\beta\}}$. The ultra low collisional energy of ultracold atoms greatly reduces the number of channels relevant to the investigated system. Electronic ground states, low partial wave number l, symmetry arguments and conservation laws lead to a limited number of channels that can be separated into two subsets $\mathcal{P}$ and $\mathcal{Q}$ uncoupled under H_0. For scattering energies E large compared to the asymptotic energy of a channel, we call the channel an "open channel" and $\mathcal{P}$ the subspace of open channels. For scattering energies E below the asymptotic energy of a channel, we call the channel a "closed channel" and $\mathcal{Q}$ the subspace of closed channels.

Figure 4.1 shows an example of an open- and a closed channel with asymptotic energies below and above the scattering energy E respectively.

Using projection operators $\hat{\mathcal{P}}$ and $\hat{\mathcal{Q}}$ on the Hamiltonian H leads to two coupled equations projected on the respective subspaces:

$$(E - H_{\mathcal{P}\mathcal{P}})\Psi_{\mathcal{P}} = H_{\mathcal{P}\mathcal{Q}}\Psi_{\mathcal{Q}} \tag{4.13}$$

$$(E - H_{\mathcal{Q}\mathcal{Q}})\Psi_{\mathcal{Q}} = H_{\mathcal{Q}\mathcal{P}}\Psi_{\mathcal{P}} \tag{4.14}$$

With $\Psi_{\mathcal{P}} = \hat{\mathcal{P}}\Psi$, $\Psi_{\mathcal{Q}} = \hat{\mathcal{Q}}\Psi$, $H_{\hat{\mathcal{P}}\hat{\mathcal{P}}} = \hat{\mathcal{P}}H\hat{\mathcal{P}}$, $H_{\hat{\mathcal{Q}}\hat{\mathcal{Q}}} = \hat{\mathcal{Q}}H\hat{\mathcal{Q}}$ and $H_{\hat{\mathcal{P}}\hat{\mathcal{Q}}} = \hat{\mathcal{P}}H\hat{\mathcal{Q}}$, $H_{\hat{\mathcal{Q}}\hat{\mathcal{P}}} = \hat{\mathcal{Q}}H\hat{\mathcal{P}}$.

By introducing an energy $E^+ = E + i\delta$ with a small and positive δ perturbation, we can now solve equation 4.13 using the Green's operator $\frac{1}{E^+ - H_{\mathcal{Q}\mathcal{Q}}}$ leading to:

$$\Psi_{\mathcal{Q}} = \frac{1}{E^+ - H_{\mathcal{Q}\mathcal{Q}}} H_{\mathcal{Q}\mathcal{P}}\Psi_{\mathcal{P}} \tag{4.15}$$

We use this wave function to solve the Hamiltonian of equation 4.14, giving an effective description of scattering into the open channel.

$$\left(H_{\mathcal{P}\mathcal{P}} + H_{\mathcal{P}\mathcal{Q}}\frac{1}{E^+ - H_{\mathcal{Q}\mathcal{Q}}}H_{\mathcal{Q}\mathcal{P}}\right)\Psi_{\mathcal{P}} = E\Psi_{\mathcal{P}} \tag{4.16}$$

In this equation we can already read some of the key features of Feshbach resonances. An incoming open channel wave can be divided into two parts: $H_{\mathcal{P}\mathcal{P}}$ describes the propagation of the open channel wave in the open channel. The second term describes the

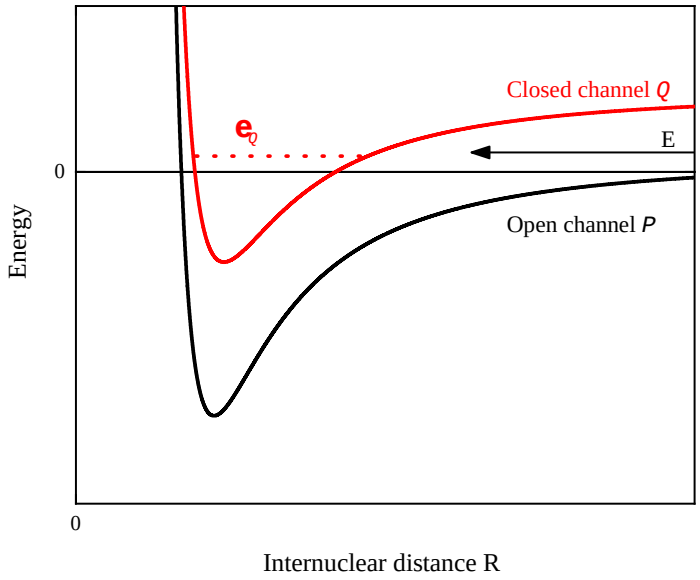

Figure 4.1: Working principle of Feshbach resonance: the scattering atoms with energy E couple to a near degenerate bound state ϵ_0 in the closed channel subspace $\mathcal{Q}$

temporary transition of the open channel wave in and out of the closed channel.

We can expand the Green's operator in discrete Eigenstates of $H_{\mathcal{QQ}}$ and if a single state with energy ϵ_0 is close to the energy E, omit all other states. This leads to the formal solution for $|\Psi_{\mathcal{P}}\rangle$ of equation 4.16

$$|\Psi_{\mathcal{P}}\rangle = \left|\Psi_i^+\right\rangle + \frac{1}{E^+ - H_{\mathcal{PP}}} H_{\mathcal{PQ}} |\psi_B\rangle \frac{\left\langle\psi_B\right| H_{\mathcal{QP}} \left|\Psi_i^+\right\rangle}{E - \epsilon_0 - \langle\psi_B| H_{\mathcal{QP}} \frac{1}{E^+ - H_{\mathcal{PP}}} H_{\mathcal{PQ}} |\psi_B\rangle} \tag{4.17}$$

Here $\left|\Psi_i^+\right\rangle$ is an Eigenstate of $H_{\mathcal{PP}}$ with incoming channel i. This scattering event can also be described in terms of the so called unitary scattering matrix S. S_{ij} describes the scattering amplitude from state i into state j where i and j are both open channels. In the case of ultracold collisions the open channel subspace reduces to a single state $i = j$ reducing the scattering matrix to a scalar. For the total energy E close to closed channel bound state with energy ϵ_0 (see figure 4.1) the S-matrix reads

$$S = S_{\mathcal{P}} \left(1 - \frac{i\Gamma}{E - \epsilon_0 - \Delta + \frac{i}{2}\Gamma}\right) \tag{4.18}$$

here $\Gamma = 2\pi |\langle\phi_{\mathcal{Q}}| H_{\mathcal{QP}} \left|\Psi_i^+\right\rangle|^2$ describes the coupling strength between the incoming state $\left|\Psi_i^+\right\rangle$ and the closed channel state $\langle\phi_{\mathcal{Q}}|$ via the coupling Hamiltonian $H_{\mathcal{QP}}$. Δ is the

resonance shift induced by the coupling of the scattering state to the closed channel and $S_{\mathcal{P}}$ is responsible for the scattering within the $\mathcal{P}$ subspace. For scattering energies $E > 0$ the molecular state becomes a quasi-bound state shifted with energy $\epsilon_0 + \Delta$ and width Γ. For energies $E < 0$ the width becomes $\Gamma = 0$ but the energy shift Δ remains.

In the two channel, single resonance approach the scattering matrix S is related to the scattering phase shift introduced in section 4.1 via $S(k) = \exp^{2i\delta_l(k)}$ [Moerdijk et al., 1995; Timmermans et al., 1999; Mies and Raoult, 2000; Köhler et al., 2006]. The scattering matrix can then be rewritten in terms of the lowest relevant partial wave which is $l = 1$ in our case

$$S_l(k) = e^{-2iV_{bg}k^3}\left(1 - \frac{2iCk^3}{iCk^3 - \epsilon_{res}}\right) \tag{4.19}$$

where V_{bg} is the background scattering volume, C is a positive constant describing the coupling between the open and the closed channel. $\epsilon_{res} = \epsilon_0 - \delta$ is the relative energy between the closed channel bound state ϵ_0 and the threshold energy. Here we can already see, that the background scattering volume V_{bg} is induced by the coupling of the incoming wave to the open channel described by $S_{\mathcal{P}}$. The second term is responsible for the coupling of the incoming wave to the closed channel state. Setting the left side equal to $\exp^{-2iVk^3}$ leads to

$$V = V_{bg} - \frac{C}{\epsilon_{res}} \tag{4.20}$$

In ultracold atoms the scattering states usually consist of two atoms in certain hyperfine states with magnetic moment $\mu_i(B) = \mu_A(B) + \mu_A(B)$ differing in spin quantum number from the closed channel state with magnetic moment $\mu_0(B)$, given by the singlet- and triplet character of the state with $\mu_0(B) = \langle S\rangle\, \mu_T(B)$. Here $\langle S\rangle$ describes the expectation value of the total spin. This leads to a magnetic field dependent relative energy $\epsilon_{res}(B) = (\mu_i(B_{res}) - \mu_0(B_{res}))(B - B_{res})$ around the magnetic field B_{res} where the relative energy is zero. We can write the resulting p-wave scattering volume in terms of the magnetic field dependence

$$V_p(B) = V_{bg}\left(1 - \frac{\Delta}{B - B_{res}}\right) \tag{4.21}$$

The scattering volume is shown in figure 4.2. Δ is the distance between the scattering pole B_{res} and the zero crossing of the scattering length (see figure 4.2) and is called the resonance width. The energy of the bound state, inducing the resonance is given by

$$E_b = \epsilon_0 + \Delta - \frac{i}{2}\Gamma(E_b) \tag{4.22}$$

where ϵ_{res} is the unperturbed resonance energy, dressed by the coupling strength of the scattering state to the open- and closed channel states Δ. For weakly coupling resonances Δ can be neglected. For p-wave resonances the bound state energy is given by [Gurarie

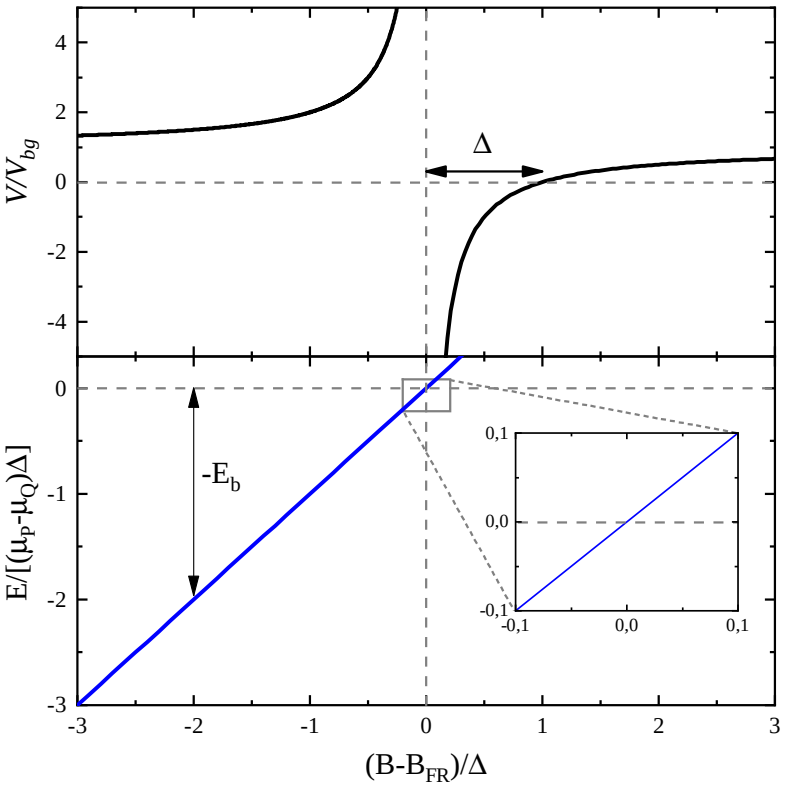

Figure 4.2: Behavior of scattering volume and binding energy close to a p-wave Feshbach resonance. Upper panel: scattering volume V_p versus the magnetic field according to equation 4.21. The zero-crossing is located at a distance Δ from the resonance position B_{FR}. Lower panel: energy of the weakly-bound molecular state given by equation 4.23. The bound state behavior differs significantly from the universal behavior at broad Feshbach resonances [Chin et al., 2010].

and Radzihovsky, 2007]

$$E_b = \frac{\hbar}{\mu V_p k_e} \tag{4.23}$$

and the width is given by[3]

$$\Gamma = \frac{2\sqrt{\mu}E^{3/2}}{k_e \hbar^2} \tag{4.24}$$

The coupling strength of a free scattering state with a molecular state is essential to the behavior of the scattering volume V_p, the bound state behavior E_b and the resonance width Γ_r. The coupling is induced by either the coulomb interaction contained in the molecular potentials V_S and V_T or the dipole-dipole Hamiltonian H_{ss} [Moerdijk et al., 1995], both discussed in the following section 4.3. Due to parity conservation of $l - l_{\mathcal{M}}$.

[3]In the following the resonance width Γ will be called Γ_r.

Feshbach resonances are classified by the angular momentum in the molecular channel $l_{\mathcal{M}}$ where $l_{\mathcal{M}} = 0$ are called s-wave resonances, $l_{\mathcal{M}} = 1$ p-wave resonances and so on. Since the parity conservation of $l - l_{\mathcal{M}}$ have to be even, the possible entrance channels for a corresponding Feshbach resonance are limited [Chin et al., 2010]. This means that p-wave resonances are induced by colliding atoms in a $l = 1$ entrance channel, coupling to a $l_{\mathcal{M}} = 1$ molecular channel. Due to angular momentum conservation also $m_l = m_{l_{\mathcal{M}}}$. In the following we use l and m_l both for the atomic scattering and the molecular state. As discussed in the previous section the centrifugal barrier in a p-wave entrance channel suppresses the cross-section with $\sigma \propto T^2$ [Wigner, 1948]. For ultracold collisions this means a "freezing out" of the p-wave interaction. However, resonant tunneling through the centrifugal barrier is possible which leads to a thinning of the resonance width.

4.3 The scattering Hamiltonian

In the previous sections we discussed atomic scattering of two particles in the p-wave channel with angular momentum of $l = 1$. We showed the resulting behavior of the scattering volume V_p and the bound state energy E_b and their dependence on the magnetic field. In this section we introduce the explicit form of the interaction potentials $V(\vec{R})$ and the scattering Hamiltonian H [Stoof et al., 1988; Moerdijk et al., 1995; Timmermans et al., 1999; Köhler et al., 2006]. In the following two chapters we will add two additional terms to the Hamiltonian and discuss corresponding observations and analysis. This section closely follows parts of Pires et al. [2014a] and Häfner [2017]. For simplicity and readability we will keep $\hbar = 1$ in this section.

The scattering Hamiltonian between two atoms A and B can be written as

$$H = T + (P_S V_S(R) + P_T V_T(R)) + H_{hf} + H_Z \tag{4.25}$$

The first term T describes the relative kinetic energy of the two atoms with $T = -\vec{\nabla}^2/(2\mu)$. The next term (shown in parentheses) describes the Born-Oppenheimer potentials $V_S(R)$ for the singlet potential ($S = 0$) and $V_T(R)$ for the triplet potential ($S = 1$) and the corresponding projection operators P_S and P_T. H_{hf} describes the hyperfine interaction and H_Z the magnetic Zeeman interaction for the electrons and the nuclei. In the following we will take a closer look at the latter three terms. More detailed introductions can be found in Stoof et al. [1988]; Moerdijk et al. [1995]; Timmermans et al. [1999]; Köhler et al. [2006]; Häfner [2017].

The molecular potential curves can be described in the Born-Oppenheimer approximation. Due to the fast electronic motion compared to the slow nuclear motion (resulting from the large mass difference) their motions can be separated. The attractive potential tail at large atomic separation R is induced by dipole-dipole interactions. We

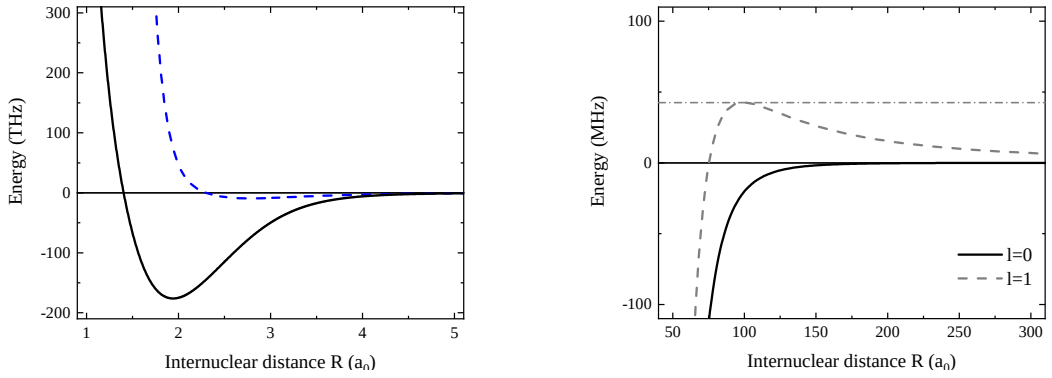

Figure 4.3: ^{6}Li-^{133}Cs molecular potential curves: (a) full singlet (black line) and triplet (blue dashed line) Born-Oppenheimer potentials in the electronic ground state. (b) long range van-der-Waals potential (see equation 4.26) including the centrifugal barrier for $l = 0$ (black line), $l = 1$ (gray dashed line) (see equation 4.28). The horizontal dash-dotted line represents the respective centrifugal barrier height given by equation 4.29.

written it as a power series of $1/R$:

$$V_{LR}(R) = -C_6/R^6 - C_8/R^8 - C_{10}/R^{10} \pm .... \tag{4.26}$$

Here C_6, C_8 and C_{10} are dispersion coefficients depending on details of the electronic configuration. Different methods exist to gain information about these parameters. They can be obtained from *ab initio* calculations [Derevianko et al., 2001] or including experimental information of bound states probed via photo association [Jones et al., 2006] or Feshbach spectroscopy [Chin et al., 2010].

The spins $\vec{s}_A$ and $\vec{s}_B$ of the individual atoms couple to a total spin $\vec{S} = \vec{s}_A + \vec{s}_B$ when the atom separation is short compared to the electron wave function. For atoms with single electron contribution to the total atomic spin e.g. alkali atoms, the total spin can either be of singlet nature ($S = 0$) or of triplet nature ($S = 1$). The different spin configurations lead to symmetric or anti-symmetric spatial wave functions for singlet and triplet spin configurations respectively. This leads to an enhanced (suppressed) electron-wave-function amplitude between the nuclei for the singlet (triplet) state. An electronic singlet configuration screens the repulsion of two the atom nuclei and leads to deep potential curve compared to the triplet configuration. An exchange term describes this difference

$$E_{ex}(R) = \pm A_{ex} R^{\gamma_{ex}} \exp\left(-\beta_{ex} R\right). \tag{4.27}$$

This term is negative for singlet and positive for triplet potentials. The details of electronic and nuclear configurations are incorporate in the parameters A_{ex}, γ_{ex} and β_{ex}. The parameters for our system can be found in Zhu et al. [2021a].

The potential at short range is dominated by Coulomb repulsion of the nucleus and Pauli blocking of the inner shell electrons. Figure 4.3a) shows the singlet and triplet potential fir ^{6}Li-^{133}Cs in black and dashed blue respectively.

As the last important contribution we add the centrifugal term shown in figure 4.3b) for ^{6}Li-^{133}Cs included as

$$H_{cf} = \frac{1}{2\mu}\frac{l(l+1)}{R^2} \tag{4.28}$$

For s-wave collisions with $l = 0$ the term is zero but for p-wave collisions with $l = 1$ the barrier height is given by

$$U_{cf} = \frac{1}{\sqrt{2C_6}}\left(\frac{12}{3\mu}\right)^{3/2} \tag{4.29}$$

For p-wave collisions of ^{6}Li the barrier is on the order of 8 mK and for ^{6}Li-^{133}Cs it is on the order of 2 mK.

The Hyperfine interaction term describes the coupling of the electronic angular momenta $\vec{j}_\beta$ to the nuclear spins $\vec{i}_\beta$ of the atom β. Here $\vec{j}_\beta = \vec{l_\beta} + \vec{s}_\beta$ where $\vec{l_\beta}$ is the electronic angular momentum and $\vec{s}_\beta$ is the electron spin. For alkali atoms in the electronic ground state $\vec{l_\beta} = 0$ leading to a hyperfine interaction Hamiltonian of

$$H_{hf} = \sum_{\beta=A,B} \alpha_\beta(R)\vec{s}_\beta \cdot \vec{i}_\beta \tag{4.30}$$

Here the function $\alpha_\beta(R)$ describes the molecular hyperfine coupling. For large internuclear separations R approaches the atomic hyperfine constants $\alpha_{\beta,hf}$ [Strauss et al., 2010]. For small internuclear distances the electronic distributions are distorted which leads to an R dependence of the coupling strength $\alpha_\beta(R)$.

The Zeeman term describes the coupling of the electron spins $\vec{s}_\beta$ and the nuclear spins $\vec{i}_\beta$ to an external magnetic field $\vec{B}$. The resulting Zeeman shifts can be seen in figure 3.1a and 3.1b for ^{6}Li and ^{133}Cs respectively. The shift is given by the Hamiltonian

$$H_Z = \sum_{\beta=A,B} \left(g_{s,\beta}\vec{s}_\beta + g_{i,\beta}\vec{i}_\beta\right)\mu_B\vec{B} \tag{4.31}$$

Here $g_{s,\beta}$ and $g_{i,\beta}$ describe the electronic and nuclear gyromagnetic ratio respectively. μ_B is the Bohr magneton. The Zeeman shift leads to an energy splitting of the different m projections of the electronic and nuclear spin.

The presented Hamiltonian H describes the scattering states but also the molecular states inducing Feshbach resonances introduced in section 4.2. The relative magnetic moment between the molecular state and the entrance channel of two colliding atoms is described within the Zeeman Hamiltonian. Figure 4.4 shows a schematic of the involved

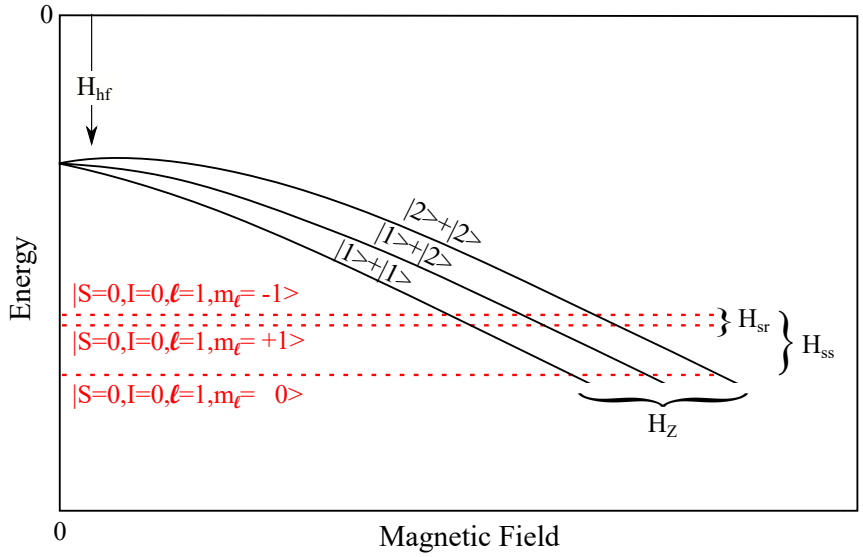

Figure 4.4: Schematic of p-wave Feshbach resonances in ^{6}Li for three different entrance channels $|1\rangle + |1\rangle$, $|1\rangle + |2\rangle$ and $|2\rangle + |2\rangle$. The Feshbach resonances occur at the magnetic fields where the free atomic scattering states (black) cross a molecular state (red). The magnetic field dependence of the states is induced by H_Z from equation 4.31, the molecular states are induced by H, we see the lowest hyperfine manifold induced by H_{hf} from equation 4.30. The splittings in the molecular states are induced by spin-spin interactions H_{ss} introduced in chapter 5 and spin-rotation interactions introduced in chapter 6. The splitting in the molecular state energies leads to a splitting in the Feshbach resonance positions. In the case of ^{6}Li the molecular states are almost complete singlet states and thus show now significant magnetic field dependence.

states emerging from the Hamiltonian in case of the ^{6}Li p-wave Feshbach resonances. p-wave Feshbach resonances can be found at the position of the crossing between the free scattering states (black) and the molecular states (red).

4.4 Measuring Magnetic Feshbach resonances

In this thesis we gain information about p-wave Feshbach resonances in ^{6}Li and ^{6}Li-^{133}Cs through so called atom loss spectroscopy. Next to bound state spectroscopy [Klempt et al., 2008; Regal et al., 2003; Bartenstein et al., 2005; Ospelkaus et al., 2006; Wu et al., 2012; Zürn et al., 2013] this is the most common method for the investigation of Feshbach resonances. Here we discuss how resonance poles can be found through atom loss. In chapter 7.1 we will go into more detail about the loss process and its consequences on the sample in the case of ^{6}Li in the lowest hyperfine stat. An inelastic process can lead to losses when the released energy leads to an increase of kinetic energy, large compared to the trapping potential. An elastic process leads to losses if a collision leads to redistribution

of kinetic energy such that the kinetic energy of an atom exceeds the trapping potential.

One-body-loss describe atom loss from a trap with no dependence on the atomic density. They are independent of Feshbach resonances and can happen either via background collisions with particles from the remaining vacuum gas or via absorption of resonant light [He et al., 2011]. In optical dipole traps despite the large detuning, due to the high power the trapping light leads to losses. One-body-losses usually lead to lifetimes of the atomic sample on the order of tens of seconds to minutes.

Two-body-losses describe atom loss from a trap with a dependence on the atomic density because two particles need to be close to each other to induce the loss process. An inelastic loss process can occur for two atoms changing internal states within a collision. For atoms in the energetically lowest channel $^6\mathrm{Li}|2\rangle \oplus ^6\mathrm{Li}|2\rangle$ or $^6\mathrm{Li}|2\rangle \oplus ^{133}\mathrm{Cs}|3,+3\rangle$ this process is suppressed, however it is possible for all other channels [Tung et al., 2013]. An elastic process can be evaporation where thermalization leads to losses when the gas sample is hot compared to the trap depth. Since thermalization depends on elastic two-body collisions this process depends on the scattering volume (see equation 4.11).

Three-body-losses describe atom loss from a trap with a dependence on the atomic density squared because three particles need to be close to each other to induce the loss process. In an inelastic process one free atom collides with a diatomic molecule. The molecular binding energy is released and shared between the free atoms and the molecule. Since the formation of the diatomic molecule depends on the position of the Feshbach resonance, this process also depends on the resonance position.

We conclude that a Feshbach resonance pole is accompanied by a loss maximum. We use this knowledge to determine the Feshbach resonance positions via magnetic field dependent atomic loss spectroscopy.

In the following two chapters we will first add the spin-spin interaction Hamiltonian H_{ss} to the previously introduced Hamiltonian H. We will see, that the spin-spin interaction lifts the degeneracy of the $m_l = 0, \pm 1$ molecular states. Further we will introduce the spin-rotation interaction Hamiltonian H_{sr} in chapter 6. There we will see, that this interaction lifts the degeneracy of the $m_l = -1, +1$ molecular states.

5. Spin-Spin interactions

In this chapter we present investigations on spin-spin interactions observed in ^{6}Li$\oplus^6$Li and ^{6}Li-^{133}Cs p-wave Feshbach molecules. The content of this chapter follows closely the publications Gerken et al. [2019]; Zhu et al. [2021b] and Zhu et al. [2021a] where we observed the dipolar splitting in high-resolution atom-loss spectroscopy of ^{6}Li and ^{6}Li-^{133}Cs p-wave Feshbach resonances for the first time.

Spin-spin interactions have been introduced in 1929 by Van Vleck [Van Vleck, 1929] as an additional perturbation to the diatomic molecular Hamiltonian to describe splittings in spectral lines. The splitting arises from an interaction lifting the degeneracy corresponding to different molecular rotational projections on the magnetic field axis.

The interaction can be separated into a first order effect, and a second order effect. The first order effect is the magnetic dipole-dipole interaction inducing the coupling between an electron spin and the magnetic field caused by the electron's magnetic moments. The second order effect is induced by the coupling of an electron spin to the magnetic field induced by the fast orbital motion of other electrons, and can thus be understood as a second order spin-orbit coupling effect [Strauss et al., 2010].

In Feshbach spectroscopy this effects give rise to a well established doublet splitting in p-wave Feshbach resonances [Ticknor et al., 2004; Pilch et al., 2009; Wang et al., 2011; Repp et al., 2013; Wang et al., 2013; Dong et al., 2016; Sawyer et al., 2017] or a triplet splitting in d-wave Feshbach resonances [Cui et al., 2017]. This doublet features in p-wave resonances corresponds to the two different projections m_l of the orbital angular momentum l onto the external magnetic field. Potassium for example exhibits a splitting of $\sim 0.4\,\mathrm{G}$ at a magnetic field of 199 G between the $m_l = 0$ and the $|m_l| = 1$ states [Ticknor et al., 2004].

Figure 5.1 shows a schematics of the two different configurations.

We introduce the dipole-dipole interaction Hamiltonian H_{ss} in its effective form [Strauss et al., 2010] that is added to the total Hamiltonian H introduced in chapter 4.1

$$H_{ss} = \frac{2}{3}\lambda(R)\langle 3S_Z^2 - S^2\rangle \tag{5.1}$$

where S_Z is the projection of the total electronic spin onto the molecular axis Z, S is the total electronic spin and $\lambda(R)$ is the dimensionless spin-spin coupling constant.

$\lambda(R)$ is a function of internuclear separation R that includes the magnetic dipole-dipole interaction [Stoof et al., 1988; Moerdijk et al., 1995] with a $1/R^3$ dependence and

the second order spin-orbit interaction with exponential R-functions [Mies et al., 1996; Kotochigova et al., 2001]. The exponential R-function effectively describes an overlap integral of the two atoms electronic distribution [Pashov et al., 2007].

$$\lambda(R) = -\frac{3}{4}\alpha^2 \left(\frac{1}{R^3} + \sum_{\beta=i} a_{SOi} \exp\left(-b_i R\right) \right) \tag{5.2}$$

Here α is the fine-structure constant and a_{SOi} and b_i for atom A and B are adjustable parameters that we will discuss later.

The dipolar splitting in ^{6}Li p-wave Feshbach resonances at 160 G was predicted to be ~ 10 mG by Chevy et al. [2005]. Despite the many studies on ^{6}Li p-wave Feshbach resonances [Zhang et al., 2004; Schunck et al., 2005; Nakasuji et al., 2013; Yoshida et al., 2018; Waseem et al., 2017, 2018], so far this very small splitting has not been resolved due to insufficient magnetic field resolution. In another experiment p-wave molecules in the $|m_l| = 1$ state were selectively formed in an optical lattice without resolving the dipolar splitting by restricting possible collision channels [Waseem et al., 2016]. Other studies of the molecular binding energy and lifetime neglected this effect [Fuchs et al., 2008; Inada et al., 2008; Maier et al., 2010]. In ^{6}Li-^{133}Cs , studies are scarce but the splitting has been observed [Repp et al., 2013].

In section 5.1 we report on high-resolution trap-loss spectroscopy on three ^{6}Li p-wave Feshbach resonances in the two lowest hyperfine states. Dipolar splittings in all three resonances are resolved between 13(1)mG and 6(1)mG. We study systematic effects of the sample temperature on the resonance with the largest splitting. In section 5.2 we report on observation of spin-spin splitting in ^{6}Li-^{133}Cs on five different p-wave Feshbach resonances with splittings between 75(12) mG and 422(5) mG. Also here we study systematic effects of the sample temperature on the resonance at 663 G.

5.1 Spin-Spin Splitting in ^{6}Li

In this section we present our experimental observations on the spin-spin splitting in ^{6}Li. A detailed description of the experimental apparatus and sample preparation has been given in chapter 2. We briefly recap the sample preparation. The two lowest hyperfine states $|2\rangle$=$|1/2, -1/2\rangle$ and $|1\rangle$=$|1/2, 1/2\rangle$ are captured in the cigar shaped optical dipole trap we call dimple trap. The cloud is evaporatively cooled for 5 s at a magnetic field of ~ 890 G which corresponds to an s-wave scattering length a_{12} between the hyperfine states $|1\rangle$ and $|2\rangle$ of $a_{12} = -8000\, a_0$. We selectively populate either one of the spin states by removing the other one with a short resonant light pulse or we keep the mixture. The starting conditions for the experiment are 3×10^4 atoms in each spin state at a temperature of $T \approx 140$ nK with trapping frequencies of $\omega = 2\pi \times (30, 170, 180)$Hz. This results in a peak atomic density of $n = 1.6(1) \times 10^{11}\mathrm{cm}^{-3}$ and $T/T_F = 0.53(4)$ where T_F is the Fermi temperature of the system. We hold the sample of atoms for three different spin configurations at different magnetic fields. Figure 5.2 shows magnetic-field-dependent loss

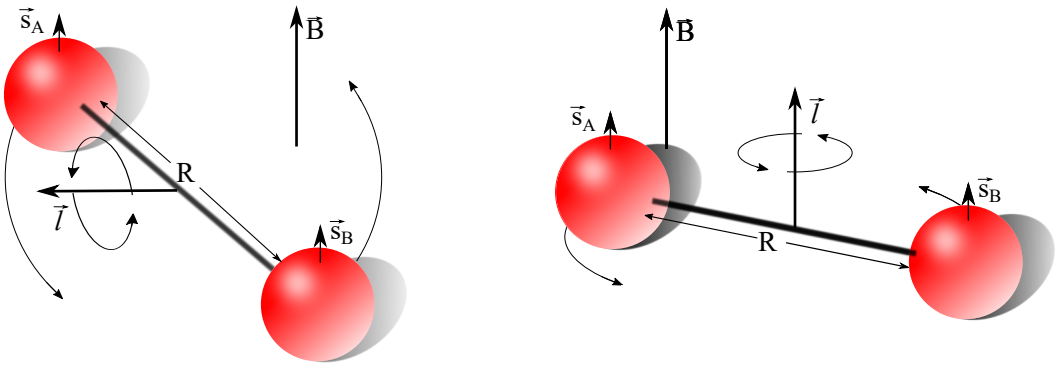

(a) $m_l = 0$ **(b)** $m_l = \pm 1$

Figure 5.1: Schematics of the spin-spin coupling in a weakly bound dimer AB consisting of one-electron atoms A and B separated by a distance R rotating with nuclear angular momentum $\vec{l}$ in an external magnetic field $\vec{B}$. The electron spins are denoted by $\vec{s}_i$, where $i = A, B$. Spin-spin interaction lifts the degeneracy between the $m_l = 0$ and $m_l = \pm 1$ states depicted by a) and b), respectively. b) shows $m_l = +1$ representing both $m_l = \pm 1$. Two effects lead to the spin-spin splitting: (1) the coupling between an electron spin and magnetic fields caused by the electron's magnetic moment, (2) the coupling of the electron spin to the magnetic fields caused by the fast orbital motion of the other electrons. The second effect is a second order spin-orbit coupling effect.

spectroscopy for the three different samples consisting of a) $|1\rangle\oplus|1\rangle$, b) $|1\rangle\oplus|2\rangle$ and c) $|2\rangle\oplus|2\rangle$ at magnetic fields of 159 G, 185 G and 214 G, respectively. The hold times vary for each resonance with a) 500 ms, b) 150 ms and c) 100 ms. The remaining atoms are detected via absorption imaging.

The points are taken in random magnetic field order to prevent systematic shifts over time. To calibrate the magnetic field we use a radio-frequency spin flip on lithium as described in section 3.1 where we also discuss the magnetic field uncertainty arising from the inferred magnetic field using the Breit-Rabi formula. The main uncertainty derived from the calibration measurements come from day-to-day drifts. Another contribution is the residual field curvature along the long axis of the atomic cloud. The absolute uncertainty is determined to be 10 mG.

To extract information from the measurements we fit Gaussian functions to the doublet structure of the respective loss measurements. We extract the loss peak position $B^e_{|m_l|}$ and the loss width in terms of the full width at half maximum $w^e_{|m_l|}$. The resonance at 185 G is fitted with global loss peak positions $B^e_{|m_l|}$ and independent $w^e_{|m_l|}$ and loss amplitudes to both spin state measurements. We define the splitting between the loss peaks as $\delta^e_{ss} = B^e_0 - B^e_1$. All extracted information is presented in table 5.1. We find splittings of 10(1)mG, 6(1)mG and 13(1)mG for the Feshbach resonances at 159 G, 185 G and 214 G, respectively.

The experimentally obtained splittings δ^e_{ss} are compared with theoretical splittings δ^{cc}_{ss}

Table 5.1: ^{6}Li p-wave Feshbach resonances position $B_1^e(G)$, width $w^e_{|m_0|}$ and $w^e_{|m_l|}$, doublet splitting $|B_1^e - B_0^e| = \delta^e_{ss}$ and theoretical doublet splitting δ^{cc}_{ss}. The experimental values are obtained by fitting multi peak Gaussian functions to the loss spectra shown in figure 5.2. For the resonance at 185 G, both spin states are fitted with a shared loss peak position $B^e_{|m_l|}$ and independent widths $w^e_{|m_l|}$ and loss amplitude. Both results are listed (the upper row for $|1\rangle$ and the lower one for $|2\rangle$). Errors are given in the determination uncertainty (first number in parentheses) and the systematic uncertainty of 10 mG (second number in parentheses). Coupled channel scattering calculations to obtain δ^{cc}_{ss} are performed for a relative kinetic energy of $k_B \times 140$ nK, matching with the experimentally measured temperature.

	B_1^e(G)	w_0^e(mG)	w_1^e(mG)	δ^e_{ss}(mG)	δ^{cc}_{ss}(mG)
$\|1\rangle\oplus\|1\rangle$	159.097(1)(10)	6(2)	17(2)	10(1)	10
$\|1\rangle\oplus\|2\rangle$	185.091(1)(10)	10(1)	5(2)	6(1)	4
	185.091(1)(10)	9(1)	5(1)	6(1)	4
$\|2\rangle\oplus\|2\rangle$	214.825(1)(10)	7(2)	10(1)	13(1)	13

obtained through coupled-channel calculations. The assignment of the quantum numbers $|m_l|$ in figure 5.2 is also obtained through the coupled-channel calculations. The observed doublet splittings are in very good agreement with a coupled-channel calculation including an effective spin-spin interaction as presented in chapter 5, similar to the procedure in the work by Knoop et al. [2009]. Our observations agree very well with previous predictions [Chevy et al., 2005; Fuchs et al., 2008].

Effects of finite temperature are caused by systematic effects on Feshbach resonances in atom-loss spectra. Figure 5.3a shows temperature dependent atom-loss spectra of the ^{6}Li p-wave Feshbach resonance at 214 G for temperatures $T \leqslant 300$ nK. To vary the temperature we stop evaporation at different trap depth. For temperatures above $T > 300$ nK the splitting becomes unresolved due to temperature broadening. Additionally the lineshape becomes asymmetric. In figure 5.3b we present the loss peak positions $B^e_{|m_l|}$ and the loss width $w^e_{|m_l|}$ extracted from figure 5.3a via a double Gaussian fit to the data.

Due to the asymmetric Maxwell-Boltzmann distribution, asymmetries in the loss shapes might arise if the temperature width is large compared to the loss resonance width. Averaging over the Maxwell-Boltzmann distribution also leads to a shift in the resonance center position. Saturation arises within the unitarity regime where the collision energy is large compared to the resonance energy [Ticknor et al., 2004; Dong et al., 2016; Zhang et al., 2004; Waseem et al., 2018, 2016]. This makes it impossible to resolve magnetic resonance splittings below magnetic fields of order $3k_BT/2\delta\mu$ [Waseem et al., 2018, 2016]. Here $\delta\mu$ is the relative magnetic moment between the molecular and the atomic state with $\delta\mu = k_B \times 118(8)\,\mu\mathrm{K\,G^{-1}}$ [Fuchs et al., 2008]. To ensure a magnetic field resolution of ~ 1 mG at the resonance at 214 G, thus we need temperatures below $T < 0.7\,\mu$K.

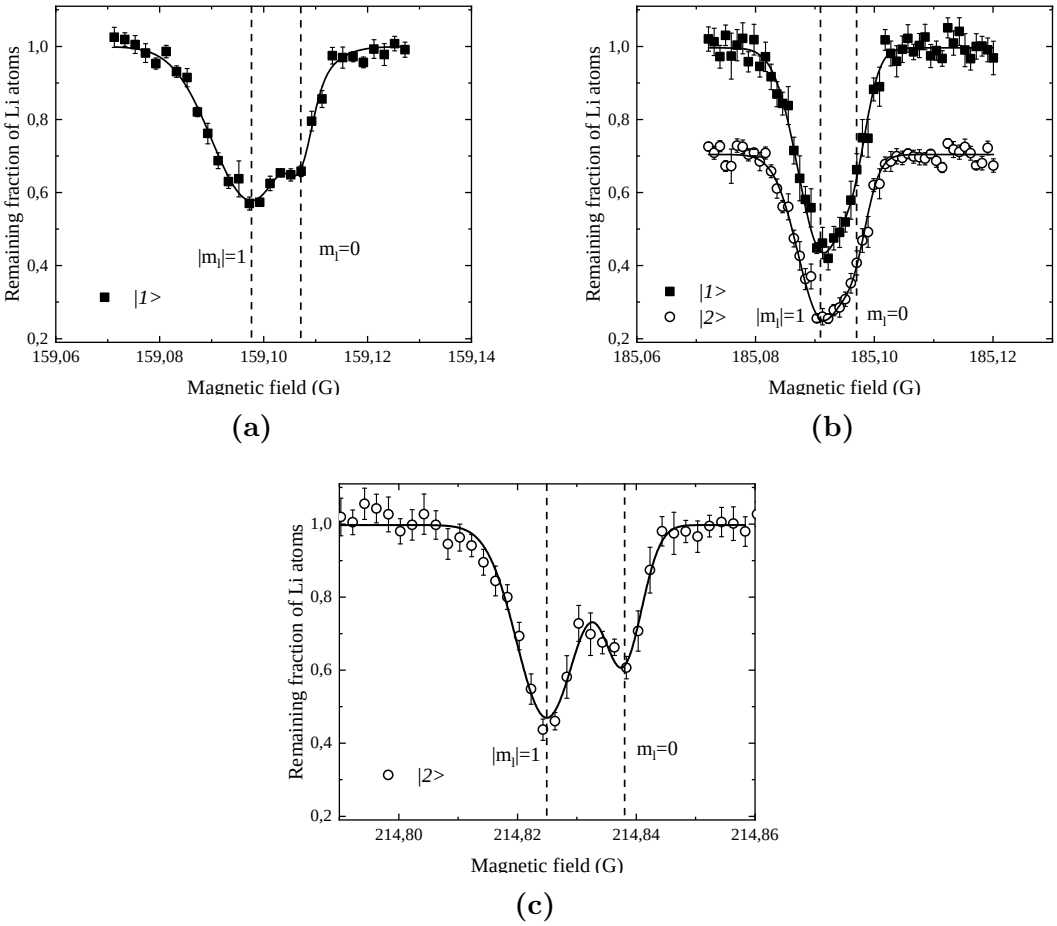

Figure 5.2: ^{6}Li p-wave Feshbach resonances in the a) $|1\rangle\oplus|1\rangle$, b) $|1\rangle\oplus|1\rangle$ and c) $|2\rangle\oplus|2\rangle$ entrance channels observed as atomic-loss features. The figure shows the remaining fraction of ^{6}Li atoms in the $|2\rangle$ spin state (solid squares) or the $|1\rangle$ spin state (open circles) after a) 500 ms, b) 150 ms and c) 100 ms. All three resonances show doublet structures. Quantum numbers $|m_l|$ are assigned to the peaks according to the theoretical modeling, described in the text. The data b) of spin-state $|1\rangle$ is vertically shifted to avoid overlapping with that of $|2\rangle$. The solid curves are fits with double-Gaussian functions. We extract the resonance positions $B^e_{m_l}$ (indicated by vertical dashed lines) and widths $w^e_{m_l}$ and listed them in table 5.1.

At lower temperature the resonance peak moves to lower magnetic fields as expected [Ticknor et al., 2004]. We approximate the temperature dependence with a linear fit to the loss peak position. We get resonance position slopes of 16(3) mG µK^{-1} and 10(3) mG µK^{-1} for the $m_l = 0$ and $|m_l| = 1$ peaks respectively. The zero temperature positions are given by $B^e_0(T = 0) = 214.824(1)(10)$G and $B^e_1(T = 0) = 214.837(1)(10)$G. Even though the slopes are slightly different for the two $|m_l|$ components, the splitting δ^e remains almost constant within the experimental uncertainty within the observed temperature range. For zero temperature we extrapolate a splitting of 13(1) mG which is in very good

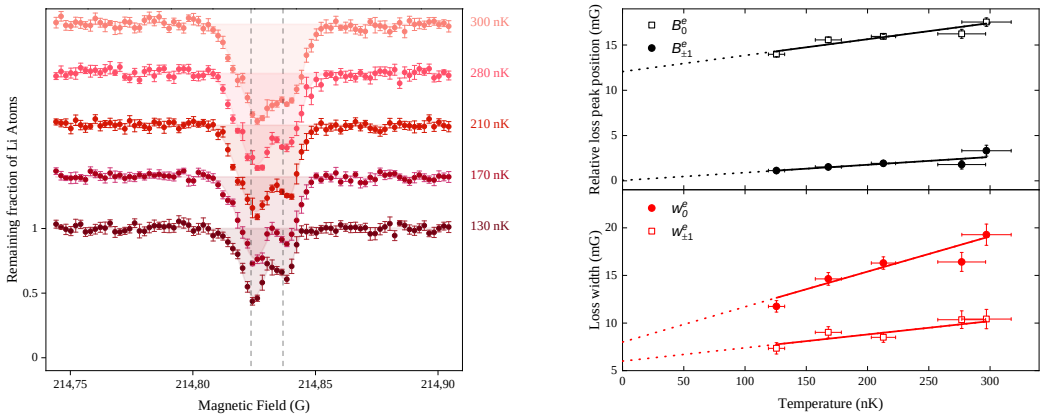

(a) **(b)**

Figure 5.3: Temperature dependence of atomic-loss spectroscopy near the 214 G ^{6}Li p-wave Feshbach resonance. a) Loss spectrum at different sample temperatures between 130 nK and 300 nK. The baselines of the profiles are shifted according to their temperature in order to avoid overlap of the curves. The data are fitted using a double-Gaussian function. We extract the loss peak positions $B^e_{|m_l|}$ and widths $w^e_{|m_l|}$. The dotted vertical lines shows the extrapolated peak positions of B^e_1 (left) and B^e_0 (right) at zero temperature at 214.824 G. (b) $B^e_{|m_l|}$ (black symbols) and $w^e_{|m_l|}$ (red symbols) of the observed loss features at different T for the $|m_l| = 1$ (solid circles) and $m_l = 0$ (open squares) components. $B^e_{|m_l|}$ are referenced to the zero-temperature value of B^e_1 at 214.824 G. The lines are linear fits to the data.

agreement with the coupled-channel calculations and previous predictions [Chevy et al., 2005]. Waseem et al. [2017, 2018] describe a Breit-Wigner theoretical approach explaining different slopes for two- and three-body loss processes. Assuming k_BT as the smallest energy scale, we estimate a resonance shift og $5k_B/2\delta\mu = 21.2\,\mathrm{mG\,\mu K^{-1}}$ and $k_B/\delta\mu = 8.5\,\mathrm{mG\,\mu K^{-1}}$ for two- and three-body loss processes respectively. The experimentally obtained slopes of $16(3)\,\mathrm{mG\,\mu K^{-1}}$ and $10(3)\,\mathrm{mG\,\mu K^{-1}}$ indicate contributions from both two- and three-body loss to the observed temperature dependence. For a loss resonance width which is small compared to the temperature width Chevy et al. [2005] calculates a slope of $11.1\,\mathrm{mG\,\mu K^{-1}}$ for a two-body loss process. For a deeper understanding of the temperature dependence through the loss mechanisms, time-resolved measurements are necessary.

For the observation of the loss width we obtain zero temperature width of $w^e_0(T = 0) = 6(1)\,\mathrm{mG}$ and $w^e_1(T = 0) = 8(1)\,\mathrm{mG}$ with slopes of $14(4)\,\mathrm{mG\,\mu K^{-1}}$ and $37(7)\,\mathrm{mG\,\mu K^{-1}}$ for the $m_l = 0$ and $|m_l| = 1$ components, respectively. The observed width includes the resonances intrinsic width Γ_r [Chevy et al., 2005; Waseem et al., 2017, 2018], dimer lifetime Λ_{ad} [Chevy et al., 2005; Waseem et al., 2017, 2018] and other experimental broadening effects such as the trap-induced density inhomogeneity, magnetic field noise and hold time. The observed width for all measured temperatures is large compared to the temperature

width with $w^e(T) > k_B T/\delta\mu$. From this one may infer that $\Gamma_r \hbar \gg k_B T$. This is also backed by the symmetry of the loss spectra. However, this disagrees with estimations of Γ_r extraced from the temperature- and interaction-strength-dependent two- [Chevy et al., 2005; Waseem et al., 2017] and three-body [Waseem et al., 2018] loss rate constants near the p-wave resonances above the Fermi temperature.

In conclusion we have performed high-resolution atom-loss spectroscopy of p-wave Feshbach resonances in an optically trapped ultracold ^{6}Li gas. We measured splittings of 10(1) mG, 6(1) mG and 13(1) mG on all three p-wave resonances at 159 G, 185 G and 214 G respectively. We assigned the different loss peaks to different absolute projections of the orbital angular momentum $|m_l|$ with a full coupled-channel calculation including spin-spin interactions. We showed that low temperatures are essential to resolve the splitting since the splitting itself only slightly depends on the temperature. The temperature dependence of the loss feature width however limits the resolution. Resolving the predicted dipolar splitting of Feshbach resonances in ^{6}Li provides a good starting point for further investigations in the direction exploring the individual control of $|m_l| = 0, 1$ scattering processes [Günter et al., 2005; Peng et al., 2018].

5.2 Spin-Spin Splitting in ^{6}Li-^{133}Cs

In this section we report on high-resolution trap-loss spectroscopy on five ^{6}Li-^{133}Cs p-wave Feshbach resonances $|\alpha\rangle = |1/2, -1/2\rangle \oplus |3, +3\rangle$ and $|\beta\rangle = |1/2, 1/2\rangle \oplus |3, +3\rangle$. Dipolar splittings on all five resonances are resolved. Observations on spin-rotation splitting is also observed and discussed in chapter 6.1. Splittings between 76(12) mG and 422(5) mG are observed. We study systematic effects of the sample temperature on the resonance at 663 G. This section is based in parts on the publications Zhu et al. [2021b,a].

A detailed description of the sample preparation has been given in chapter 2.5. We briefly recap the sample preparation. We prepare an optically trapped ultracold mixture of ^{6}Li-^{133}Cs atoms by means of standard laser-cooling techniques. The ^{133}Cs atoms are optically pumped into the absolute ground state $\left|f = 3, m_f = 3\right\rangle$ via degenerate Raman sideband cooling and loaded into the optical dipole trap we call reservoir trap. The ^{6}Li atoms in the ground state manifold $|f = 1/2>$ are loaded into another cigar shaped trap we call dimple trap, located 1 mm away from the reservoir trap. Both clouds are evaporatively cooled simultaneously at a magnetic field of 896 G where $a_{CsCs} = 320\, a_0$ and $a_{LiLi} = -8000\, a_0$. The combination of the two species is done at a field of 907 G. Lithium is spin polarized by removing one spin state via a short resonant light pulse. Finally both species are trapped in the dimple trap with 5×10^4 Cesium and 3×10^4 Lithium atoms at 430 nK. The trapping frequencies are $\omega_{Cs} = 2\pi \times (12, 173, 162)$Hz and $\omega_{Li} = 2\pi \times (44, 388, 388)$Hz. This corresponds to peak densities of $n_{Cs} = 2.7 \times 10^{12}\text{cm}^{-3}$ and $n_{Li} = 2.2 \times 10^{11}\text{cm}^{-3}$.

We perform high-resolution trap-loss spectroscopy by measuring the remaining fraction of ^{6}Li and ^{133}Cs atoms after optimized holding times in the trap. Holding times vary between 500 ms for the resonance at 663 G and 10 s for the resonance at 658 G. Magnetic

fields are calibrated as introduced in chapter 3 by a radio-frequency spin flip on Lithium and the Breit-Rabi formula. Absolute magnetic field uncertainties are determined to be 16 mG and are caused by long-term drifts, residual field curvatures along the long axis of the trap and calibration uncertainties.

Figure 5.4 shows five p-wave Feshbach resonances at magnetic fields between 658 G and 764 G Lithium and Cesium. In this section we focus on the observed spin-spin splitting, visible in all five resonances. We assign each peak with a quantum number $|m_l|$ according to a full coupled-channel calculation. We use Gaussian fits to extract the loss resonance positions $B^e_{m_l}$ where we use $B^e_{|m_l|=1} = \frac{B^e_{+1}+B^e_{-1}}{2}$, the loss width w^e_0 and the spin-spin splitting $\delta^e_{ss} = \frac{B^e_{+1}+B^e_{-1}}{2} - B^e_0$. These parameters are all listed in table 5.2 alongside the theoretical value of the spin-spin splitting δ^{cc}_{ss} extracted from a full coupled-channel calculation at a collision energy corresponding to a temperature of 430 nK. The observed splittings δ^e_{ss} are very large compared to the resonance width of ~ 20 mG, such that they are well resolved.

To account for the observed splitting, spin-spin interactions are included in the full coupled channel calculation presented in equation 5.1. For H_{ss} the diagonal parts give rise to the doublet splitting between the $m_l = 0$ and $|m_l| = 1$ states with an energy difference of

$$\Delta E_{ss} = \frac{1}{2}\langle\lambda(R)\rangle\langle 3S_z^2 - S^2\rangle \tag{5.3}$$

Here $\langle 3S_z^2 - S^2\rangle$ are expectation values calculated with the spin parts of the close-channel wave function. Off-diagonal parts in m_l are too small at high magnetic fields to cause a significant splitting of the $|m_l| = 1$ components (see Ref [Park et al., 2012] at low magnetic fields). The full spin-spin coupling parameters $\langle\lambda\rangle$ as introduced in equation 5.2 included in the full coupled channel calculation.

As described in the introduction of this chapter the $1/R^3$ term describes the direct magnetic dipole-dipole interaction [Stoof et al., 1988; Moerdijk et al., 1995]. The second order spin-orbit interactions are included with an biexponential R-function [Mies et al., 1996; Kotochigova et al., 2001]. The function shows a dominance of the first order term for large R and a dominance of the second order term for small R.

The energy splittings from equation 5.3 are translated into magnetic field splittings δ_{ss} via the differential magnetic moment μ_{rel} between closed and open channel. Table 5.2 shows $\langle\lambda\rangle$ calculated from these splittings in units of the rotational energy B_v which is given by $B_v = \hbar^2/(2\mu R^2)$. By fitting the full coupled channel calculation to the observed splitting δ^e_{ss}, we determine the free parameters in equation 5.2 to be: $a_{so1} = -1.99167$, $a_{so2} = -0.012380$, $b_1 = 0.7$ and $b_2 = 0.28$. Table 5.2 also shows the experimentally measured $\langle\lambda^e\rangle$ gained via

$$\langle\lambda^e\rangle = -2\mu_{rel}\frac{\delta^e_{ss}}{\langle 3S_z^2 - S^2\rangle} \tag{5.4}$$

where μ_{rel} and $\langle 3S_z^2 - S^2\rangle$ are obtained from the full coupled channel calculation.

In addition to the shown measurements of figure 5.4 we perform temperature dependent

Table 5.2: Dipole-dipole splitting in ^{6}Li-^{133}Cs p-wave Feshbach resonances observed for different spin channels $|\alpha\rangle = {}^6\text{Li}|1/2,+1/2\rangle \oplus {}^{133}\text{Cs}|3,+3\rangle$ and $|\beta\rangle = {}^6\text{Li}|1/2,-1/2\rangle \oplus {}^{133}\text{Cs}|3,+3\rangle$. The resonances are observed at magnetic field B_0^e and the corresponding loss width w_0^e. δ_{ss}^e is the splitting observed induced by the spin-spin interaction. The numbers in parentheses give the uncertainties in the determination of B_0^e, w_0^e and δ_{ss}^e. The systematic uncertainty is shown for B_0^e in the second bracket. δ_{ss}^{cc} shows the corresponding theoretical value of the splitting obtained from the full coupled-channel calculations for a relative kinetic energy corresponding to the temperature 430 nK. $\langle\lambda^e\rangle$ shows the effective spin-spin parameter calculated from the measured splitting δ_{ss}^e, the relative magnetic moment μ_{rel} and the expectation value $\langle 3S_z^2 - S^2\rangle$ as described in equation 5.2.

	$B_0^e(G)$	$w_0^e(mG)$	$\delta_{ss}^e(mG)$	$\delta_{ss}^t(mG)$	$\langle\lambda^e\rangle(10^{-3}B_v)$
$\|\alpha\rangle$	662.822(3)(16)	21(1)	224(4)	228.5	-7(1)
	713.632(4)(16)	15(1)	422(5)	419.5	-8(1)
$\|\beta\rangle$	658.080(10)(16)	25(3)	75(12)	81.5	-6(1)
	708.663(3)(16)	16(1)	228(4)	232.5	-7(1)
	764.201(1)(16)	21(1)	421(1)	423	-8(1)

high-resolution trap-loss spectroscopy on the 663 G p-wave resonance at temperatures between 210 nK and 840 nK. The measured spectra are presented in figure 5.5a. Also here we first focus on the spin-spin splitting and discuss the splitting of the $m_l = \pm 1$ states in section 6.1. Similar to the temperature dependent observations on the ^{6}Li p-wave Feshbach resonances, also here the resonance positions shift to lower fields. The splitting however stays resolved over the whole temperature range. We extract information about the loss peak positions $B_{|m_l|}^e$ and the loss width w_0^e by fitting multiple Gaussian functions to the spectra. The extracted information is presented in figure 5.5b.

The loss peak positions B_0^e and $B_{\pm 1}^e$ are shown for Lithium and Cesium. The data is presented such that $B_0^e = 0$ at zero temperature, shifted by 662.819(3) G. To lowest order we approximate the data by linear functions. The slopes for the loss peak positions give $25(2)\,\text{mG}\,\mu\text{K}^{-1}$ and $29(5)\,\text{mG}\,\mu\text{K}^{-1}$ for the B_0^e and $B_{\pm 1}^e$ peaks respectively. The splitting δ_{ss}^e does not change significantly over the whole range and is $\delta_{ss}^e(T = 0) = 222(3)\,\text{mG}$ at zero temperature. Similar to the discussion of temperature dependence on the ^{6}Li p-wave Feshbach resonance, we discuss the shift in terms of temperature-induced resonance shifts for two- or three-body loss processes. The temperature dependent shift for two-body loss events is given by $3/2k_BT/\delta\mu = 10\,\text{mG}\,\mu\text{K}^{-1}$ [Chevy et al., 2005] and by $k_BT/\delta\mu = 7\,\text{mG}\,\mu\text{K}^{-1}$ for three-body loss [Gerken et al., 2019], where $\delta\mu = h\times 3\,\text{kHz}\,\text{mG}^{-1}$ is the differential magnetic moment between the bound molecular and free atom state. Only a small part of the resonance shift can be explained by these effects. The other $\sim 20\,\text{mG}\,\mu\text{K}^{-1}$ might be induced by the AC stark effect induced by the change in trap power for varying trap-depth and temperature [Jag et al., 2014; Cetina et al., 2016].

Figure 5.5b also shows the change of the resonance width w_0^e in dependence of the

temperature for the Cesium measurements. Here a linear fit gives the zero temperature width of $w_0^e(T=0) = 10(2)\,\mathrm{mG}$ with a slope of $32(4)\,\mathrm{mG\,\mu K^{-1}}$. For a full understanding of the width behavior, measurements over a larger range are necessary. At temperatures of 840 nK the resonance shape becomes asymmetric, which indicates a resonance width on the order of $\Gamma_r\hbar \approx k_B \times 840\,\mathrm{nK}$. Further reasons for the change in loss width can be experimental parameters like the trap-induced density inhomogeneity, magnetic field noise, and the holding time in the trap.

In conclusion we showed spin-spin splitting on five ^{6}Li-^{133}Cs p-wave Feshbach resonances via high-resolution trap-loss spectroscopy. We observed splittings between 75(12) mG and 422(5) mG that are in good agreement with a full coupled channel calculation. Temperature dependence on the resonance at 663 mG was investigated where no significant temperature dependence on the splitting could be observed. In the next chapter we discuss the lifting of the degeneracy in the $B^e_{|m_l|=1}$ states.

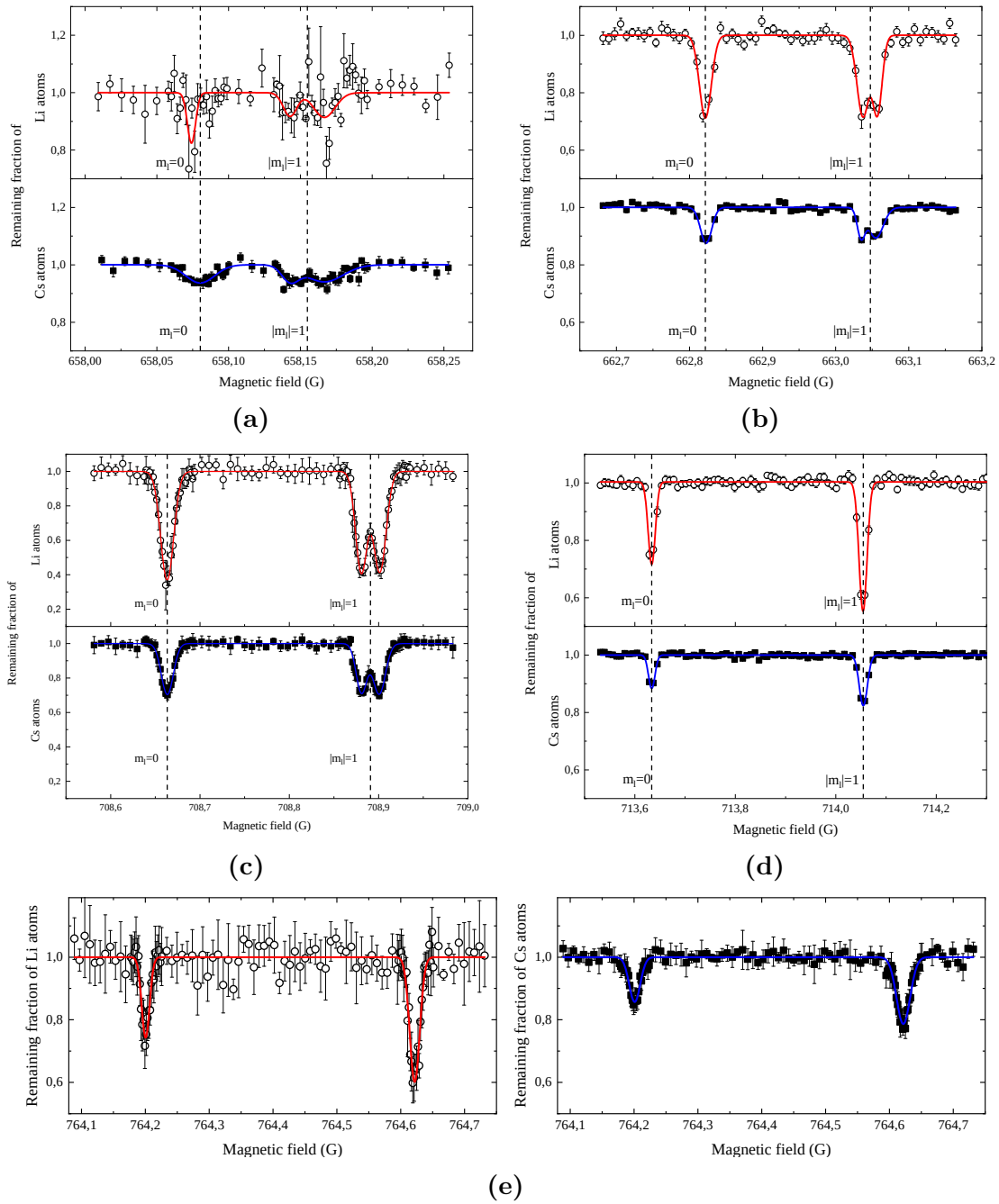

Figure 5.4: ^{6}Li-^{133}Cs p-wave Feshbach resonances in the $|\alpha\rangle$ (b) 663 G, d) 713 G resonances) and $|\beta\rangle$ (a) 658 G, c) 708 G and e) 764 G resonances) spin state channels. The upper graphs show the remaining fraction of ^{6}Li atoms (open circles). The lower graphs show the remaining fraction of ^{133}Cs atoms (solid square). The holding times are a) 10 s, b) 0.5 s, c) 1 s, d) 5 s and e) 5 s. The error bars are standard deviations with 10 repeated measurements at each point. Measurements are taken in random magnetic field order to reduce systematic field shifts. The solid lines are multi-peak Gaussian functions to extract resonance positions $B^e_{m_l}$ and resonance width $w^e_{m_l}$ presented in table 5.2. Dashed vertical lines indicate $m_l = 0$ to $|m_l| = 1$ dipole-dipole splitting. The doublet structure in the $|m_l| = 1$ resonances at a) 658 G, b) 663 G and c) 708 G is induced by spin-rotation coupling discussed in chapter 6.

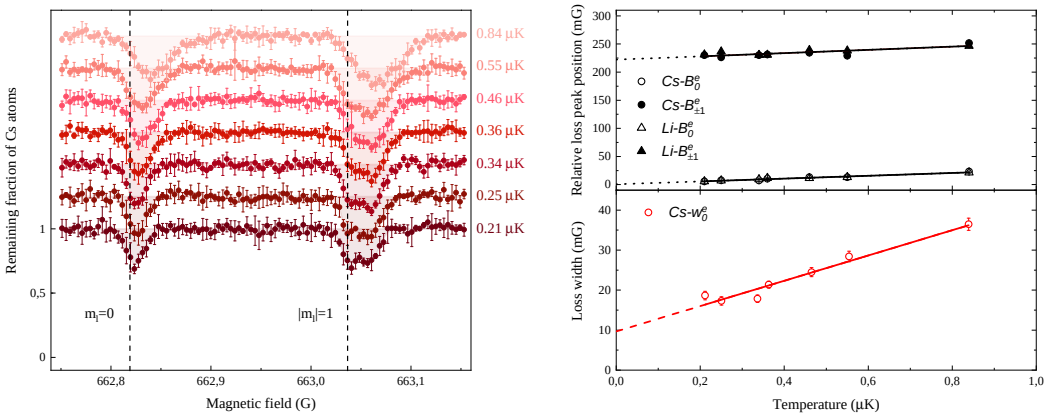

(a) **(b)**

Figure 5.5: Temperature dependence of the ^{6}Li-^{133}Cs p-wave Feshbach resonance near 663 G. a) Loss features for varied temperature by change of trap-depth. The remaining fraction of ^{133}Cs atoms after 0.2 s is shown as a function of the external magnetic field. The spectra are shifted vertically to avoid overlap. Each point is averaged over 4 experimental runs and the error bars show the standard deviation. A triplet Gaussian function is fitted to the data to extract the resonance position $B^e_{|m_l|}$. Vertical dashed lines indicate the zero temperature limit of the $B^e_{|m_l|=0}$ and $B^e_{|m_l|=1}$ resonance. b) shows the resonance positions $B^e_{|m_l|=0}$ ($B^e_{|m_l|=1}$) for ^{133}Cs and ^{6}Li as open circles and triangles respectively (for ^{133}Cs and ^{6}Li as solid circles and triangles respectively) and the resonance width w^e_0 for ^{133}Cs in red open circles. In the upper graph the zero position is set in reference to $B^e_{|m_l|=0}$ at zero temperature, $B^e_0(T = 0) = 662.819(3)$ G. The δ^e_{ss} dipole-dipole splitting does not depend significantly on the temperature within the observed range and is $\delta^e_{ss}(T = 0) = 222(3)$ mG.

6. Spin-Rotation interactions

In the previous section we discussed spin-spin coupling where the dipole-dipole interaction lead to different energy shifts depending on the orientation of the molecular rotation towards the magnetic field. These interactions lift the degeneracy of the $m_l = 0$ and $|m_l| = 1$ states in p-wave molecules. In this section we introduce spin-rotation coupling, the quantum-mechanical coupling of a spin to a magnetic field, induced by a physical rotation. Even though the effect is well known in molecular [Lefebvre-Brion H., 1986] and solid physics [Maekawa et al., 2012] it has not been observed so far in Feshbach molecules. In non-singlet molecules the spin-rotation coupling was first introduced by Friedrich Hund in 1927 [Hund, 1927]. The splitting is caused by the interaction of the electron's magnetic moment with the magnetic field induced by the rotation of the nuclear charges and the distorted electronic orbitals induced by the same rotation of the nuclear charges. We introduce the spin-rotation interaction Hamiltonian H_{sr} and add it to the total Hamiltonian H introduced in chapter 4.

$$H_{sr} = \frac{\gamma}{2\mu R^2}\vec{S}\vec{l} \tag{6.1}$$

where $\vec{S} = \sum_{\beta=A,B} \vec{s_\beta}$ is the total electron spin and $\vec{l}$ is the molecular rotation angular momentum. γ is the dimensionless spin-rotation coupling constant. Figure 6.1 shows a schematic on how the molecular rotation leads to the different couplings.

In deeply bound molecules the well known effect can be precisely measured via microwave spectroscopy [Brown and Alan, 2003]. However, in shallow molecular states, the weak rotational effects make it rarely accessible. The already weak dipole-dipole coupling effect can be compared to the spin-rotation coupling in relative strength to estimate the spin-rotation coupling effect. To do that we compare the magnetic fields involved in the two coupling cases. The first order effect of the spin-spin effect directly involves the electron's magnetic moment. The first order spin-rotation interaction involves a magnetic dipole moment induced by the rotation of the nuclei. Thus the ratio between the effects is proportional to the ratio of the electron-proton mass ratio $\sim m_e/m_p \approx 5 \times 10^{-4}$. The second order effects of the spin-rotation coupling are the perturbations of the nuclear rotation and the spin-orbit. The second order effect of the dipole-dipole coupling also arises from spin-orbit coupling. The relative coupling strength ratio can be estimated as B_v/A_{so}. Here B_v is the molecular rotational energy $B_v = \hbar^2/(2\mu R^2)$ with μ the reduced mass and A_{so} is the excited-state spin-orbit coupling constant [Strandberg and Tinkham,

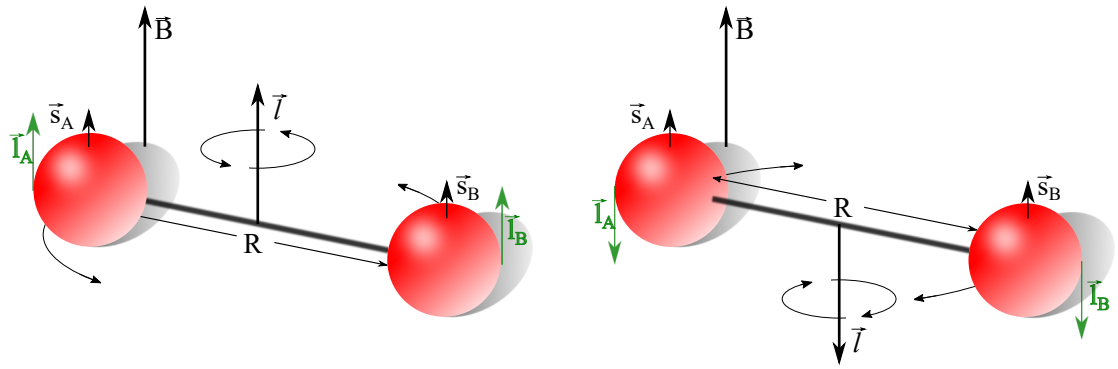

(a) $m_l = 0$ **(b)** $m_l = \pm 1$

Figure 6.1: Schematics of the spin-rotation coupling in a weakly bound dimer AB consisting of one-electron atoms A and B separated by a distance R rotating with nuclear angular momentum $\vec{l}$ in an external magnetic field $\vec{B}$. The electron spins are denoted by $\vec{s}_i$ with $i = A, B$. Spin-spin interaction would result in degenerate energies for the projections $m_l = \pm 1$ in (a) and (b), respectively. Nuclear rotation lifts this degeneracy by two effects: (1) Magnetic fields created directly by the rotating charges, and (2) spin-orbit coupling caused by rotation-induced electron orbital angular momenta $\vec{l}_A$ and $\vec{l}_B$. The corresponding energies in (a) and (b) have the same strength, but opposite sign.

1955]. Due to the large size of the Feshbach molecule the rotational energy takes small values of $B_v \approx h100\,\mathrm{MHz}$. The excited-state spin-orbit coupling can safely be assumed to be the ^{133}Cs $6p$ dominated spin-orbit coupling. This leads to a relative strength of $B_v/A_{so} \approx 10^{-5}$. Here the first order contribution dominates over the second order contribution. From the previous section, where we saw that the spin-spin splitting of a ^{6}Li-^{133}Cs p-wave Feshbach molecule was on the order of $\sim 400\,\mathrm{mG}$, we can safely assume, that the spin-rotation splitting is far below the accessible magnetic field resolution or washed out by the resonance width.

In this section we present the first experimental observation of spin-rotation splitting in high-resolution trap-loss spectroscopy in p-wave Feshbach resonances of ultracold gases, specifically in ultracold ^{6}Li-^{133}Cs. The spin-rotation interaction manifests itself as an additional splitting in the $m_l = \pm 1$ components of the loss spectra. We will start by presenting the experimental observations and discuss the relation to spin-rotation coupling in section 6.1. We also analyze the temperature dependence of the splitting. Finally we present a simple model-wave-function to calculate the first- and second order spin-rotation coupling components to gain a deeper understanding of the un-intuitive appearance of the effect.

6.1 Spin-rotation interactions in ^{6}Li-^{133}Cs

The data and the experimental procedure have been presented in the previous section 5.2. Figure 6.2 shows a zoom on the atom loss spectroscopy data of the ^{6}Li-^{133}Cs p-wave Feshbach resonance at 658 G, 663 G and 708 G presented in figure 5.4 to highlight the spin-rotation splitting. We fit multi Gaussian functions to the loss spectra and extract loss position $B^e_{m_l}$, loss width $w^e_{m_l}$ and spin-rotation splitting $\delta^e_{sr} = B^e_{-1} - B^e_{+1}$ from the data and summarize them in table 6.1. The two remaining resonances at 714 G and at 764 G do not show a splitting of the $m_l = \pm 1$ states. The observed splittings are on the order of 20 mG, much larger then what we expect from the initial estimation.

To account for the observed splitting, the spin-rotation interaction Hamiltonian from equation 6.1 is included in the full coupled channel calculation. We fit the splittings with γ, the dimensionless spin-rotation parameter, as the only free parameter. In the range of high magnetic fields, l and m_l both are nearly conserved parameters, such that only the diagonal terms of the Hamiltonian H_{sr} contribute significantly to the energy splitting. The diagonal term $\gamma \frac{\hbar^2}{2\mu R^2} S_z m_l$ then leads to the splitting

$$\Delta E_{sr} = 2\gamma B_v \langle S_z \rangle \tag{6.2}$$

between the $m_l = +1$ and $m_l = -1$ components. Here S_z is the projection of the total spin $\vec{S}$ along the external magnetic field, $\langle S_z \rangle$ the expectation value in the closed channel and $B_v = \langle \hbar^2/(2\mu R^2) \rangle \sim 228$ MHz is the rotational constant of the least bound vibrational state of the ^{6}Li-^{133}Cs triplet electronic ground state. Table 6.1 also shows the spin-rotation parameter γ^e we measure for each splitting calculated using

$$\gamma^e = -\mu_{rel} \frac{\delta^e_{sr}}{2\langle S_z \rangle B_v} \tag{6.3}$$

The values $\langle S_z \rangle$ and μ_{rel} are calculated via a full coupled channel calculation without the spin-spin and spin-rotation terms. We fit the observed splittings including H_{sr} to the full coupled channel calculation and determine the free fit parameter $|\gamma^{cc}| = 0.566(50) \times 10^{-3}$. We cannot determine the sign of γ^{cc} since a sign change of γ^{cc} and m_l are interchangeable. We assign the quantum numbers m_l to the loss resonances in figure 6.2 according to a positive γ^{cc}. The table also shows the spin-rotation splittings δ^t_{sr} calculated for each resonance via the full coupled channel calculation using γ^{cc}. The experimentally observed splittings of the three resonances are in very good agreement with the theoretical values. For the two resonances where no splitting is observed, the predicted splitting is small compared to the measured loss width w^e_0. We assume, that the splittings cannot be observed due to limiting resolution under the current experimental conditions. The differences in the predicted splittings δ^t_{sr} for the different resonances arises from different singlet- triplet character of the closed molecular states $\langle S_z \rangle$.

The spin-rotation coupling explains very well the observed splittings and also the non-observed splittings. To further justify the spin-rotation coupling as the observed effect, we investigate further possible explanations [Tischer, 1967]. The rotational Zeeman effect

Table 6.1: Spin-rotation splitting in ^{6}Li-^{133}Cs p-wave Feshbach resonances observed for different spin channels $|\alpha\rangle = {}^6\text{Li}|1/2,+1/2> \oplus {}^{133}\text{Cs}|3,+3>$ and $|\beta\rangle = {}^6\text{Li}|1/2,-1/2> \oplus {}^{133}\text{Cs}|3,+3>$. The resonances are observed at the magnetic field $B^e_{\pm1}$ and the corresponding loss width $w^e_{\pm1}$. δ^e_{sr} is the splitting observed corresponding to the spin-rotation interaction. The numbers in parentheses give the uncertainties in the determination of $B^e_{\pm1}$, $w^e_{\pm1}$ and δ^e_{sr}. The systematic uncertainty is shown for $B^e_{\pm1}$ in the second bracket. δ^t_{sr} shows the corresponding theoretical value obtained from the full coupled-channel calculations for a relative kinetic energy corresponding to the temperature 430 nK, the temperature at the experiment. The remaining two resonances presented in table 5.2 do not show a splitting of the $m_l = \pm1$ states.

	$B^e_{\pm1}(G)$	$w^e_{+1/-1}(mG)$	$\delta^e_{sr}(mG)$	$\delta^t_{sr}(mG)$	$\gamma^e(10^{-3})$
$\|\alpha\rangle$	662.929(3)(16)	6(1)/10(1)	20(6)	17	0.6(2)
$\|\beta\rangle$	658.155(10)(16)	6(1)/13(1)	24(14)	25	0.5(3)
	708.772(3)(16)	6(1)/7(1)	20(4)	17	0.6(1)

splits the m_l states, but only shows a small dependence on $\langle S_z\rangle$ due to the small coupling to the rotation. This is contradictory to our observation showing a strong dependence on the electron spin, indicating that the rotational Zeeman effect is not responsible for the splitting. The molecular anisotropy of the electron g-tensor with respect to the molecular axis results from the spin-orbit interaction and could thus yield a small contribution compared to the spin-rotation interaction. Including this effect into the fitting routine results in a magnitude of about 10 % of the free electron's g factor. This unphysically large contribution indicates, that also the molecular anisotropy of the electron g-tensor is not responsible for the observed splitting. We conclude, that spin-rotation coupling plays the dominant role in the observed splittings.

We also investigate the behavior of the temperature on the spin-rotation splitting. In figure 6.3 we present the temperature dependent high-resolution trap-loss spectra with a focus on the $m_l = \pm1$ loss peaks. Figure 6.3b shows the change of the loss peak positions B^e_{+1} and B^e_{-1} relative to the $B^e_{|m_l|=\pm1}$ at zero temperature, $B^e_0(T=0) = 663.051(3)$ G. The splitting at zero temperature is $\delta^e_{sr}(T=0) = 20(6)$ mG. The slope are $20(10)\,\text{mG}\,\mu\text{K}^{-1}$ and $24(10)\,\text{mG}\,\mu\text{K}^{-1}$ for the B^e_{+1} and B^e_{-1} states respectively. This shows, that the spin-rotation splitting does not depend significantly on the temperature within the observed range. The slopes themselves follow the observed slopes for the B^e_0 state discussed in section 5.2 and can thus be explained with the same arguments.

In conclusion we presented an experimental observations of a triplet structure of ^{6}Li-^{133}Cs p-wave Feshbach resonances via high-precision trap-loss spectroscopy. We attributed the splittings to spin-spin and spin-rotation interactions and assigned m_l quantum numbers to the loss peaks. We fitted a full coupled channel calculation to the spectra and extracted the dimensionless spin-rotation parameter $\gamma^{cc} = 0.566(50) \times 10^{-3}$. In the next

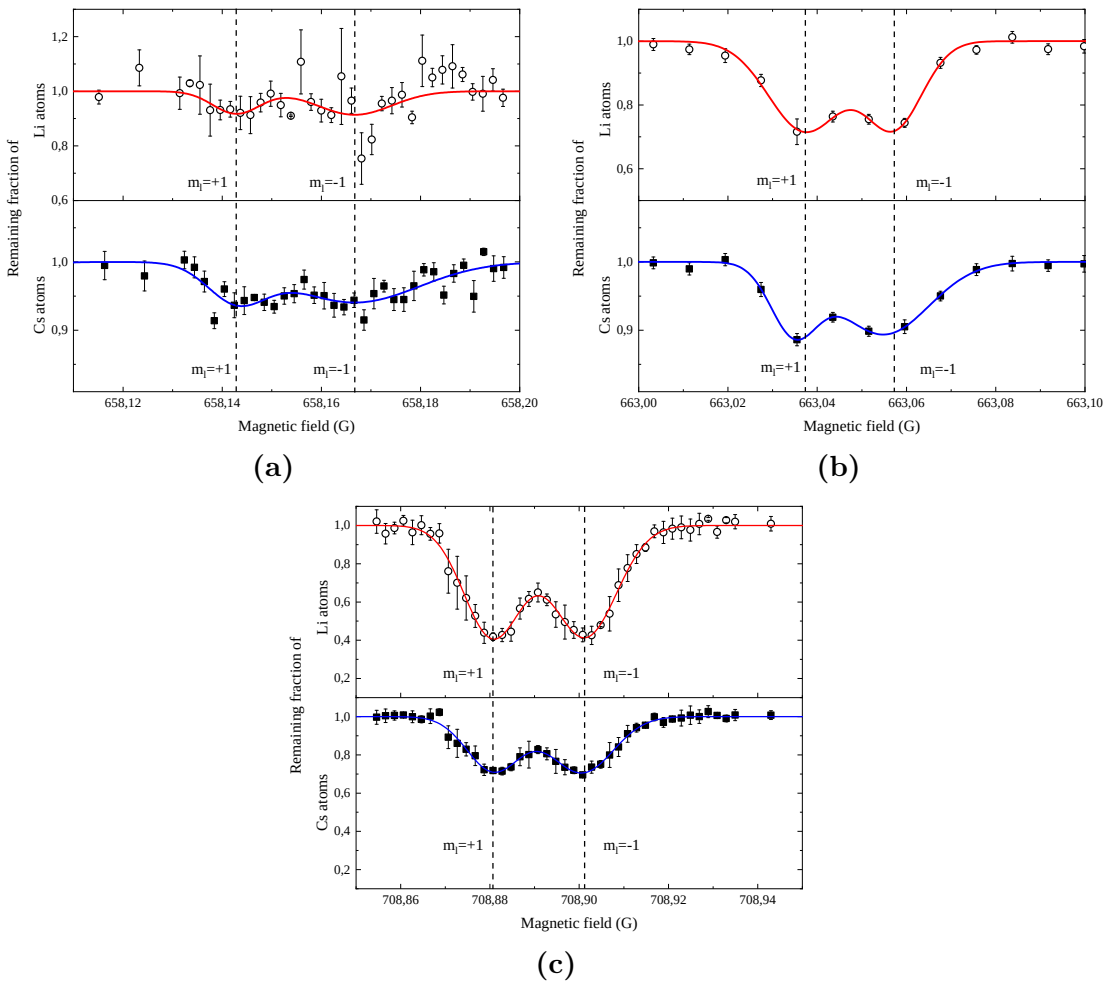

Figure 6.2: ^{6}Li-^{133}Cs p-wave Feshbach resonances in the $|\alpha\rangle$ spin state channel a) 663 G and $|\beta\rangle$ spin state channels b) 658 G, c) 708 G. The upper graphs show the remaining fraction of ^{6}Li atoms (open circles). The lower graphs show the remaining fraction of ^{133}Cs atoms (solid square). The holding times are a) 10 s, b) 0.5 s, c) 1 s. The error bars are standard deviations with 10 repeated measurements at each point. Measurements are taken in random magnetic field order to reduce systematic field shifts. The solid lines are multi-peak Gaussian functions to extract resonance positions $B^{e}_{m_l}$ and resonance width $w^{e}_{m_l}$ presented in table 6.1. Dashed vertical lines indicate $m_l = +1$ to $m_l = -1$ spin-rotation splitting. The doublet structure is induced by spin-rotation coupling.

section we will present a simple model to calculate the spin-spin parameter λ introduced in section 5.2 and the spin-rotation parameter γ from a model wavefunction for the case of ^{6}Li-^{133}Cs.

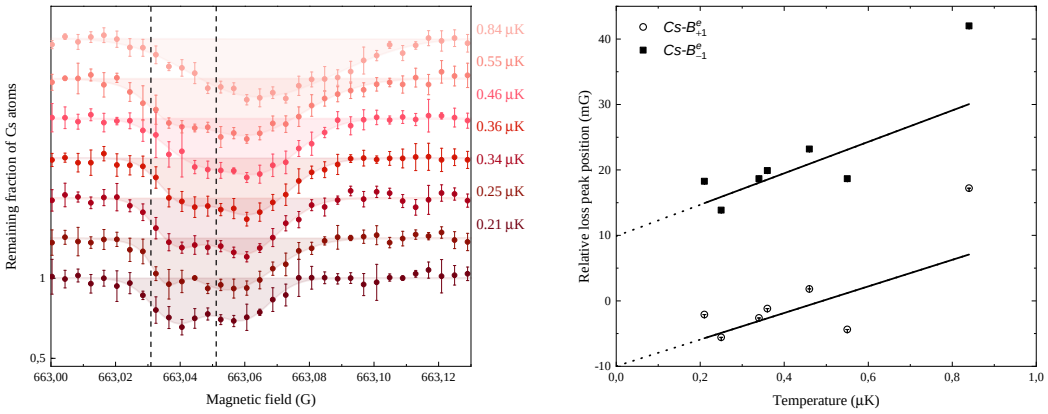

(a) **(b)**

Figure 6.3: Temperature dependence of the ^{6}Li-^{133}Cs p-wave Feshbach resonance near 663 G. a) Loss features for varied temperature by change of trap-depth. The remaining fraction of ^{133}Cs atoms after 0.2 s is shown as a function of the external magnetic field. The spectra are shifted vertically to avoid overlap. Each point is averaged over 4 experimental runs and the error bars show the standard deviation. A triplet Gaussian function is fitted to the data to extract the resonance position $B^e_{|m_l|}$. Vertical dashed lines indicate the zero temperature limit of the B^e_{+1} and B^e_{-1} resonance. m_l values are indicated according to a positive γ^{cc}. b) shows the resonance positions B^e_{-1} (B^e_{-1}) for ^{133}Cs as open circles and closed squares respectively. The zero position is set in reference to $B^e_{|m_l|=\pm1}$ at zero temperature, $B^e_0(T=0) = 663.051(3)$ G. The δ^e_{sr} dipole-dipole splitting does not depend significantly on the temperature within the observed range and is $\delta^e_{sr}(T=0) = 20(6)$ mG.

6.2 Modeling the ^{6}Li-^{133}Cs Spin-Rotation Interactions

In this section we want to introduce a simple model for the calculation of the spin-spin and spin-rotation interactions in a ^{6}Li-^{133}Cs system to gain a deeper physical understanding of the important constituents of the effects. The ratio of the observed values γ/λ is larger then expected. We will try to reproduce our fitted values for the dimensionless spin-spin and spin-rotation parameters λ and γ. To do this we will calculate the first- and second order contributions of both parameter using a molecular wavefunction constructed out of the atomic electron wavefunctions. We obtained it from the atomic electron wavefunctions at the unperturbed ground states by treating the static Coulomb interactions between atom pairs separated by a distance R. Figure 6.4 shows a schematic for the relevant values of the model. We start this section by introducing the model wavefunction, being the nuclear- and the electronic wavefunctions. Afterwards we will use the model wavefunction to first calculate the first- and second order contribution for the spin-spin parameter, and later for the spin-rotation parameter.

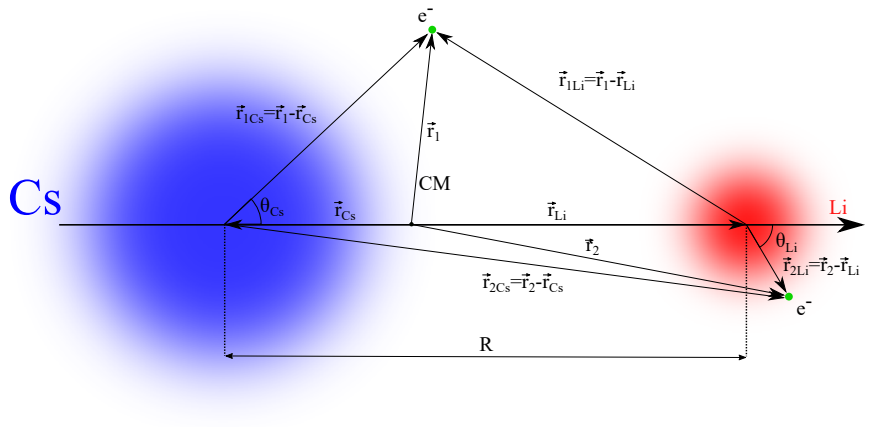

Figure 6.4: Schematic drawing of a ^{6}Li-^{133}Cs dimer with center of mass (CM) coordinate system and z axis along the internuclear axis. The variable $\beta = Li, Cs$ indicates the cores and $i = 1, 2$ indicates the electrons. The ionic cores coordinate is described as $\vec{r} = (0, 0, z_\beta)$, the valence electrons are found at $\vec{r}_i = (x_i, y_i, z_i)$. $\vec{r}_{i\beta} = \vec{r}_i - \vec{r}_\beta$ describes the vector from the core β to the valence electron i and the angle θ_β is defined as the angle from the z axis to the corresponding valence electron.

The nuclear wavefunction is obtained by solving the Schrödinger equation for the last vibrational state of the ^{6}Li-^{133}Cs triplet ground state potential $a^3\Sigma^+$. The bound state problem is solved by the so-called renormalized Numerov method [Johnson, 1977]. The potential we use is obtained via the full coupled channel calculations using all ^{6}Li-^{133}Cs resonance position [Häfner, 2017]. The potential also includes the centrifugal barrier $l(l+1)\hbar^2/(2\mu R^2)$ for p-wave potentials. Figure 6.5a shows a schematic of the obtained nuclear wave function in the nuclear potential. Note, that the centrifugal barrier is far to small to be seen ($10^{-6} E_\mathrm{h}$). The binding energy is 3376 MHz, the inner turning point R_{in} is at about $8\,a_0$ and the outer turning point R_{out} is at about $43\,a_0$.

The electron wavefunction and energy for the atom pair at large R, are obtained following a perturbative derivation of the dispersion coefficients for the ground-state potentials of bi alkali atoms presented in Marinescu and Dalgarno [1995]. This approximation is valid for nuclear distances down to the LeRoy radius R_{LR} [Le Roy, 1974] where the electron wavefunctions of the separated atoms do not overlap. In the case of ^{6}Li-^{133}Cs ground state wavefunctions the LeRoy radius is $R_{LR} \approx 20\,a_0$. In zeroth order we assume both atoms to be in their electronic ground state being $\left|\psi_{2s}^{Li}\right\rangle$ and $\left|\psi_{6s}^{Cs}\right\rangle$ which we write short as $\left|\Psi_{2s,6s}\right\rangle$ for simplification. As the first-order correction we add components of the electronic wave function being in the first excited state $\left|\Psi_{2p,6p}\right\rangle$. The full electronic

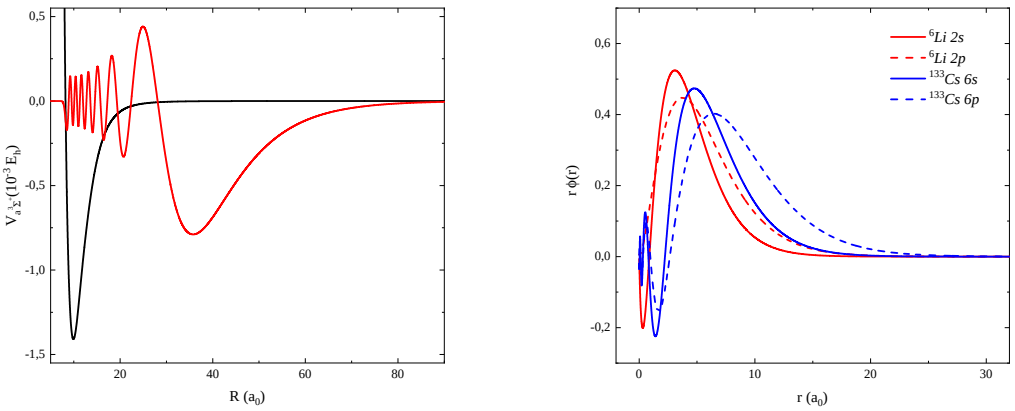

(a) **(b)**

Figure 6.5: Model wavefunctions for the calculation of the spin-spin parameter λ and the spin-rotation parameter γ. a) shows the triplet groundstate $a^3\Sigma^+$ potential including the p-wave centrifugal barrier in black [Zhu et al., 2021a]. The nuclear wavefunction $\Psi(R)$ of the least bound vibrational state is shown in red. The energy scale of the potential is given in E_h the Hartree energy, while the amplitude of the wavefunction is arbitrarily choose for visualization. b) shows the electronic wavefunctions for ^{6}Li (^{133}Cs) in red (blue) with the ground state $2s$ ($6s$) and the excited state $2p$ ($6p$) are shown as solid and dashed lines respectively. Here r is the distance between the atomic nucleus and its valence electron.

wavefunction can then be written as

$$|\Psi; R\rangle = |\Psi_{2s,6s}\rangle + \sum_{m=-1,0,1} c_{1,m} \left|\psi^{Li}_{2p,m_l}\right\rangle \left|\psi^{Cs}_{6p,-m_l}\right\rangle \tag{6.4}$$

where m_l denotes the projection of the electronic orbital momentum. The coefficients $c_{1,m}$ are given by

$$c_{1,0} = 2c_{1,\pm1} = -\frac{2c}{3R^3}(E_{Li,2p} + E_{Cs,6p})^{-1} \tag{6.5}$$

where $c = \left\langle \psi^{Li}_{2p} \right| r \left| \psi^{Li}_{2s} \right\rangle \left\langle \psi^{Cs}_{6p} \right| r \left| \psi^{Cs}_{62s} \right\rangle \approx 24.1$. The second order corrections to the electronic wavefunction can be neglected since they are smaller by a factor of 10^4 compared to the first order correction. Thus we now have a full molecular wavefunction validly approximated for internuclear distances of $R > R_{LR}$.

6.2.1 Modeling Spin-Spin Coupling

In this section we calculate the expected spin-spin coupling parameter λ via the fit parameters obtained from the full coupled channel calculation. Following Strandberg and Tinkham [1955]; Brown and Alan [2003] we separate λ into two parts, namely the first-order magnetic dipole-dipole interaction and the second order spin-orbit coupling.

The first order contribution models the magnetic dipole-dipole interaction. It's $1/R^3$ dependence is well known for dipole-dipole interactions. In the spin-spin coupling parameter $\lambda^{(1)}$ as used [Stoof et al., 1988; Moerdijk et al., 1995] in equation 5.2 is manifested in

$$\lambda^{(1)} = -\frac{3}{4}\frac{\alpha^2}{R^3} \tag{6.6}$$

The second order contribution models the coupling of the electron spin to the electron orbital deformed by the molecular rotation. In the spin-spin coupling parameter $\lambda^{(2)}$ as used [Mies et al., 1996; Kotochigova et al., 2001] in equation 5.2 is manifested in

$$\lambda^{(2)} = -\frac{3}{4}\alpha^2 \left(a_{so1}\exp\left(-b_1 R\right) + a_{so2}\exp\left(-b_2 R\right)\right) \tag{6.7}$$

as a biexponential R-function.

Both $\lambda^{(i)}$ for $i = 1, 2$ are plotted in figure 6.6. $\lambda^{(2)}$ is shown with inverse sign. This already shows, that both orders are competing. While $\lambda^{(1)}$ is dominating at long range, $\lambda^{(2)}$ dominates at short range. The lower part of figure 6.6 shows both $\lambda^{(i)}$ components weighted by our model molecular wavefunction. To obtain the averaged $\langle\lambda(R)\rangle$ as measured and presented in table 5.2, we average and add both λ components $\langle\lambda(R)\rangle = \langle\lambda^{(1)}(R)\rangle + \langle\lambda^{(2)}(R)\rangle$ over R.

We obtain $\langle\lambda(R)\rangle/B_v \approx -8 \times 10^{-3}$. This is in very good agreement with our experimental observations presented in table 5.2.

6.2.2 Modeling Spin-Rotation Coupling

Also here we will follow closely the derivation presented in Brown and Alan [2003]; Strandberg and Tinkham [1955] where the spin-rotation coupling for the $X^3\Sigma_g^-$ state of O_2 are evaluated.

The first order contribution of the spin-rotation coupling describes the coupling for the electric spins to the magnetic field induced by the molecular rotation. Van Vleck [1951] gives the first order contribution in the form

$$H_{sr}^{(1)} = \frac{1}{2}g\alpha^2\left(\sum_{\beta,i}\frac{Z_{i\beta}(\vec{v}_\beta \times \vec{r}_{i\beta})}{r_{i\beta}^3}\cdot\vec{s}_i - \sum_{i\neq j}\frac{\vec{v}_j \times \vec{r}_{ji}}{r_{ji}^3}\cdot\vec{s}_j\right) \tag{6.8}$$

Here g is the g-factor of the electron, α is the fine structure constant. The subscripts $i = 1, 2$ and $\beta = \mathrm{Li}, \mathrm{Cs}$ denote the two valence electrons and the atomic cores, respectively. $Z_{i\beta}$ is the effective nuclear charge of β seen by the electron i at $\vec{r}_{i\alpha} = \vec{r}_i - \vec{r}_\alpha$ and $\vec{r}_{ji} = \vec{r}_j - \vec{r}_i$. Here $\alpha$is the index of the nuclei. The effective charges of the atomic cores are seen shielded by the valence electrons. Including the shielding of the nuclear charge by the inner electrons, we take $Z_{2Li} = 1.3$, $Z_{1Cs} = 6.4$ and $Z_{1Li} = Z_{2Cs} = 1$ [Clementi and Raimondi, 1963; Clementi et al., 1967]. $\vec{v}_i$ describes the electronic velocities. Due to the

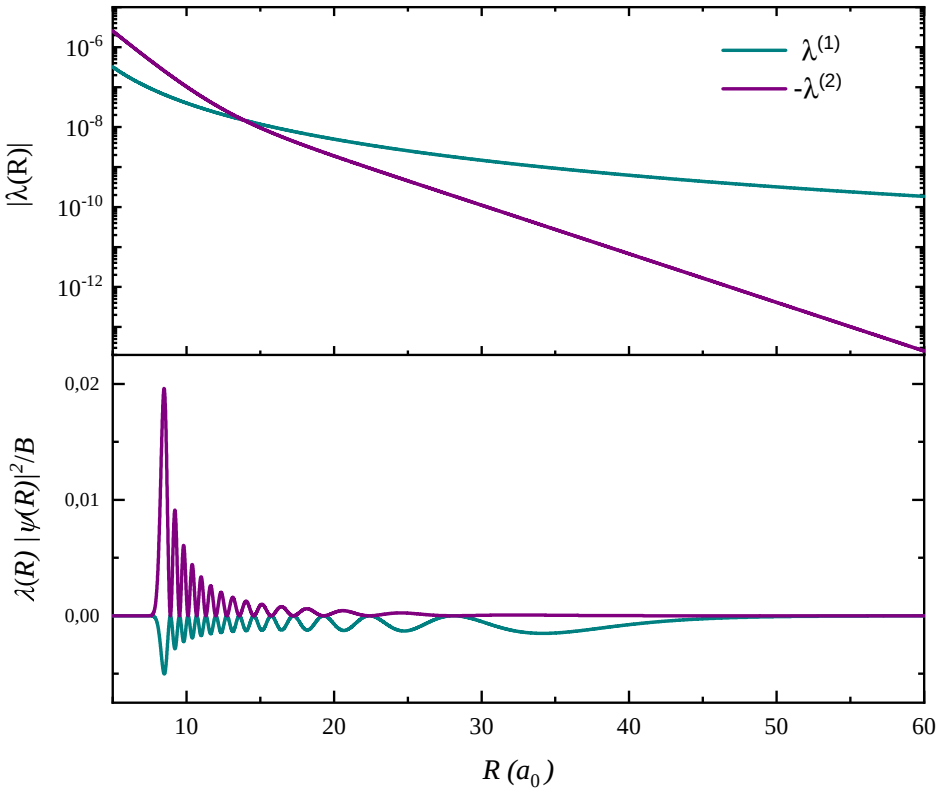

Figure 6.6: First-order (dark cyan) and second order (purple) spin-spin coupling parameter λ from equation 6.6 and 6.7 respectively. The lower graph shows their corresponding values weighted by the absolute square of the nuclear wavefunction $|\Phi(R)|^2$. To obtain the values for $\lambda^{(1)}$ and $\lambda^{(2)}$ we integrate over R.

fast oscillatory nature of their motions, their contributions average to zero. The second term of equation 6.8 is zero. $\vec{v}_\beta$ describes the nuclear velocities that can be replaced by the molecular rotation giving $\vec{v}_\beta = \frac{l}{\mu R^2} \times \vec{r}_\beta$. With this we rewrite equation 6.8 as

$$H_{sr}^{(1)} = \frac{g\alpha^2}{2\mu R^2} \sum_{\beta,i} \frac{Z_{i\beta}(\vec{l} \cdot \vec{r}_{i\beta})\vec{r}_\beta - (\vec{r}_\beta \cdot \vec{r}_{i\beta})\vec{l}}{r_{i\beta}^3} \cdot \vec{s}_i \tag{6.9}$$

Due to the axial symmetry around the internuclear axis z in the molecule, any terms containing odd powers of x_i and y_i are zero and we can further simplify to

$$H_{sr}^{(1)} = -g\alpha^2 B(R)\vec{l} \cdot \sum_{\beta,i} Z_{i\beta} \frac{z_\beta(z_i - z_\beta)}{r_{i\beta}^3} \vec{s}_i \tag{6.10}$$

which results in the first order contribution of the spin-rotation parameter γ

$$\gamma^{(1)} = -g\alpha^2 B(R) \langle \Phi; R| \sum_{i,\beta} \frac{\vec{S}\cdot\vec{s}_i}{S(S+1)} Z_{i\beta} \frac{z_\beta(z_i - z_\beta)}{r_{i\beta}^3} |\Phi; R\rangle \approx \frac{g\alpha^2}{2} R^{-1} = 5.4 \times 10^{-5} R^{-1} \tag{6.11}$$

The final step of this calculation is presented in the appendix A.2. Due to the large interactomic separation, the contribution of the excited state $\left|\Phi_{2p,6p}\right\rangle$ to the first-order spin-rotation energy is negligible within the approximations made.

The second order contribution to the spin-rotation energy arises from the finite electronic orbital angular momentum induced by the rotation of the nuclei. This then undergoes spin-orbit coupling involving the electronically excited states admixed to the groundstate. In this sense the second order contribution is a second order spin-orbit coupling effect. The resulting perturbation to the groundstate energy thus can be written as [Brown and Alan, 2003; Strandberg and Tinkham, 1955]

$$H_{sr}^{(2)}(R) = \sum \frac{\langle \psi; R| H_{so}^e \left|\Psi_{2p,6p}\right\rangle \left\langle \psi_{2p,6p}\right| 2B(R)\vec{L}\cdot\vec{l} |\Psi; R\rangle}{E_{Li,2p} + E_{Cs,6p}} \tag{6.12}$$

Here the excited molecular state is approximated with the atomic excited state $\left|\Phi_{2p,6p}\right\rangle$. The sum is taken over all substates, meaning m_l configurations. The energies $E_{Li,2p}$ and $E_{Cs,6p}$ are the energies of the bare atomic states in the ^{6}Li $2p$ and ^{133}Cs $6p$ states in reference to their atomic groundstate. The Hamiltonian $H_{so}^e = \sum_i A_i(R)\vec{\ell_i}\cdot\vec{s}_i$ with $\vec{\ell_i}$ and $\vec{s}_i$ being the orbital angular momentum and spin angular momentum of the atom i respectively, is the spin-orbit Hamiltonian. The total electronic orbital angular momentum is the sum of the individual ones $\vec{L} = \sum_i \vec{\ell_i}$.

Equation 6.12 can be rewritten in form of $\gamma_i^{(2)}$, the coupling constant for the individual electrons, by using the relations $\vec{\ell_i}\cdot\vec{s_i} = (\ell_i^+ s_i^- + \ell_i^- s_i^+)/2 + \ell_i^z s_i^z$ and $\vec{\ell_i^+}\vec{l} = (\ell_i^+ l^- + \ell_i^- l^+)/2 + \ell_i^z l^z$

$$\gamma_i^{(2)} = \frac{1}{2} \sum \frac{\langle \psi; R| A_i \ell_i^+ \left|\Psi_{2p,6p}\right\rangle \left\langle \psi_{2p,6p}\right| \ell_i^- |\Psi; R\rangle}{E_{Li,2p} + E_{Cs,6p}} \tag{6.13}$$

with $\sum \langle \psi; R| A_i \ell_i^+ \left|\Psi_{2p,6p}\right\rangle \left\langle \psi_{2p,6p}\right| \ell_i^- |\Psi; R\rangle = \frac{10c^2}{9R^6(E_{Li,2p}+E_{Cs,6p})^2}$ we can rewrite the second order spin-rotation parameter to the form

$$\gamma^{(2)}(R) = \frac{1}{2}\sum_i \gamma_i^{(2)}(R) = \frac{5c^2 \sum_i A_i}{18R^6(E_{Li,2p} + E_{Cs,6p})^2} \approx 232.6R^{-6} \tag{6.14}$$

We can already see, that $\gamma^{(1)}$ dominates the spin-rotation coupling at large internuclear distance R and $\gamma^{(2)}$ dominates at low distance. Figure 6.7 shows $\gamma^{(1)}$ and $\gamma^{(2)}$ over the internuclear distance R. The lower figure 6.7 shows the parameters weighted with the square of the nuclear wavefunction from figure 6.5a.

To obtain $\langle\gamma(R)\rangle = \langle\gamma^{(1)}(R)\rangle + \langle\gamma^{(2)}(R)\rangle$ we average the weighted components over

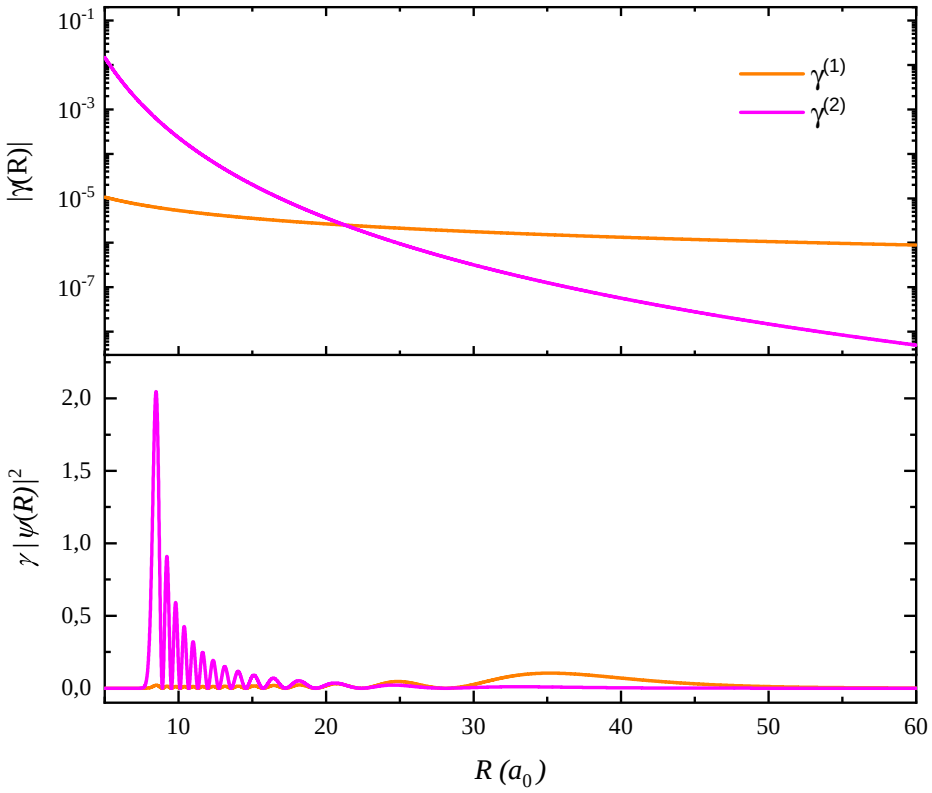

Figure 6.7: First-order (orange) and second order (magenta) spin-rotation coupling parameter γ from equation 6.11 and 6.14 respectively. The lower graph shows their corresponding values weighted by the absolute square of the nuclear wavefunction $|\Phi(R)|^2$. To obtain the values for $\gamma^{(1)}$ and $\gamma^{(2)}$ we integrate over R.

the nuclear distance R and add them. As a loose lower bound for the estimation we extend our estimations of the $\gamma^{(1)}$ and $\gamma^{(2)}$ components to $R < R_{LR}$, such that we average over the whole range of the internuclear distance $R_{in} < R < R_{out}$ as we did for the spin-spin coupling parameter λ. In our simple model we find $\langle\gamma^{(1)}(R)\rangle = 1.5 \times 10^{-6}$ and $\langle\gamma^{(2)}(R)\rangle = 2.4 \times 10^{-6}$. This is significantly (two orders of magnitude) smaller than our experimentally determined values of $\langle\gamma(R)\rangle \approx 5.5 \times 10^{-4}$ as presented in table 6.1. This is explained by the underestimation of both first- and second order effects in the range $R_{in} < R < R_{LR}$ where our electronic wavefunction is not valid. In reverse this means, that our high-precision measurement of the spin-rotation parameter γ is a precise measure for the short-range part of the electronic wavefunction in the molecular structure. Our measurements can be a benchmark for elaborated ab-initio calculations of the electronic structure of molecules at short range [Mies et al., 1996; Kotochigova et al., 2001].

7. Exploratory study of losses near a p-wave Feshbach Resonance

Understanding losses near magnetic Feshbach resonances has been essential for the exploitation of said resonances as a control tool in ultracold atom experiments. The mapping of a three-body loss minimum in ^{133}Cs , induced by a loss resonance interference, has been key for the preparation of the first ^{133}Cs BEC [Weber et al., 2003]. The stability of a degenerate Fermi sample, caused by the suppression of the possible loss processes [Petrov, 2003; Petrov et al., 2004], lead first to the production of a BEC of degenerate Fermi atom dimers [Jochim et al., 2003] and later to the investigation of the BEC-BCS crossover regime [Bourdel et al., 2004; Bartenstein et al., 2004; Partridge et al., 2005]. p-wave Feshbach resonances do not show the stability seen in Fermi gas s-wave resonances [Regal et al., 2003]. Great efforts have been made to understand the elastic [Regal et al., 2003; Chevy et al., 2005; Nakasuji et al., 2013] and inelastic scattering processes surrounding p-wave resonances. Inelastic loss processes of two-body nature, where the collision leads to a dipolar relaxation, are dominant in two component Fermi gases [Zhang et al., 2004; Waseem et al., 2017]. In a one component Fermi gas polarized in the lowest hyperfine ground state the two-body relaxation is suppressed due to energy and momentum conservation. Instead the inelastic three-body process dominates [Regal et al., 2003; Suno et al., 2003; Yoshida et al., 2018; Waseem et al., 2018]. In Waseem et al. [2019] a cascade model has been developed that separated the inelastic process into a two step. In the first step the dimer forms with a momentum dependent rate of Γ_r. In the second step a deeply bound dimer can be formed with help of an observer atom with ratio Λ_{ad}. The high momentum dependence on p-wave Feshbach resonances have lead to interesting studies surrounding the ratio of elastic to inelastic collision, also called good to bad collision ratio. Collisional cooling has been proposed and investigated where loss of high momentum particles through inelastic collisions, and momentum redistribution through elastic collisions leads to an increase of the phase space density of the probed gas [Mathey et al., 2009; Mathew and Tiesinga, 2013; Nuske et al., 2015; Horvath et al., 2017; Peng et al., 2021]. Top et al. [2021] used high densities to find a beneficial good to bad collision ratio for effective evaporative cooling far away from a p-wave Feshbach resonance. The separation of elastic and inelastic collisions across the momentum distribution lead to non equilibrium distributions. In this chapter we expand the cascade model of Waseem et al. [2019] and theoretically investigate implications. We find two regimes where either elastic collisions dominate over inelastic

collisions and the expected three-body loss behavior remains. In the second regime thermalization is slow compared to losses and the loss curve follows two-body loss behavior leading to out of equilibrium momentum distributions. In section 7.1 we introduce the model and fit it to the data of Waseem et al. [2019] in section 7.2. In section 7.3 and 7.4 we present the two regimes and present their different behaviors. We finally discuss the separations of regimes and accessibility in an experiment of ultracold ^{6}Li in section 7.5.

7.1 Cascade process

To understand the scattering processes close to a p-wave Feshbach resonance we describe the process as a cascade of several steps following [Li et al., 2018] and [Waseem et al., 2019]. Figure 7.1 shows two p-wave Van-der-Waals potentials as open- and closed channels. Two colliding atoms of energy E in the open channel tunnel through the centrifugal barrier at a rate $\Gamma_r(E)$ if on resonance with a dimer state of bound state energy E_r of the closed channel inducing the Feshbach resonance. The dimer can either decay through the barrier again with rate Γ_r and lead to two free atoms or collide with another free atom and form a deeply bound dimer via the rate coefficient of vibrational quenching Λ_{ad}. The first process describes an elastic scattering process. In the second process decay into a deeply bound molecular state will set free kinetic energy on the order of ΔE, the bound state energy of a deeply bound dimer. When the kinetic energy is large compared to the trap potential this process leads to loss from the trap. To model the loss as change of atomic density, we describe these three processes in a set of differential equations as done in Waseem et al. [2019]:

$$\frac{dn}{dt} = 2\Gamma_r n_D - 2L_m n^2 - \Lambda_{ad} n n_D \tag{7.1}$$

$$\frac{dn_D}{dt} = -\Gamma_r n_D + L_m n^2 - \Lambda_{ad} n n_D \tag{7.2}$$

where n is the atomic density and n_D is the dimer density. The first term in both equations describes the decay from dimer to two free atoms. The second term describes the creation of a dimer by two free atoms under the condition we will discuss further. The third term describes the loss of one free atom and a dimer. The rate Γ_r is given by the Wigner threshold law [Gurarie and Radzihovsky, 2007]

$$\Gamma_r(E) = \frac{2\sqrt{m}E^{3/2}}{k_e \hbar^2} \tag{7.3}$$

where m is the atomic mass, k_e the effective range and E is the collision energy. L_m is an energy independent atom-atom collision rate that can be written in a momentum dependent rate $K_m(v', v'')$ where $L_m n^2 = \int K_m(v', v'')\rho(v')\rho(v'')dv'dv''$ where $\rho(v)$ is the phase space distribution [1]. K_m is the atom to dimer creation rate and can contain different assumptions [Schmidt et al., 2020; Waseem et al., 2019]. In the case that $\Gamma_r \hbar \ll k_B T$,

[1] In the case of a thermal gas the phase space distribution $\rho(v)$ is given by the density n times

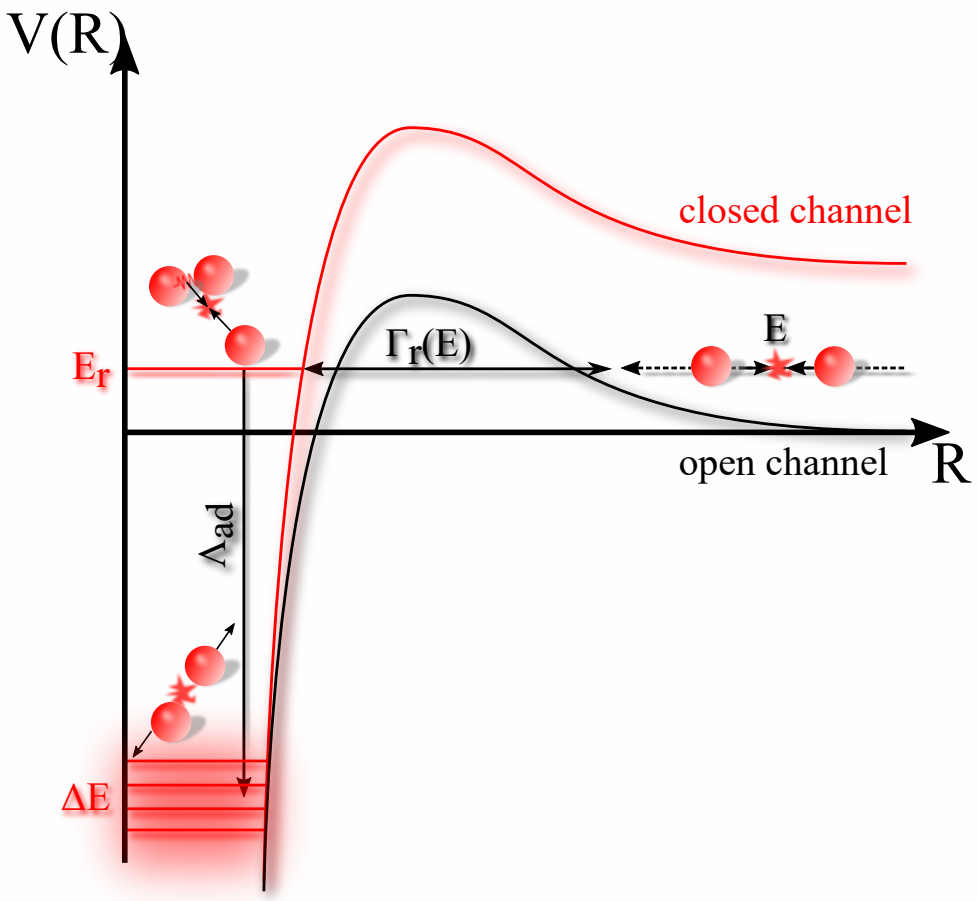

Figure 7.1: Schematic depiction of p-wave scattering process. The figure shows the open potential of the incoming scattering atoms at energy E and the closed channel with an resonant dimer state at energy E_r. Incoming atoms can tunnel through the centrifugal barrier with rate $\Gamma_r(E)$ and create weakly bound dimers with probability L_m. Weakly bound dimers can in return decay into two free atoms with rate $\Gamma_r(E)$. This process leads to energy redistribution e.g. thermalization. Weakly bound dimers colliding with a free atom lead to collapse into deeply bound dimers at rate $n\Lambda_{ad}$. This process leads to losses since ΔE sets free kinetic energy large compared to the trap depth of the atomic trap.

the resonance width is small compared to the width of the momentum distribution k_BT. K_m can then be approximated by a delta function giving the velocity condition $E_r = \frac{1}{4}m|v_1' - v_2''|^2$, the creation rate Γ_r and the volume given by the wave vector related to the de Broglie wavelength $k_{dB} = (mE)^{3/2}\hbar^{-1}$:

$$K_m(v', v'') = 3\left(\frac{4\pi^2}{k_{dB}^3}\right)\Gamma_r\delta\left(E_r - \frac{1}{4}m|\vec{v}' - \vec{v}''|^2\right) \tag{7.4}$$

the Maxwell-Boltzmann distribution $f(v)d^3v$, $\rho(v) = n\left(\frac{m}{2\pi k_BT}\right)^{3/2}\exp\left(-\frac{mv^2}{2k_BT}\right)$.

distribution of temperature T this simplifies to

$$L_m(E_r) = 3\Gamma_r \left(\frac{6\pi}{k_T^2}\right)^{3/2} \exp^{-(E_r/k_BT)} \tag{7.5}$$

where $k_T = \sqrt{3mk_BT/(2\hbar^2)}$ is the thermal relative wavenumber.
In a steady-state condition of $dn_D/dt = 0$ equation 7.2 leads to

$$n_D = \frac{L_m}{\Gamma_r + n\Lambda_{ad}} n^2 \tag{7.6}$$

We can use this to solve equation 7.1 where this leads to

$$\frac{dn}{dt} = -9 \left(\frac{6\pi}{k_T^2}\right)^{3/2} \exp^{-(E_r/k_BT)} \frac{n\Lambda_{ad}\Gamma_r}{\Gamma_r + n\Lambda_{ad}} n^2 \tag{7.7}$$

For small changes in the density one can rewrite this as

$$\frac{dn}{dt} = -L_3 n^3 \tag{7.8}$$

with

$$L_3 = -9 \left(\frac{6\pi}{k_T^2}\right)^{3/2} \exp^{-(E_r/k_BT)} \frac{\Lambda_{ad}\Gamma_r}{\Gamma_r + n\Lambda_{ad}} \tag{7.9}$$

Note that this is only valid for a small change in n since we neglect the density dependence due to atom dimer collisions in L_3 itself.

7.2 Bench marking

To verify our model we compare it to experimental data from Waseem et al. [2019]. In their experiment they investigate three-body-losses of Lithium in the $|1/2, -1/2\rangle$ state close to the Feshbach resonance at 160 G in dependence of the magnetic field detuning on the positive side of the Feshbach resonance. They extract the three body loss parameter L_3 from atom loss curves and the cascade model to extract the rate coefficient of the vibrational quenching [2] Λ_{ad} from L_3.

Figure 7.2 shows L_3 for three sets of measurements of thermalized samples at temperature of 2.7 µK, 3.9 µK and 5.7 µK for magnetic field detuning between 150 mG and 600 mG. The densities for the data sets are $n_1 = 1.2 \times 10^{18}\mathrm{m}^{-3}$, $n_2 = 1.3 \times 10^{18}\mathrm{m}^{-3}$ and $n_3 = 1.5 \times 10^{18}\mathrm{m}^{-3}$ for the respective temperatures.

Our model differs from the model presented in Waseem et al. [2019] regarding the assumption on the regime. Waseem et al. assume $\Gamma_r \gg n\Lambda_{ad}$ which leads to a three body loss coefficient of

$$L_3 = -9(6\pi/k_T^2)^{3/2} \exp^{-(E_r/k_BT)} \Lambda_{ad} \tag{7.10}$$

[2] In Waseem et al. [2019] the notation is K_{AD} for the vibrational quenching rate coefficient.

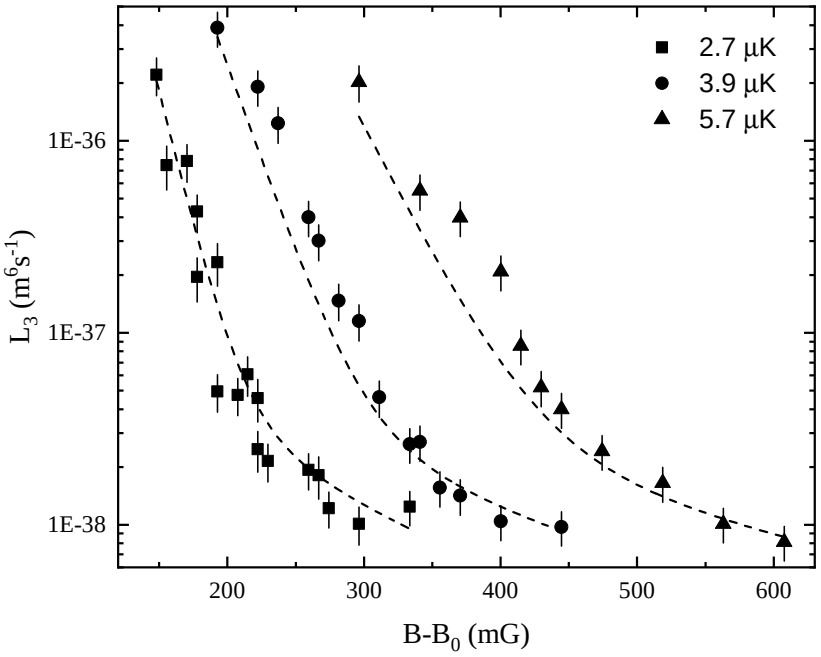

Figure 7.2: Three-body-loss parameter L_3 close to the p-wave Feshbach resonance at $B_0 = 159.17(5)\,\mathrm{G}$ provided from the publication [Waseem et al., 2019]. The data shows three different sets of temperatures of 2.7 µK, 3.9 µK and 5.7 µK for square, circle and triangles respectively. We fit equation 7.12 to the data and extract an $\Lambda_{ad} = 3.6(6) \times 10^{-14}\mathrm{m}^3\,\mathrm{s}^{-1}$.

(see section 7.3). We assume to be in the intermediate regime of $\Gamma_r \approx n\Lambda_{ad}$ which leads to the three body loss coefficient shown in equation 7.9.

To account for the whole regime covered in the data we add the weakly coupling regime [Esry et al., 2002] to the loss parameter L_3 following Waseem et al. [2019]. The data from Waseem et al. show a transition from the weakly coupling regime where $L_3 \propto V_p^{8/3}$ to the non universal regime at $k_T/k_r < 0.3$. We add the weakly coupling regime with

$$L_3^{weak} = C\frac{\hbar}{m}k_T^4 V_B^{8/3} \tag{7.11}$$

where C is the so called contact describing three-body-recombination at low momentum [Yoshida et al., 2018]. We get a total L_3 of

$$L_3 = -9\left(\frac{6\pi}{k_T^2}\right)^{3/2}\exp^{-(E_r/k_BT)}\frac{\Lambda_{ad}\Gamma_r}{\Gamma_r + n\Lambda_{ad}} + C\frac{\hbar}{m}k_T^4 V_B^{8/3} \tag{7.12}$$

Using equation 7.12 we fit all three data sets from figure 7.2 with Λ_{ad} as the only free parameter. We fix the other parameters to the values from Nakasuji et al. [2013] that are

$V_{bg}\Delta B = -2.8(3)\times10^6 {a_0}^3$ G and $k_e = 0.055(5){a_0}^{-1}$. Here V_{bg} is the background scattering volume, ΔB is the resonance width in Gauss and k_e is one over the effective range. We use these parameters to calculate the magnetic field dependent bound state energy with the scattering volume V_p via $V_p \approx V_{bg}\Delta B/(B - B_0)$, $k_r = 1/\sqrt{|V_p|k_e}$ and $E_r = \hbar^2 k_r^2/m$, where k_r is the momentum of the resonance bound state and B_0 is the resonance position in the magnetic field.

We weight each data set equally, independent of the number of points. The resulting shown curves are shown in figure 7.2. They are in very good agreement with the data. We extract the vibrational quenching rate coefficient $\Lambda_{ad} = 3.6(6)\times10^{-14}\mathrm{m}^3\,\mathrm{s}^{-1}$ [3]. Comparing Γ_r and $n\Lambda_{ad}$ we get values of $\Gamma_r/n\Lambda_{ad}$ between 3 and 24 showing, that we are in a transition regime where dimer creation as well as dimer atom loss equally contribute to the cascade loss mechanism. By including both processes in the fit function we reduce the relative error $\delta\Lambda_{ad}/\Lambda_{ad} \approx 0.17$ relative to $\delta K_{ad}/K_{ad} \approx 0.38$ from Waseem et al. [2019].

In the following calculations we will use the parameters extracted in this section. We separate two regimes where either elastic collisions dominate inelastic collisions or vice versa. We will first discuss the case of losses in a thermalized regime and afterwards take a look at non-thermalized regime.

7.3 Thermalized behavior

In this section we discuss the regimes of dominant elastic collisions. We argue that this leads to a permanent thermalized sample of atoms. Thus we assume a thermalized ensemble at any point in time. This regime has been discussed in several publications [Peng et al., 2021; Nuske et al., 2015; Horvath et al., 2017; Mathew and Tiesinga, 2013; Mathey et al., 2009] and has interesting implications as for example thermalization of a single component Fermi gas where s-wave collisions are suppressed due to the Fermi blocking, or even collisional cooling where atoms with energy above average can be lost in a controlled manner. This section will start by briefly describing the thermalized regime, then find an analytic description for the gas behavior of a thermalized gas in a box- and harmonic potential.

Two colliding atoms that scatter into a weakly bound dimer state of energy E_r can decay back into two free atoms. This elastic process leads to redistribution of kinetic energy. It is described by the probabilities $\propto \Gamma_r^2$ [Mathey et al., 2009]. In the limit $\Gamma_r \gg n\Lambda_{ad}$ the probability that these processes occur is large compared to the probability of loss due to formation of a deeply bound molecule which is given by $\Gamma_r n\Lambda_{ad}$. In other words, the ratio is given by $\tau_{el}/\tau_{in} = n\Lambda_{ad}/\Gamma_r$ and is $\tau_{el}/\tau_{in} \ll 1$. Looking at equation 7.7 the limit of large elastic collisions leads to

$$\frac{dn}{dt} = -9(6\pi/k_T^2)^{3/2}\exp^{-(E_r/k_BT)}\Lambda_{ad}n^3 = -L_3n^3 \tag{7.13}$$

[3] Due to a difference in the definition of L_3 as compared to [Waseem et al., 2019], our Λ_{ad} is not comparable to their parameter K_{ad}.

In this limit the loss is of three-body nature since it depends on the density cubed. The rate Γ_r is not relevant to the process. As soon as three atoms are close to each other and two of the atoms fulfill the kinetic energy constraint given by the delta function in equation 7.4, Λ_{ad} probes if a loss happens. The average energy of lost atoms E_{loss} due to E_r is given by the average collision energy $3/2k_BT$ and E_r by $E_{loss} = E_r + 3/2k_BT$. By looking at the averaged energy of the lost atoms we can construct a temporal development of the temperature following the equation [Nuske et al., 2015]

$$\frac{dT}{dt} = -L_3 n^2 \frac{T}{3}(\frac{3}{2} - \eta) \tag{7.14}$$

where we call $\eta = E_r/k_BT$ the truncation parameter. When $\eta < 3/2$ the losses lead to heating of the gas. This can be understood in the picture of manly low momentum atoms fulfilling the loss condition and being lost. Redistribution of energy then leads to heating. For $\eta > 3/2$ the gas is cooled. This on the other hand can be understood in the picture of mainly high energy particles fulfilling the loss conditions. Thus redistribution of energy leads to cooling. Looking at the development of the phase-space-density ρ we get

$$\frac{d\rho}{dt} = -L_3 n^2 \frac{\rho}{2}\left(\frac{7}{2} - \eta\right) \tag{7.15}$$

leading to an increase of phase-space-density for $\eta > 7/2$ an a decrease for $\eta < 7/2$. As pointed out in [Mathey et al., 2009; Nuske et al., 2015; Peng et al., 2021] this is a form of collisional cooling. When choosing η to be above a certain value, only energetically high atoms are extracted from the sample. This happens almost analogous to evaporative cooling [Ketterle and Druten, 1996]. In evaporative cooling the atoms with energy large compared to the trapping potential are lost from the sample if they reach the potential border. In collisional cooling atoms are lost via the collisional energy condition. An efficient evaporation is reached for a truncation parameter $\eta = U_0/k_BT > 6$, where U_0 is the trap depth. [Ketterle and Druten, 1996] defines an evaporation efficiency parameter γ to characterize the cooling efficiency with $\gamma = \log(\rho_0/\rho)/\log(N_0/N)$. For efficient evaporation γ can reach values up to 4. For collisional cooling in a box potential we get

$$\gamma = \frac{\eta}{2} - \frac{7}{4} \tag{7.16}$$

For a good cooling efficiency of $\gamma = 4$ we thus need $\eta = 11.5$. For a Lithium 6 gas at $T = 2\,\mu\text{K}$, $n = 1 \times 10^{12}\text{cm}^{-3}$ this leads to a loss time of $\tau_3 \approx 1\,\text{s}$. The described increase and decrease of the temperature can be seen in figure 7.3 showing the temporal evolution of the temperature inside a box potential for different η_0. Here $\eta(t = 0) = \eta_0 = E_r/k_BT_0$ is the initial truncation parameter. Time is given in units of τ where

$$\tau = 9\Lambda_{ad}(6\pi/k_T^2)^{3/2} exp^{-9/2} n_0^2 t \tag{7.17}$$

the three body timescale for $\eta = 9/2$. As discussed before on $\eta_0 = 3/2$ the temperature does not change. The small decrease in T for large η_0 is given by the decreasing atom loss. Note that η is here time dependent since T is changing. Figure 7.4a shows the temporal

evolution of the phase-space-density ρ for different η_0. Here ρ stays constant for $\eta_0 = 7/2$.

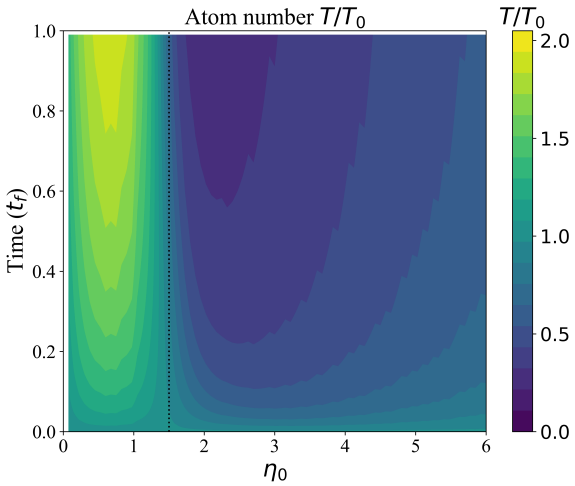

Figure 7.3: Temporal development of temperature T/T_0 for different initial truncation parameter η_0 in a box. Time is given in τ from equation 7.17. The dashed line shows $\eta_0 = 3/2$ where the temperature stays constant. For $\eta_0 < 3/2$ the temperature of the gas increases. For $\eta_0 > 3/2$ the temperature decreases due to three body losses over energetically high particles.

In a harmonic trap two additional effects lead to a small change in the behavior compared to a gas in a box potential. The so called anti evaporation leads to an additional heating effect. The position dependent density leads to increase losses in the center of the trap. Due to the spatially dependent potential energy, atoms with above average potential energy are lost from the trap [Weber et al., 2003]. This leads to an additional energy loss per particle of $3/2k_BT$. Compared to 7.14 this leads to a temperature evolution of

$$\frac{dT}{dt} = -L_3 n^2 \frac{T}{3} (3 - \eta) \tag{7.18}$$

A second effect is the temperature dependent density which leads to a difference in temperature dependence of the phase-space-density ρ. Compared to 7.15 we get

$$\frac{d\rho}{dt} = -L_3 n^2 \rho (4 - \eta) \tag{7.19}$$

Even though one needs a larger $\eta > 3$ for a negative change in temperature and a larger $\eta > 4$ for a positive change in phase-space-density, the evaporation efficiency γ itself is larger compared to 7.16 with

$$\gamma = \eta - 4 \tag{7.20}$$

Here an efficient evaporation with $\gamma = 6$ is achieved with $\eta = 10$. For a Lithium 6 sample at $T = 2\,\mu\text{K}$, a density of $n = 1 \times 10^{12}\text{cm}^{-3}$ the loss time is $\tau_3 \approx 200\,\text{ms}$. This

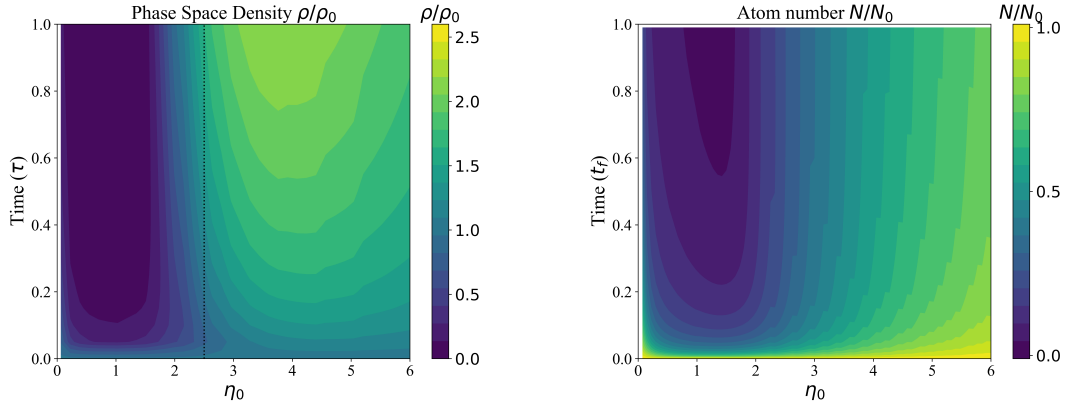

(a) **(b)**

Figure 7.4: Temporal development of a) phase-space-density ρ over initial phase-space-density ρ_0 and b) of atom number N for different initial truncation parameter η_0 in a box. Time is given in τ from equation 7.17. The dashed line in a) shows $\eta_0 = 7/2$, the border where the phase-space-density of the gas stays constant. Left of the line the phase-space-density decreases due to decreasing density and increasing temperature. To the right of the line the phase-space-density decreases due to decreasing temperature even though density is decreasing.

makes efficient collisional cooling in a harmonic trap a good method for efficient cooling.

7.4 Non-Thermalized behavior

In the case where $\Gamma_r \ll n\Lambda_{ad}$ elastic collisions are small compared to inelastic collisions. Thermalization is no longer assumed since losses are fast compared to thermalization. We will here show that this process lead to out of equilibrium losses where we start with a thermal distribution and end up with a velocity distribution that does not follow the Maxwell-Boltzmann distribution. To do this we describe equation 7.1 including a random velocity distribution function $f(v)$

$$\frac{dn}{dt}f(v) = 2\Gamma_r n_D f(v) - 2\int K_m(v,v')n^2 f(v')dv' f(v) - \Lambda_{ad} n n_D f(v) \tag{7.21}$$

Note that $nf(v) = \rho(v)$ describes the phase space distribution and that $\dot{\rho}(v) = \dot{n}f(v)$. The dimer density distribution, multiplied with $f(v)$ is given by

$$\frac{dn_D}{dt}f(v) = -\Gamma_r n_D f(v') + \int K_m(v',v'')n^2 f(v')dv' f(v'')dv'' f(v) - \Lambda_{ad} n n_D f(v) \tag{7.22}$$

Including both equations with the steady-state condition $dn_D/dt = 0$ we end up with

a velocity dependent phase-space-density description of

$$\begin{aligned}\frac{d\rho(v)}{dt} =& -2\int K_m(v,v')\rho(v)\rho(v')dv' \\ &+2\int K_m(v'',v''')\rho(v'')\rho(v''')dv''dv'''\frac{\rho(v)}{n} \\ &-3\frac{\Lambda_{ad}}{\Gamma_r+n\Lambda_{ad}}\int K_m(v'',v''')\rho(v'')\rho(v''')dv''dv'''\rho(v)\end{aligned} \tag{7.23}$$

In the non-thermalization limit of $\Gamma_r \ll n\Lambda_{ad}$ we get the final equation

$$\frac{d\rho(v)}{dt} = -2\int K_m(v,v')\rho(v)\rho(v')dv' - \int K_m(v'',v''')\rho(v'')\rho(v''')dv''dv'''\frac{\rho(v)}{n} \tag{7.24}$$

The first thing to note here, is that the loss is no longer dependent on the density cubed but instead depends on the density squared. This becomes clear when looking at it for a thermal distribution [4] where we get

$$\frac{dn}{dt} = -9\left(6\pi/k_T^2\right)^{3/2}\exp^{-(E_r/k_BT)}\Gamma_r n^2 = -L_2 n^2 \tag{7.25}$$

This can be understood by assuming that each creation of a dimer immediately leads to loss of the dimer and an additional atom. Thus the triggering of the loss process only depends on the dimer creation probability which is dependent on the density squared.

The second thing to note are the two different terms in equation 7.24. They describe two different roles of the observed atom described by $\rho(v)$. In the first term the observed atom is part of the dimer creation process and has to follow the energy condition of $K_m(v,v')$. The atom can participate in the process in the two different positions of the two dimer atoms, leading to the factor of 2. In the second term the atom follows the role of the observer, colliding with an existing dimer.

Figure 7.5, 7.6a and 7.6b show the development of a momentum distribution for $\eta_0 = 8/2$, $\eta_0 = 0/2$, $\eta_0 = 5/2$ respectively. The time unit is given by

$$t_f = 9\Gamma_r(6\pi/k_T^2)^{3/2}exp^{-9/2}n_0 t \tag{7.26}$$

In the case of $\eta_0 = 8/2$ and $\eta_0 = 5/2$ for $t_f = 20$ the exponential tail of the initial Maxwell-Boltzmann distribution is completely lost. Figure 7.7a shows the temporal evolution of the variance of the energy distribution. In the case of a thermal distribution $\langle E_v\rangle = 3/2k_BT$. For $\eta_0 > 3/2$ the average energy per particle decreases linear in η. The position of the minimum is dependent of the time t at which one looks. For $\eta_0 < 3/2$ the average energy increases. Figure 7.7b shows the number of atoms N/N_0 for different times t_f.

[4] The thermalization is only assumed at the initialization time. As we discussed before the losses will lead non-thermal distributions

A description of a harmonic potential in the non-thermal case poses additional challenges that are beyond the scope of this work. Due to the spatially dependent density, loss times are spatially dependent. In absence of thermalization this leads to a non trivial coupling of density and momentum distributions. To access information about resulting phase space distributions Monte-Carlo simulations are a promising method.

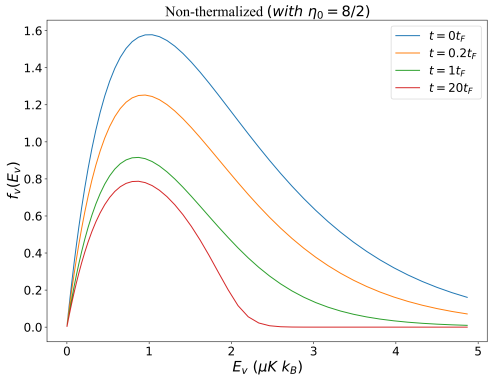

Figure 7.5: Temporal development of energy distribution f_v in non-thermal regime of three body losses in a cascade process close to a p-wave Feshbach resonance for $\eta_0 = 4$. Development of velocity distribution starting from a Maxwell-Boltzmann distribution at $t = 0t_f$ where t_f is given by equation 7.26. For $t = 20t_f$ the exponential tail of the distribution is gone.

7.5 Regimes

After seperating and discussing the thermal and the non-thermal regime, in this section we discuss the constraints and accessibility of the different regimes and give some further limiting factors for experimental observation of the described effects. Figure 7.8 shows a sketch of the different regimes on a log-log scale of temperature over density. The transitions between the regimes are not as clear as shown in the sketch. Instead the sketch shows borders where the relevant timescales of the neighboring regimes are equal. Five different regimes can be described

The thermal regime is given in the case of $\Gamma_r \gg n\Lambda_{ad}$ and is described in section 7.3. Here the atomic loss is of three body nature, depends on the coupling strength of weakly bound dimers to deeply bound dimers Λ_{ad} and the dominating elastic collisions lead to a thermalized gas. Mathey et al. [2009] discuss the possibility to combine two p-wave resonance. One resonance plays the role of the knife edge losses discussed here and the other broad lossless resonance leads to elastic collisions.

The non-thermal regime is given in the case of $\Gamma_r \ll n\Lambda_{ad}$ and is described in section 7.4. Here the atomic loss is of two-body nature, depends on the resonance width

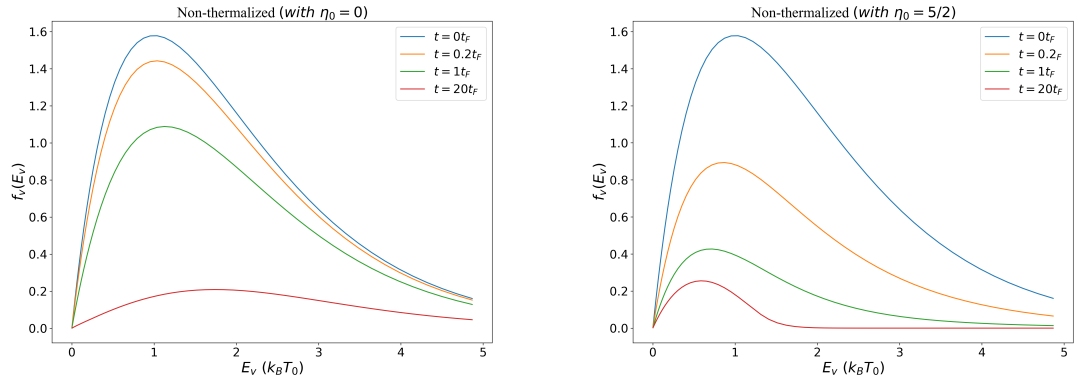

(a) **(b)**

Figure 7.6: Temporal development of energy distribution f_v in non-thermal regime of three body losses in a cascade process close to a p-wave Feshbach resonance for a) $\eta_0 = 0$ and b) $\eta_0 = 5/2$. Development of velocity distribution starting from a Maxwell-Boltzmann distribution at $t = 0t_f$ where t_f is given by equation 7.26. For a) the maximum of the distribution shifts to higher energies. For b) the maximum shifts to lower energies and the exponential tail of the distribution is lost.

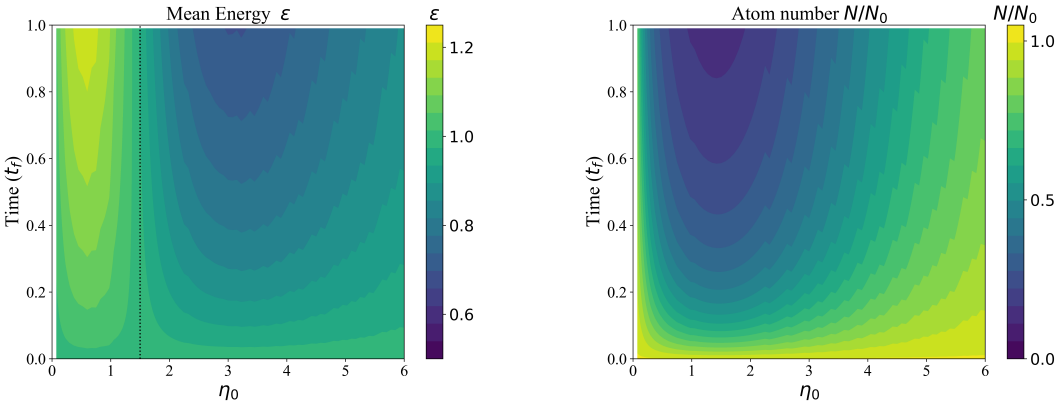

(a) **(b)**

Figure 7.7: Temporal development of a) mean energy $\epsilon = \langle E_{kin} \rangle / (\frac{3}{2} k_B T_0)$ and b) of the atom number N/N_0 for different initial truncation parameter η_0 in a box potential. Time is given in t_f from equation 7.26.

Γ_r and the dominating inelastic collisions lead to a gas out of thermal equilibrium. The calculations of the thermal and the non-thermal regime rely on the condition that $\Gamma_r + n\Lambda_{ad} \ll k_B T/\hbar$, because an infinetely narrow resonance was assumed.

The broad resonance Regime is reached when $\Gamma_r + n\Lambda_{ad} \gg k_B T/\hbar$ where the resonance width is large compared to the thermal distribution. In this case the loss process is no longer momentum dependent and equally distributed over the whole momentum distribution.

The non universal regime is reached when $0.3 < k_T/k_r < 1$ where $k_r = \sqrt{mE_r/\hbar^2}$ is the wave vector related to the bound state energy E_r. For $0.3 > k_T/k_r$ or $k_T/k_r > 1$ we reach the weakly coupling regime or the unitarity regime respectively as discussed in detail in [Yoshida et al., 2018]. This regime translates into a condition of the truncation parameter $1.5 < \eta < 15$.

The non-degenerate regime is reached when $k_f \ll k_T$ where $k_f = n^{1/3}$ is the wave vector related to the inter particle distance. In the degenerate regime the momentum distribution no longer follows a Maxwell-Boltzmann distribution but instead a Fermi distribution. The behavior of a gas in the transition regime es described in [Mathey et al., 2009].

The 1B loss regime is reached when the one body loss timescale due to background losses τ_1 is short compared to the three body loss scale $\tau_3 = (L_3 n^2)^{-1}$ in the thermalized case or $\tau_3 = (L_2 n)^{-1}$ in the non-thermalized case. In the presence of other loss processes, all loss processes should be slow compared to the losses described in this section.

For ^{6}Li in the lowest hyperfine state $|1/2, -1/2\rangle$ at the resonance close to 160 G, the thermal regime can be reached for $n = 1 \times 10^{12}\text{cm}^{-3}$, $T = 2\mu\text{K}$ and $\eta_0 = 10$ which corresponds to a magnetic field detuning of $\Delta B = 85\,\text{mG}$.

The non-thermal regime can be reached for example for parameters of $n = 1 \times 10^{12}\text{cm}^{-3}$, $T = 600\text{nK}$ and $\eta_0 = 10$ which corresponds to a magnetic field detuning of $\Delta B = 30\,\text{mG}$.

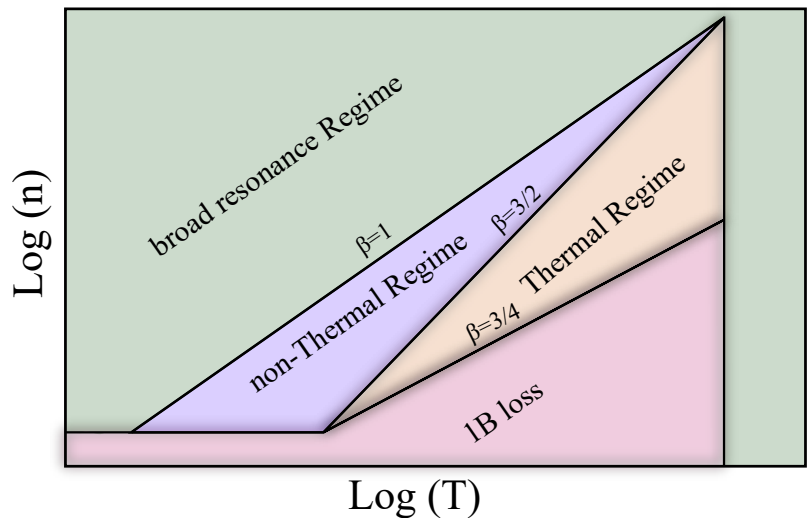

Figure 7.8: Regimes for different loss behavior in an ultracold atomic sample undergoing p-wave interactions for different density n and temperature T at a fixed η between $1.5 < \eta < 15$. The thermal regime (orange) is described in section 7.3. Here elastic collisions are large compared to inelastic collisions. The non-thermal regime (purple) is described in section 7.4. Here inelastic collisions are large compared to elastic collisions. In the broad resonance regime (green), the resonance width is large compared to the width of the temperature distribution. A $K_m(v, v')$ described by a delta function is no longer a valid assumption. Measurements in section 5 and 6 are taken in this regime. In the 1B loss regime (red), one body losses induced by background scattering are large compared to three body losses. β indicates the corresponding exponential scalings $n \propto T^{\beta}$ for the regime dividing borders.

Conclusion and Outlook

In this work we studied and explored p-wave Feshbach resonances in ultracold farmionic ^{6}Li gases and in ultracold Bose-Fermi mixtures of ^{6}Li-^{133}Cs via high-resolution atom-loss spectroscopy. In this context, we improved our efficiency in the production scheme of ultracold ^{6}Li samples and precisely characterized the topology of our magnetic fields. We presented the implementation of gray molasses cooling on the D_1-line of ^{6}Li, as a further optical cooling step, increasing the phase space density after optical cooling by a factor of twelve, compared to the old apparatus. An adapted and improved dipole trap loading sequence with a spatially modulated dipole trap was implemented to account for the modified starting conditions of the optically cooled gas. Here we increased the number of loaded atoms by a factor of five with a decrease in temperature by a factor of four. We showed that this allows us to produce a ^{6}Li double component degenerate BEC with up to 3×10^5 molecules. Ultracold ^{6}Li-^{133}Cs mixtures are produced at temperatures as low as 200 nK. A precise characterization of the magnetic field landscape has been performed using ^{6}Li radio-frequency and ^{133}Cs microwave spectroscopy. Compensation of the earth magnetic field and determination of the Feshbach field curvature, in three spatial directions allows absolute magnetic field precisions down to 10 mG with relative resolutions as low as 1 mG.

With this improved experimental apparatus we investigated ^{6}Li and ^{6}Li-^{133}Cs p-wave Feshbach resonances with an angular momentum of $l = 1$ at ultra low temperatures and high magnetic field precision. We performed atom loss spectroscopy on three ^{6}Li and five ^{6}Li-^{133}Cs p-wave Feshbach resonances.

Doublet structures were observed on five of the eight resonances and triplet structures on the remaining three ^{6}Li and ^{6}Li-^{133}Cs resonances. Comparing the experimentally found splittings with elaborate coupled channel calculations performed by Eberhard Tiemann we attributed the doublet structure to spin-spin coupling lifting the degeneracy of $m_l = 0$ and $|m_l| = 1$ projections of the pair rotation.

For the first time we observed triplet structures on p-wave Feshbach resonances at high magnetic field. Three ^{6}Li-^{133}Cs p-wave resonances showed a further splitting of the $|m_l| = 1$ resonance. Via the coupled channel calculations we attributed these splittings to spin-rotation coupling, lifting the degeneracy of the $m_l = +1$ and $m_l = -1$ p-wave pair rotation orientation. The spin-rotation splitting dependence on $\langle S_z \rangle$ explains the observed and non-observed splittings on three out of five ^{6}Li-^{133}Cs resonances. Other contributions to the observed splitting, such as the rotational Zeeman effect or the molecular anisotropy

of the electron g-tensor, were excluded or are negligible small. A fit of the coupled channel calculation to the resonances yields the dimensionless spin-rotation coupling constant $|\gamma| = 0.566(50) \times 10^{-3}$.

The observed spin-rotation interaction is well known in molecular physics [Brown and Alan, 2003] but shows to be unexpectedly large in Feshbach molecules. A calculation of γ using electron model wave functions leads to a significant underestimation of the spin-rotation coupling constant. We attribute the deviation to a strong under representation of the model wave function at low inter nuclear separations. Inversely, this suggests that γ can act as a high precision measure for electron wave functions at short internuclear distances.

Additionally, the temperature dependence of the ^{6}Li p-wave resonance at 214 G and the ^{6}Li-^{133}Cs p-wave resonance at 663 G was investigated. As expected, no significant temperature dependence on the spin-spin or spin-rotation splitting could be observed. However, the change in resonance position and width of the ^{6}Li signal suggests two- and three-body loss contributions to the loss signal.

The observed splittings opens the door to new investigations in spin-polarized Fermi gases near p-wave Feshbach resonances. Predictions of phase transitions from a polar p_x state to an axial $p_x + ip_y$ state as well as the topological transition from a gapless to a gapped p_x+ip_y phase state promises rich structures in the p-wave superfluid phase diagram [Botelho and Sá de Melo, 2005; Gurarie et al., 2005; Cheng and Yip, 2005]. Despite great efforts to understand and to control the large inelastic losses close to single-component p-wave Feshbach resonances, the realization of a stable p-wave superfluid in quantum gases is still challenging [Zhang et al., 2004; Schunck et al., 2005; Regal et al., 2003; Waseem et al., 2018, 2019]. Confining the gas in spatial dimensions has proven to be a promising route to suppress losses and realize p-wave superfluid pairing [Günter et al., 2005; Waseem et al., 2017; Zhou and Cui, 2017]. Goyal et al. [2010] proposed that optical coupling to an excited electronic state can also lead to suppressed losses. Resolving the different $m_l = -1, 0, +1$ projections gives a further important tool for the individual control of the rotational states. Studies that have previously only been possible in ^{40}K due to the large splitting of the m_l components, such as the study of p-wave contact, can now be extended to ^{6}Li [Luciuk et al., 2016]. The temperature dependent decrease in width shows that accessing lower temperatures is beneficial since the temperature broadened width is still a limiting factor in individual resonance control.

The newly observed spin-rotation splitting in p-wave Feshbach resonances is also expected for other bi-alkali dimers with large mass imbalance such as Li-Rb and Na-Cs. Predicting the splittings is non-trivial as our simple model approach showcased. Nevertheless, a large mass imbalance and a large spin-orbit coupling constant promotes large spin-rotation coupling. Also here low temperatures and high magnetic field resolutions are key requirements for the observation of said splittings. We performed an attempt to observe spin-rotation coupling on the 214 G p-wave ^{6}Li resonance by lowering the temperature down to 50 nK. Apart from a large difference in resonance width between the two peaks, that has already been observed for higher temperatures, nothing hints towards

an observable splitting of the $m_l = -1$, $m_l = 1$ states. Also by confining the gas to lower spatial dimensions, these states can not be distinguished [Günter et al., 2005]. Peng et al. [2018] showed that optical manipulation of the individual closed-channels might enables access to the different m_l states.

It is compelling that atom loss spectroscopy provides the means and resolution to investigate molecular fine structure. By further decreasing the temperature dependent width, the spectroscopy resolution can be increased thus opening the door for the exploration of further molecular sub-structure. While for *s*-wave Feshbach resonances rf spin flip association of Feshbach dimers is a very precise method to determine the resonance pole [Wu et al., 2012; Ulmanis et al., 2015], for *p*-wave dimers the wave function overlap to the free atoms is limiting the rf association rate, hindering this approach. However, Ahmed-Braun et al. [2021] investigated the *p*-wave Feshbach dimer states very precisely via rf spin flip association and resonant association.

Furthermore, a theoretical study on the behavior of losses close to the ^{6}Li $|1\rangle\oplus|1\rangle$ *p*-wave Feshbach resonance, was performed. The presented cascade model of a dimer creation followed by an atom-dimer collision, features two different loss regimes. For larger temperatures, thermalization and losses can lead to collisional cooling very similar to evaporative cooling. We showed that cooling efficiencies of $\gamma^{evap} > 4$ are accessible over almost four orders of magnitude in temperature. For low temperatures thermalization is slow compared to losses leading to non-equilibrium momentum distributions. We show that the separation of the two regimes can be observed experimentally though a qualitative change in loss behavior. The thermalized regime exhibits three-body losses whereas the non-thermalized regime follows a two-body loss behavior.

In comparison with collisional cooling on narrow *s*-wave Feshbach resonances [Peng et al., 2021], the centrifugal barrier in *p*-wave Feshbach resonances leads to a narrowing of the resonance width for lower momentum, which in turn leads to a lower limit for the final temperature [Wigner, 1948]. Additionally, our study predicts that *p*-wave Feshbach resonances can be used to create single component ultracold thermalized samples of fermions. A task that is not easily achieved since regular evaporation is suppressed due to forbidden elastic *s*-wave collisions [Nakasuji et al., 2013].

Schmidt et al. [2020] predicts a three body state at the low momentum side of the *p*-wave resonance. Even though the predicted loss amplitude is small compared to the discussed two body loss channel, this resonance could significantly alter our predicted cooling efficiency. Top et al. [2021] recently showed, that *p*-wave resonances can be used to perform evaporative cooling in the weak coupling regime. In that case, the large momentum dependence of the elastic scattering lead to a non-thermal distribution, seen as an underrepresentation of the low momentum part.

Even though great effort has been made to study losses near *p*-wave resonances [Regal et al., 2003; Suno et al., 2003; Zhang et al., 2004; Waseem et al., 2017; Yoshida et al., 2018; Waseem et al., 2018, 2019] qualitative change in loss behavior from three- to two-body loss has not been observed. Due to the broad regime range this should be easily accessible in an ultracold ^{6}Li system. Additionally, performing expansion measurements in a pancake-

shaped trap will reveal the predicted non-equilibrium momentum distributions.

An ultracold ^{6}Li-^{133}Cs system will also in the future enable access to interesting physical regimes surrounding p-wave Feshbach resonances. Beside the investigation of few-body physics in ^{6}Li-^{133}Cs mixtures, the experiment is currently being upgraded for studying many-body physics in the polaron scenario where an impurity interacts with a degenerate Bose (Bose polaron) or Fermi (Fermi polaron) gas. Analogue to the study on Bose- and Fermi-polarons near s-wave resonances, that show special behavior due to the large mass imbalance of ^{6}Li-^{133}Cs [Tran et al., 2021; Enss et al., 2020; Sun et al., 2017; Sun and Cui, 2017], polarons close to p-wave Feshbach resonances are expected to exhibit rich polaronic state structure due to the lifted m_l degeneracy [Levinsen et al., 2012].

In conclusion, the ^{6}Li-^{133}Cs experiments holds exciting prospects for further studies exploiting the here presented rich structure of ^{6}Li-^{133}Cs p-wave Feshbach resonances.

A. Appendix

A.1 Improved Optical Setup for Gray Molasses Cooling

In this section we present the improved optical setup for gray molasses cooling on the D1-line of ^{6}Li. The first optical setup has been presented in Gerken [2016] but improved for more flexibility and stability in power. Figure A.1 shows the optical setup. A Toptica TA-Pro laser system with a main output power of 350 mW and a spectroscopy output of around 1 mW is used to generate light at around 671 nm. The spectroscopy output is used for a FM-spectroscopy (frequency modulation) laser stabilization setup that locks the laser detuned by +156 MHz from the $|f = 3/2\rangle \rightarrow |f' = 1/2, 3/2\rangle$ transition. The main output of the laser is coupled into a PM8-NIR electro optical modulator (EOM) from QUBIG producing sidebands at 224.8 MHz. The light is separated into two beams. The first beam with around 250 mW is coupled into an acousto optical modulator (AOM) for power and switching control. The beam is coupled into a fiber that produces the light in x_3 direction of the gray molasses cooling (see figure 1.4). The other beam with a power of 12 mW is coupled into a home build tapered amplifier system [Faraoni, 2014] increasing the power to around 350 mW. After passing through a set of two lenses the light is again separated into two equally powered beams. The beams are frequency shifted by an AOM at frequency of -114 MHz and are coupled into optical fibers to produce the light in x_1 and x_2 direction for the gray molasses cooling (see figure 1.4). Figure A.2 shows the light frequencies produced in this setup. The beams carry a cooler frequency $|f = 3/2\rangle \rightarrow |f' = 1/2, 3/2\rangle + \delta$ and a repumper frequency $|f = 1/2\rangle \rightarrow |f' = 1/2, 3/2\rangle + \delta$ with a power ratio of $I_{cool}/I_{rep} \approx 10$. The total detuning is fixed at $\delta \approx 30$ MHz from the $|f' = 3/2\rangle$ state.

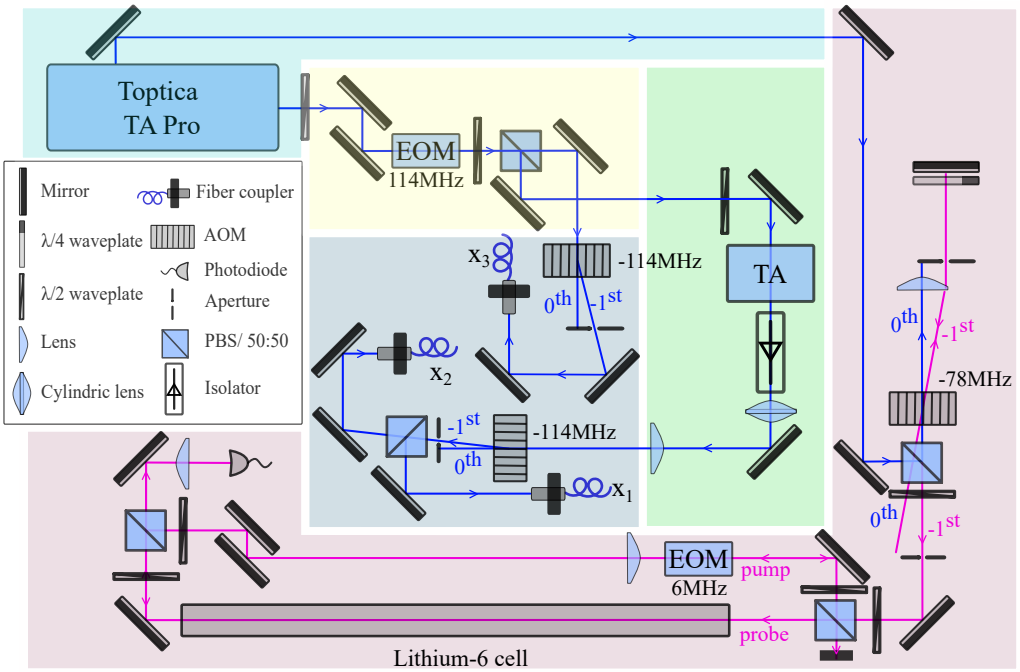

Figure A.1: Gray molasses optical setup scheme for the preparation of the light frequencies presented in figure A.2. The optical elements are explained in the legend. The background color coding divides the setup into five parts: The laser system is shown in teal. A Toptica TA-Pro provides light at 671 nm with a spectroscopy output at 1 mW (top) and main output at 350 mW (right). The FM laser lock system is shown in red. An AOM double pass shifts the laser frequency to -156 MHz. ^{6}Li heated to 635 K inside a vacuum cell, acts as a frequency reference for the frequency stabilization to the $|f = 3/2\rangle \rightarrow |f' = 1/2, 3/2\rangle$ transition. In the yellow part the repumper light is created via a frequency sideband at 228.2 MHz by an EOM. The light is amplified using a home build TA system marked by the green area. Here 12 mW are amplified to 350 mW. In the blue shaded area the light is shifted by two AOMs by -114 MHz and finally coupled into three fibers for x_1, x_2 and x_3 direction.

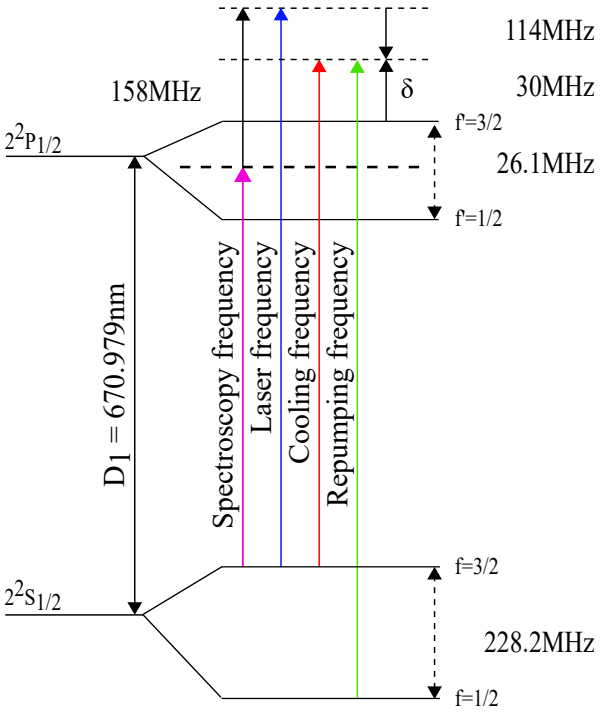

Figure A.2: ^{6}Li level scheme on the D_1-line with light frequencies used in gray molasses cooling. The Toptica TA-Pro laser is locked to the $|f = 3/2\rangle \rightarrow |f' = 1/2, 3/2\rangle$ transition (pink) but offset by -156 MHz (blue) via an AOM double pass. An EOM at a frequency of 228.2 MHz produces a sideband that is overlapped with the carrier frequency. Both frequencies are again shifted by -114 MHz to generate the cooling frequency (red) and the repumper frequency (green) detuned by *delta* ≈ 30 MHz from the $|f' = 3/2\rangle$ state.

A.2 Calculations for Spin-Rotation coupling

In this appendix we present the extended calculations to the first-order spin-rotation parameter $\gamma^{(1)}$. We consider the contribution from Cesium and Lithium separately and use the introduced simple model wavefunction from equation 6.4. Our starting point is the spin-rotation Hamiltonian as presented in equation 6.10

$$H_{sr}^{(1)} = -g\alpha^2 B(R)\vec{l}\cdot\sum_{\beta,i} Z_{i\beta}\frac{z_\beta(z_i - z_\beta)}{r_{i\beta}^3}\vec{s}_i \tag{A.1}$$

Using the electron model wavefunction and the coordinate system as presented in figure 6.4 we get for the different contributions

$$\begin{aligned}\gamma_{Cs}^{(1)}(R) &= -g\alpha^2\left\langle\Psi;R\right|\left[\frac{Z_{1Li}z_{Li}(_r+r_{1Cs}\cos(\theta_{Cs})}{(R^2+r_{1Cs}^2-2Rr_{1Cs}\cos(\theta_{Cs})^{3/2}}+\frac{Z_{1Cs}z_{Cs}}{r_{1Cs}^2}\cos(\theta_{Cs})\right]\left|\Psi;R\right\rangle\\ &= -\frac{g\alpha^2}{1+\eta}\left\langle\Psi;R\right|\left[\frac{Z_{1Li}\eta}{R}\sum_{n=0}^{\infty}(n+1)P_n(\cos(\theta_{Cs}))(\frac{r_{1Cs}}{R})^n+\frac{Z_{1Cs}R}{r_{1Cs}^2}\cos(\theta_{Cs})\right]\left|\Psi;R\right\rangle\end{aligned} \tag{A.2}$$

where $z_{Li} = \frac{\eta}{1+\eta}R$, $z_{Cs} = -\frac{\eta}{1+\eta}R$ and $\eta = 22.1$ is the mass ratio between ^{133}Cs and ^{6}Li. $P_n(\cos(\theta_{Cs}))$ are the Legendre polynomials. The first-order contribution from Lithium can be similarly written as

$$\begin{aligned}\gamma_{Li}^{(1)}(R) &= -g\alpha^2\left\langle\Psi;R\right|\left[\frac{Z_{1Cs}z_{Cs}(_r+r_{1Li}\cos(\theta_{Li})}{(R^2+r_{1Li}^2-2Rr_{1Li}\cos(\theta_{Li})^{3/2}}+\frac{Z_{1Li}z_{Li}}{r_{1Li}^2}\cos(\theta_{Li})\right]\left|\Psi;R\right\rangle\\ &= -\frac{g\alpha^2}{1+\eta}\left\langle\Psi;R\right|\left[\frac{Z_{1Cs}\eta}{R}\sum_{n=0}^{\infty}(n+1)P_n(\cos(\theta_{Li}))(\frac{r_{1Li}}{R})^n+\frac{Z_{1Li}R}{r_{1Li}^2}\cos(\theta_{Li})\right]\left|\Psi;R\right\rangle\end{aligned} \tag{A.3}$$

The integrals in equation A.2 and A.2 have a general expression of

$$\begin{aligned}I_{l,m_l;n} &= \int Y_l^{m_l^*}(\theta,\phi)P_n(\cos\theta)Y_l^{m_l}(\theta,\phi)d\theta d\phi\\ &= \frac{2l+1}{2}\int P_l^{-m_l}(\cos\theta)P_n(\cos\theta)P_n^{m_l}(\cos\theta)d\theta\end{aligned} \tag{A.4}$$

Here $Y_l^{m_l}(\theta,\psi) = (-1)^{m_l}\sqrt{\frac{2l+1}{4\pi}\frac{(l-m_l)}{(l+m_l)}}P_l^{m_l}(\cos\theta)\exp^{im_l\psi}$ are the spherical harmonics with the associated Legendre Polynomials. Only the s and p states are involved with $(\ell = 0, m_l = 0)$ and $(\ell = 1, m_l = 0, \pm 1)$. For $I_{0,0;n} = \delta_{n,0}$, $I_{1,0;n} = \delta_{n,0} + \frac{2}{5}\delta_{n,2}$ and

$I_{1,\pm1;n} = \frac{1}{2}(-\delta_{n,0} + \frac{2}{5}\delta_{n,2})$ we get the simplified forms

$$\gamma_{Cs}^{(1)} = g\alpha^2 \frac{\eta}{(1+\eta)R}\left[1 + |c_{1,\pm1}|^2\left(\frac{7}{2} + \frac{27\langle r_{1Cs}^2\rangle}{5R^2}\right)\right] \tag{A.5}$$

and

$$\gamma_{Li}^{(1)} = g\alpha^2 \frac{\eta}{(1+\eta)R}\left[1 + |c_{1,\pm1}|^2\left(\frac{7}{2} + \frac{27\langle r_{2Li}^2\rangle}{5R^2}\right)\right] \tag{A.6}$$

The final approximation can be made for $c_{1,m} \ll 1$ and $R \gg r_{1Cs}, r_{2Li}$ such that we finally get

$$\gamma^{(1)}(R) = \left[\gamma_{Cs}^{(1)} + \gamma_{Li}^{(1)}\right]/2 \approx \frac{g\alpha^2}{2R} \tag{A.7}$$

Bibliography

Ahmed-Braun, D. J. M., Jackson, K. G., Smale, S., Dale, C. J., Olsen, B. A., Kokkelmans, S. J., Julienne, P. S., and Thywissen, J. H. (2021). Probing open- and closed-channel p-wave resonances. *Phys. Rev. Research*, 3(033269):1–22.

Arimondo, E. (1991). Laser manipulation of atoms and ions. In Phillips, W. D. and Strumia, F., editors, *International School of Physics*.

Bartenstein, M., Altmeyer, A., Riedl, S., Geursen, R., Jochim, S., Chin, C., Denschlag, J. H., Grimm, R., Simoni, A., Tiesinga, E., Williams, C. J., and Julienne, P. S. (2005). Precise determination of ^{6}Li cold collision parameters by radio-frequency spectroscopy on weakly bound molecules. *Physical Review Letters*, 94(10):1–4.

Bartenstein, M., Altmeyer, A., Riedl, S., Jochim, S., Chin, C., Denschlag, J. H., and Grimm, R. (2004). Collective excitations of a degenerate gas at the BEC-BCS crossover. *Physical Review Letters*, 92(20):90–93.

Bazak, B. and Petrov, D. S. (2018). Stable p-Wave Resonant Two-Dimensional Fermi-Bose Dimers. *Physical Review Letters*, 121(26):263001.

Bell, S. C., Junker, M., Jasperse, M., Turner, L. D., Lin, Y. J., Spielman, I. B., and Scholten, R. E. (2010). A slow atom source using a collimated effusive oven and a single-layer variable pitch coil Zeeman slower. *Review of Scientific Instruments*, 81(1):1–8.

Benvenuti, C., Cazeneuve, J. M., Chiggiato, P., Cicoira, F., Santana, A. E., Johanek, V., Ruzinov, V., and Fraxedas, J. (1999). Novel route to extreme vacua: the non-evaporable getter thin film coatings. *Vacuum*, 53(1-2):219–225.

Bergeman, T., Erez, G., and Metcalf, H. J. (1987). Magnetostatic trapping fields for neutral atoms. *Physical Review A*, 35(4):1535–1546.

Berninger, M., Zenesini, A., Huang, B., Harm, W., Nägerl, H. C., Ferlaino, F., Grimm, R., Julienne, P. S., and Hutson, J. M. (2011). Universality of the three-body parameter for Efimov states in ultracold cesium. *Physical Review Letters*, 107(12):1–5.

Bloch, I., Dalibard, J., and Zwerger, W. (2008). Many-body physics with ultracold gases. *Reviews of Modern Physics*, 80(3):885–964.

Boesten, H. M., Tsai, C. C., Gardner, J. R., Heinzen, D. J., and Verhaar, B. J. (1997). Observation of a shape resonance in the collision of two cold ^{87}Rb atoms. *Physical Review A - Atomic, Molecular, and Optical Physics*, 55(1):636–640.

Botelho, S. S. and Sá de Melo, C. A. (2005). Quantum phase transition in the BCS-to-BEC evolution of p-wave Fermi gases. *Journal of Low Temperature Physics*, 140(5-6):409–428.

Bothwell, T., Kennedy, C. J., Aeppli, A., Kedar, D., Robinson, J. M., Oelker, E., Staron, A., and Ye, J. (2022). Resolving the gravitational redshift across a millimetre-scale atomic sample. *Nature*, 602(7897):420–424.

Bourdel, T., Khaykovich, L., Cubizolles, J., Zhang, J., Chevy, F., Teichmann, M., Tarruell, L., Kokkelmans, S. J., and Salomon, C. (2004). Experimental study of the BEC-BCS crossover region in lithium 6. *Physical Review Letters*, 93(5):3–6.

Breit, G. and Rabi, I. I. (1931). Measurement of nuclear spin. *Physical Review*, 38(11):2082–2083.

Brown, J. and Alan, C. (2003). *Rotational Spectroscopy of Diatomic Molecules*. Cambridge University Press.

Burchianti, A., Valtolina, G., Seman, J. A., Pace, E., De Pas, M., Inguscio, M., Zaccanti, M., and Roati, G. (2014). Efficient all-optical production of large Li 6 quantum gases using D1 gray-molasses cooling. *Physical Review A*, 90(4):1–5.

Castin, Y., Dalibard, J., and Cohen-Tannoudji, C. N. (1991). *The Limits of Sisyphus Cooling*. ETS Editrice, Pisa.

Cetina, M., Jag, M., Lous, R. S., Fritsche, I., Walraven, J. T., Grimm, R., Levinsen, J., Parish, M. M., Schmidt, R., Knap, M., and Demler, E. (2016). Ultrafast many-body interferometry of impurities coupled to a Fermi sea. *Science*, 354(6308):96–99.

Cheng, C. H. and Yip, S. K. (2005). Anisotropic fermi superfluid via p-wave Feshbach resonance. *Physical Review Letters*, 95(7):1–4.

Chevy, F., Van Kempen, E. G., Bourdel, T., Zhang, J., Khaykovich, L., Teichmann, M., Tarruell, L., Kokkelmans, S. J., and Salomon, C. (2005). Resonant scattering properties close to a p-wave Feshbach resonance. *Physical Review A*, 71(6):1–8.

Chin, C., Bartenstein, M., Altmeyer, A., Riedl, S., Jochim, S., Denschlag, J. H., and Grimm (2004). Observation of the pairing gap in a strongly interacting Fermi gas. *Science*, 305(5687):1128–1130.

Chin, C., Grimm, R., Julienne, P. S., and Tiesinga, E. (2010). Feshbach resonances in ultracold gases. *Reviews of Modern Physics*, 82(2):1225–1286.

Clementi, E. and Raimondi, D. L. (1963). Atomic screening constants from SCF functions. *The Journal of Chemical Physics*, 38(11):2686–2689.

Clementi, E., Raimondi, D. L., and Reinhardt, W. P. (1967). Atomic screening constants from SCF functions. II. Atoms with 37 to 86 electrons. *The Journal of Chemical Physics*, 47(4):1300–1307.

Courteille, P., Freeland, R. S., Heinzen, D. J., van Abeelen, F. A., and Verhaar, B. J. (1998). Observation of a feshbach resonance in cold atom scattering. *Physical Review Letters*, 81(1):69–72.

Cui, Y., Shen, C., Deng, M., Dong, S., Chen, C., Lü, R., Gao, B., Tey, M. K., and You, L. (2017). Observation of Broad d -Wave Feshbach Resonances with a Triplet Structure. *Physical Review Letters*, 119(20):1–5.

Cumby, T. D., Shewmon, R. A., Hu, M. G., Perreault, J. D., and Jin, D. S. (2013). Feshbach-molecule formation in a Bose-Fermi mixture. *Physical Review A*, 87(1):1–6.

Dalibard, J. (1999). *Collisional dynamics of ultra-cold atomic gases*. Proceedings of the International School of Physics "Enrico Fermi", Varena, volume 140 edition.

Dalibard, J. and Cohen-Tannoudji, C. N. (1989). Laser cooling below the Doppler limit by polarization gradients: simple theoretical models. *Journal of the Optical Society of America B*, 6(11):2023.

DeMarco, B., Bohn, J. L., Burke, J. P., Holland, M., and Jin, D. S. (1999). Measurement of p-Wave Threshold Law Using Evaporatively Cooled Fermionic Atoms. *Physical Review Letters*, 82(21):4208–4211.

Derevianko, A., Babb, J. F., and Dalgarno, A. (2001). High-precision calculations of van der Waals coefficients for heteronuclear alkali-metal dimers. *Physical Review A*, 63(5):527041–527044.

DeSalvo, B. J., Patel, K., Cai, G., and Chin, C. (2019). Observation of fermion-mediated interactions between bosonic atoms. *Nature*, 568(7750):61–64.

DeSalvo, B. J., Patel, K., Johansen, J., and Chin, C. (2017). Observation of a Degenerate Fermi Gas Trapped by a Bose-Einstein Condensate. *Physical Review Letters*, 119(23):1–5.

Dong, S., Cui, Y., Shen, C., Wu, Y., Tey, M. K., You, L., and Gao, B. (2016). Observation of broad p-wave Feshbach resonances in ultracold ^{85}Rb-^{87}Rb mixtures. *Physical Review A*, 94(6):1–7.

Drewsen, M., Laurent, P., Nadir, A., Santarelli, G., Clairon, A., Castin, Y., Grison, D., and Salomon, C. (1994). Investigation of sub-Doppler cooling effects in a cesium magneto-optical trap. *Applied Physics B Lasers and Optics*, 59(3):283–298.

Duarte, P. M., Hart, R. A., Hitchcock, J. M., Corcovilos, T. A., Yang, T. L., Reed, A., and Hulet, R. G. (2011). All-optical production of a lithium quantum gas using narrow-line laser cooling. *Physical Review A*, 84(6):1–4.

Duda, M., Chen, X.-Y., Bause, R., Schindewolf, A., Bloch, I., and Luo, X.-Y. (2022). Long-lived fermionic Feshbach molecules with tunable *p*-wave interactions. *arXiv*, pages 1–5.

Duine, R. A. and Stoof, H. T. (2003). Microscopic many-body theory of atomic Bose gases near a Feshbach resonance. *Journal of Optics B: Quantum and Semiclassical Optics*, 5(2).

Enss, T., Tran, B., Rautenberg, M., Gerken, M., Lippi, E., Drescher, M., Zhu, B., Weidemuller, M., and Salmhofer, M. (2020). Scattering of two heavy Fermi polarons: Resonances and quasibound states. *Physical Review A*, 102(6):1–7.

Esry, B. D., Greene, C. H., and Suno, H. (2002). Threshold laws for three-body recombination. *Physical Review A*, 65(1):107051–107054.

Esslinger, T., Sander, F., Weidemüller, M., Hemmerich, A., and Hänsch, T. W. (1996). Subrecoil Laser Cooling with Adiabatic Transfer. *Physical Review Letters*, 76(14):2432–2435.

Faraoni, G. (2014). *Nonlinear light propagation through a strongly interacting Rydberg gas. Master thesis, Universita di Pisa.* PhD thesis, University of Pisa, Pisa.

Fedichev, P. O., Kagan, Y., Shlyapnikov, G. V., and Walraven, J. T. (1996). Influence of nearly resonant light on the scattering length in low-temperature atomic gases. *Physical Review Letters*, 77(14):2913–2916.

Feshbach, H. (1958). Unified theory of nuclear reactions. *Annals of Physics*, 5(4):357–390.

Filzinger, M. (2018). *Improved manipulation and detection of an ultracold* ^{6}*Li-*^{133}*Cs mixture towards the investigation of the Bose polaron.* PhD thesis, Ruprecht-Karl Universität heidelberg, Heidelberg.

Foot, C. J. (2005). *Atomic Physics.* Oxford University Press.

Fritsche, I., Baroni, C., Dobler, E., Kirilov, E., Huang, B., Grimm, R., Bruun, G. M., and Massignan, P. (2021). Stability and breakdown of Fermi polarons in a strongly interacting Fermi-Bose mixture. *Physical Review A*, 103(5):1–15.

Fröhlich, H. (1954). Electrons in lattice fields. *Advances in Physics*, 3(11):325–361.

Fuchs, J., Ticknor, C., Dyke, P., Veeravalli, G., Kuhnle, E. D., Rowlands, W., Hannaford, P., and Vale, C. J. (2008). Binding energies of ^{6}Li p-wave Feshbach molecules. *Physical Review A*, 77(5):1–6.

Gaebler, J. P., Stewart, J. T., Bohn, J. L., and Jin, D. S. (2007). p-Wave feshbach molecules. *Physical Review Letters*, 98(20):1–4.

Gehm, M. E. (2003). Properties of Lithium-6. *Introductory Analysis*, pages 45–57.

Gerken, M. (2016). *Gray Molasses Cooling of Lithium-6 Towards a Degenerate Fermi Gas*. PhD thesis, Ruprecht-Karls Universität Heidelberg.

Gerken, M., Tran, B., Häfner, S., Tiemann, E., Zhu, B., and Weidemüller, M. (2019). Observation of dipolar splittings in high-resolution atom-loss spectroscopy of ^{6}Li p-wave Feshbach resonances. *Physical Review A*, 100(5):1–5.

Goyal, K., Reichenbach, I., and Deutsch, I. (2010). P-wave optical Feshbach resonances in ^{171}Yb. *Physical Review A*, 82(6):1–7.

Greiner, M., Regal, C. A., and Jin, D. S. (2003). Emergence of a molecular Bose-Einstein condensate from a Fermi gas. *Nature*, 426(6966):537–540.

Grier, A. T., Ferrier-Barbut, I., Rem, B. S., Delehaye, M., Khaykovich, L., Chevy, F., and Salomon, C. (2013). Λ-enhanced sub-Doppler cooling of lithium atoms in D1 gray molasses. *Physical Review A*, 87(6):1–8.

Grimm, R., Weidemüller, M., and Ovchinnikov, Y. B. (2000). Optical Dipole Traps for Neutral Atoms. *Advances in Atomic, Molecular and Optical Physics*, 42(C):95–170.

Grynberg, G. and Courtois, J. Y. (1994). Proposal for a magneto-optical lattice for trapping atoms in nearly-dark states. *Epl*, 27(1):41–46.

Günter, K., Stöferle, T., Moritz, H., Köhl, M., and Esslinger, T. (2005). P-Wave interactions in low-dimensional fermionic gases. *Physical Review Letters*, 95(23):1–4.

Guo, M., Zhu, B., Lu, B., Ye, X., Wang, F., Vexiau, R., Bouloufa-Maafa, N., Quéméner, G., Dulieu, O., and Wang, D. (2016). Creation of an Ultracold Gas of Ground-State Dipolar ^{23}Na ^{87}Rb Molecules. *Physical Review Letters*, 116(20):1–5.

Gurarie, V. and Radzihovsky, L. (2007). Resonantly paired fermionic superfluids. *Annals of Physics*, 322:2–119.

Gurarie, V., Radzihovsky, L., and Andreev, A. V. (2005). Quantum phase transitions across a p-wave feshbach resonance. *Physical Review Letters*, 94(23):1–4.

Häfner, S. (2017). *From two-body to many-body physics in an ultracold Bose-Fermi mixture of Li and Cs atoms*. PhD thesis, Ruprecht Karls Universität.

Han, D. J., Wolf, S., Oliver, S., McCormick, K. C., DePue, M. T., and Weiss, D. S. (2000). 3D Raman sideband cooling of cesium atoms at high density. *Physical Review Letters*, 85(4):724–727.

Harcken, H. (2021). The Earth's magnetic field at PTB.

Hazlett, E. L., Zhang, Y., Stites, R. W., and O'Hara, K. M. (2012). Realization of a resonant fermi gas with a large effective range. *Physical Review Letters*, 108(4):1–5.

He, J., dong Yang, B., jie Cheng, Y., cai Zhang, T., and min Wang, J. (2011). Extending the trapping lifetime of single atom in a microscopic far-off-resonance optical dipole trap. *Frontiers of Physics*, 6(3):262–270.

Heck, R. (2012). *All-Optical Formation of an Ultracold Gas of Fermionic Lithium Close to Quantum Degeneracy*. PhD thesis, Ruprecht-Karl Universität heidelberg.

Heo, M. S., Wang, T. T., Christensen, C. A., Rvachov, T. M., Cotta, D. A., Choi, J. H., Lee, Y. R., and Ketterle, W. (2012). Formation of ultracold fermionic Na-Li Feshbach molecules. *Physical Review A*, 86(2):3–6.

Hoffmann, D. K., Paintner, T., Limmer, W., Petrov, D. S., and Denschlag, J. H. (2018). Reaction kinetics of ultracold molecule-molecule collisions. *Nature Communications*, 9(1).

Horvath, M. S., Thomas, R., Tiesinga, E., Deb, A. B., and Kjærgaard, N. (2017). Above-threshold scattering about a Feshbach resonance for ultracold atoms in an optical collider. *Nature Communications*, 8(1):1–8.

Hu, M. G., Van De Graaff, M. J., Kedar, D., Corson, J. P., Cornell, E. A., and Jin, D. S. (2016). Bose Polarons in the Strongly Interacting Regime. *Physical Review Letters*, 117(5):1–6.

Hund, F. (1927). Zur Deutung der Bandenspektren. II. *Zeitschrift für Physik*, 46(11-12):814–825.

Hutson, J. M. and Soldán, P. (2006). Molecule formation in ultracold atomic gases. *International Reviews in Physical Chemistry*, 25(4):497–526.

Inada, Y., Horikoshi, M., Nakajima, S., Kuwata-Gonokami, M., Ueda, M., and Mukaiyama, T. (2008). Collisional properties of p-wave feshbach molecules. *Physical Review Letters*, 101(10):1–4.

Inouye, S., Andrews, M. R., Stenger, J., Mlesner, H. J., Stamper-Kurn, D. M., and Ketterle, W. (1998). Observation of Feshbach resonances in a Bose-Einstein condensate. *Nature*, 392(6672):151–154.

Jag, M., Zaccanti, M., Cetina, M., Lous, R. S., Schreck, F., Grimm, R., Petrov, D. S., and Levinsen, J. (2014). Observation of a strong atom-dimer attraction in a mass-imbalanced fermi-fermi mixture. *Physical Review Letters*, 112(7):1–5.

Jochain, C. J. (1983). *Quantum collision theory*. North-Holland Publ. Comp, Amsterdam, 3. ed. edition.

Jochim, S., Bartenstein, M., Altmeyer, A., Hendl, G., Riedl, S., Chin, C., Denschlag, J. H., and Grimm, R. (2003). Observation of bose-einstein condensation of molecules. *Physical Review Letters*, 302(5653):2101–2103.

Johansen, J., De Salvo, B. J., Patel, K., and Chin, C. (2017). Testing universality of Efimov physics across broad and narrow Feshbach resonances. *Nature Physics*, 13(8):731–735.

Johnson, B. R. (1977). New numerical methods applied to solving the one-dimensional eigenvalue problem. *The Journal of Chemical Physics*, 67(9):4086–4093.

Jones, K. M., Tiesinga, E., Lett, P. D., and Julienne, P. S. (2006). Ultracold photoassociation spectroscopy: Long-range molecules and atomic scattering. *Reviews of Modern Physics*, 78(2):483–535.

Jørgensen, N. B., Wacker, L., Skalmstang, K. T., Parish, M. M., Levinsen, J., Christensen, R. S., Bruun, G. M., and Arlt, J. J. (2016). Observation of Attractive and Repulsive Polarons in a Bose-Einstein Condensate. *Physical Review Letters*, 117(5):1–6.

Kerman, A. J., Vuletić, V., Chin, C., and Chu, S. (2000). Beyond optical molasses: 3D raman sideband cooling of atomic cesium to high phase-space density. *Physical Review Letters*, 84(3):439–442.

Ketterle, W. and Druten, N. J. (1996). Evaporative Cooling of Trapped Atoms. *Advances in Atomic, Molecular and Optical Physics*, 37(C):181–236.

Ketterle, W., Durfee, D. S., and Stamper-Kurn, D. M. (1999). Making, probing and understanding Bose-Einstein condensates. *arXiv*.

Ketterle, W. and Zwierlein, M. W. (2008). Making, probing and understanding ultracold Fermi gases. *Rivista del Nuovo Cimento*, 31(5-6):247–422.

Kinast, J., Hemmer, S. L., Gehm, M. E., Turlapov, A., and Thomas, J. E. (2004). Evidence for superfluidity in a resonantly interacting Fermi gas. *Physical Review Letters*, 92(15):2–5.

Klempt, C., Henninger, T., Topic, O., Scherer, M., Kattner, L., Tiemann, E., Ertmer, W., and Arlt, J. J. (2008). Radio-frequency association of heteronuclear Feshbach molecules. *Physical Review A*, 78(6):1–4.

Knoop, S., Ferlaino, F., Mark, M., Berninger, M., Schöbel, H., Nägerl, H. C., and Grimm, R. (2009). Observation of an Efimov-like trimer resonance in ultracold atom-dimer scattering. *Nature Physics*, 5(3):227–230.

Köhler, T., Góral, K., and Julienne, P. S. (2006). Production of cold molecules via magnetically tunable Feshbach resonances. *Reviews of Modern Physics*, 78(4):1311–1361.

Kohstall, C., Zaccanti, M., Jag, M., Trenkwalder, A., Massignan, P., Bruun, G. M., Schreck, F., and Grimm, R. (2012). Metastability and coherence of repulsive polarons in a strongly interacting Fermi mixture. *Nature*, 485(7400):615–618.

Köppinger, M. P., McCarron, D. J., Jenkin, D. L., Molony, P. K., Cho, H. W., Cornish, S. L., Le Sueur, C. R., Blackley, C. L., and Hutson, J. M. (2014). Production of optically trapped ^{87}RbCs Feshbach molecules. *Physical Review A*, 89(3):31–33.

Kotochigova, S., Tiesinga, E., and Julienne, P. S. (2001). Relativistic ab initio treatment of the second-order spin-orbit splitting of the a $3\Sigma_u^+$ potential of rubidium and cesium dimers. *Physical Review A*, 63(1):012517–012511.

Kraemer, T., Mark, M., Waldburger, P., Danzl, J. G., Chin, C., Engeser, B., Lange, A. D., Pilch, K., Jaakkola, A., Nägerl, H. C., and Grimm, R. (2006). Evidence for Efimov quantum states in an ultracold gas of caesium atoms. *Nature*, 440(7082):315–318.

Landau, L. D. and Lifshitz, E. M. (1965). *Quantum Mechanics: Non-Relativistic Theory*. Pergamon Press Ltd.

Le Roy, R. (1974). Long-Range Potential Coefficients From RKR Turning Points: C_6 and C_8 for $B(3\Sigma_{Ou}^+)$-State Cl_2, Br_2, and I_2. *Canadian Journal of Physics*, 52(3).

Lefebvre-Brion H., F. R. (1986). *Perturbations in the spectra of diatomic molecules*. United States: Academic Press Inc.

Lett, P. D., Watts, R. N., Westbrook, C. I., Phillips, W. D., Gould, P. L., and Metcalf, H. J. (1988). Observation of atoms laser cooled below the doppler limit. *Physical Review Letters*, 61(2):169–172.

Levinsen, J., Massignan, P., Chevy, F., and Lobo, C. (2012). P-wave polaron. *Physical Review Letters*, 109(7).

Li, J., Liu, J., Luo, L., and Gao, B. (2018). Three-Body Recombination near a Narrow Feshbach Resonance in Li 6. *Physical Review Letters*, 120(19):193402.

Lompe, T., Ottenstein, T. B., Serwane, F., Wenz, A. N., Zürn, G., and Jochim, S. (2010). Radio-Frequency Association of Efimov Trimers. *Science*, 330(November):940–944.

Luciuk, C., Trotzky, S., Smale, S., Yu, Z., Zhang, S., and Thywissen, J. H. (2016). Evidence for universal relations describing a gas with p-wave interactions. *Nature Physics*, 12(6):599–605.

Luiten, O. J., Reynolds, M. W., and Walraven, J. T. (1996). Kinetic theory of the evaporative cooling of a trapped gas. *Physical Review A*, 53(1):381–389.

Maekawa, S., Valenzuela, S. O., Saitoh, E., and Kimura, T. (2012). *Spin Current*. Oxford University Press.

Maier, R. A., Marzok, C., Zimmermann, C., and Courteille, P. W. (2010). Radio-frequency spectroscopy of Li6 p-wave molecules: Towards photoemission spectroscopy of a p-wave superfluid. *Physical Review A*, 81(6).

Marcum, A. S., Fonta, F. R., Ismail, A. M., and O'Hara, K. M. (2020). Suppression of Three-Body Loss Near a p-Wave Resonance Due to Quasi-1D Confinement. pages 1–6.

Marinescu, M. and Dalgarno, A. (1995). Dispersion forces and long-range electronic transition dipole moments of alkali-metal dimer excited states. *Physical Review A*, 52(1):311–328.

Mathew, R. and Tiesinga, E. (2013). Controlling the group velocity of colliding atomic Bose-Einstein condensates with Feshbach resonances. *Physical Review A*, 87(5):1–5.

Mathey, L., Tiesinga, E., Julienne, P. S., and Clark, C. W. (2009). Collisional cooling of ultracold-atom ensembles using Feshbach resonances. *Physical Review A*, 80(3):1–4.

McKay, D. C., Jervis, D., Fine, D. J., Simpson-Porco, J. W., Edge, G. J., and Thywissen, J. H. (2011). Low-temperature high-density magneto-optical trapping of potassium using the open 4S→5P transition at 405 nm. *Physical Review A*, 84(6):1–8.

Mies, F. H. and Raoult, M. (2000). Analysis of threshold effects in ultracold atomic collisions. *Physical Review A*, 62(1):19.

Mies, F. H., Williams, C. J., Julienne, P. S., and Krauss, M. (1996). Estimating bounds on collisional relaxation rates of spin-polarized ^{87}Rb atoms at ultracold temperatures. *Journal of Research of the National Institute of Standards and Technology*, 101(4):521–535.

Moerdijk, A. J., Verhaar, B. J., and Axelsson, A. (1995). Resonances in ultracold collisions of ^{6}Li, ^{7}Li, and ^{23}Na. *Physical Review A*, 51(6):4852–4861.

Molony, P. K., Gregory, P. D., Ji, Z., Lu, B., Köppinger, M. P., Le Sueur, C. R., Blackley, C. L., Hutson, J. M., and Cornish, S. L. (2014). Creation of ultracold ^{87}Rb ^{133}Cs molecules in the rovibrational ground state. *Physical Review Letters*, 113(25):1–5.

Naidon, P. and Endo, S. (2017). Efimov physics: a review. *Reports on Progress in Physics*, 80(5).

Nakasuji, T., Yoshida, J., and Mukaiyama, T. (2013). Experimental determination of p-wave scattering parameters in ultracold ^{6}Li atoms. *Physical Review A*, 88(1):1–5.

Neiczer, M. M. (2018). *Efficient creation of a molecular Bose-Einstein condensate of Lithium-6 using a spatially modulated dipole trap*. PhD thesis, Ruprecht Karls Universität, Heidelberg.

Ni, K. K., Ospelkaus, S., De Miranda, M. H., Pe'er, A., Neyenhuis, B., Zirbel, J. J., Kotochigova, S., Julienne, P. S., Jin, D. S., and Ye, J. (2008). A high phase-space-density gas of polar molecules. *Science*, 322(5899):231–235.

Nishida, Y. (2012). Impossibility of the Efimov effect for p-wave interactions. *Physical Review A*, 86(1):12710–12711.

Nuske, M., Tiesinga, E., and Mathey, L. (2015). Optimization of collisional Feshbach cooling of an ultracold nondegenerate gas. *Physical Review A*, 91(4):1–6.

Ospelkaus, C., Ospelkaus, S., Humbert, L., Ernst, P., Sengstock, K., and Bongs, K. (2006). Ultracold heteronuclear molecules in a 3D optical lattice. *Physical Review Letters*, 97(12):2–5.

Page, D., Prakash, M., Lattimer, J. M., and Steiner, A. W. (2011). Rapid cooling of the neutron star in cassiopeia a triggered by neutron superfluidity in dense matter. *Physical Review Letters*, 106(8):1–4.

Papoff, F., Mauri, F., and Arimondo, E. (1992). Transient velocity-selective coherent population trapping in one dimension. *Journal of the Optical Society of America B*, 9(3):321–331.

Park, J. W., Will, S. A., and Zwierlein, M. W. (2015). Ultracold Dipolar Gas of Fermionic ^{23}Na-^{40}K Molecules in Their Absolute Ground State. *Physical Review Letters*, 114(20):1–5.

Park, J. W., Wu, C. H., Santiago, I., Tiecke, T. G., Will, S., Ahmadi, P., and Zwierlein, M. W. (2012). Quantum degenerate Bose-Fermi mixture of chemically different atomic species with widely tunable interactions. *Physical Review A*, 85(5):1–5.

Partridge, G. B., Strecker, K. E., Kamar, R. I., Jack, M. W., and Hulet, R. G. (2005). Molecular probe of pairing in the BEC-BCS crossover. *Physical Review Letters*, 95(2):8–11.

Pashov, A., Docenko, O., Tamanis, M., Ferber, R., Knoeckel, H., and Tiemann, E. (2007). The coupling of the $X^1\Sigma^+$ and $a^3\Sigma^+$ states of KRb. *Physical Review A*, 76(022511):1–10.

Peng, P., Zhang, R., Huang, L., Li, D., Meng, Z., Wang, P., Zhai, H., Zhang, P., and Zhang, J. (2018). Universal feature in optical control of a p -wave Feshbach resonance. *Physical Review A*, 97(1):1–9.

Peng, S., Liu, H., Li, J., and Luo, L. (2021). Cooling a Fermi gas with three-body recombination near a narrow Feshbach resonance. *arXiv*, pages 1–8.

Petrov, D. S. (2003). Three-body problem in Fermi gases with short-range interparticle interaction. *Physical Review A*, 67(1):4.

Petrov, D. S., Salomon, C., and Shlyapnikov, G. V. (2004). Weakly bound dimers of fermionic atoms. *Physical Review Letters*, 93(9):1–4.

Phillips, W. D. and Metcalf, H. J. (1982). Laser Deceleration of an Atomic Beam. *Physical Review Letters*, 48(9):596–599.

Pilch, K., Lange, A. D., Prantner, A., Kerner, G., Ferlaino, F., Nägerl, H. C., and Grimm, R. (2009). Observation of interspecies Feshbach resonances in an ultracold Rb-Cs mixture. *Physical Review A*, 79(4):1–7.

Pinkse, P. W., Mosk, A., Weidemüller, M., Reynolds, M. W., Hijmans, T. W., and Walraven, J. T. (1997). Adiabatically changing the phase-space density of a trapped bose gas. *Physical Review Letters*, 78(6):990–993.

Pires, R. (2014). *Efmov Resonances in an Ultracold Mixture with Extreme Mass Imbalance*. Phd-thesis, Ruprecht Karls Universität, Heidelberg.

Pires, R., Repp, M., Ulmanis, J., Kuhnle, E. D., Weidemüller, M., Tiecke, T. G., Greene, C. H., Ruzic, B. P., Bohn, J. L., and Tiemann, E. (2014a). Analyzing Feshbach resonances: A Li 6 - Cs 133 case study. *Physical Review A*, 90(1):1–14.

Pires, R., Ulmanis, J., Häfner, S., Repp, M., Arias, A., Kuhnle, E. D., and Weidemüller, M. (2014b). Observation of Efimov resonances in a mixture with extreme mass imbalance. *Physical Review Letters*, 112(25):1–5.

Regal, C. A., Ticknor, C., Bohn, J. L., and Jin, D. S. (2003). Creation of ultracold molecules from a Fermi gas of atoms. *Nature*, 424(6944):47–50.

Rentrop, T., Trautmann, A., Olivares, F. A., Jendrzejewski, F., Komnik, A., and Oberthaler, M. K. (2016). Observation of the phononic Lamb shift with a synthetic vacuum. *Physical Review X*, 6(4):1–10.

Repp, M. (2013). *Interspecies Feshbach Resonances in an Ultracold, Optically Trapped Bose-Fermi Mixture of Cesium and Lithium*. Phd-thesis, Ruprecht Karls Universität Heidelberg, Heidelberg.

Repp, M., Pires, R., Ulmanis, J., Heck, R., Kuhnle, E. D., Weidemüller, M., and Tiemann, E. (2013). Observation of interspecies 6Li-133Cs Feshbach resonances. *Physical Review A*, 87(1):1–5.

Rio Fernandes, D., Sievers, F., Kretzschmar, N., Wu, S., Salomon, C., and Chevy, F. (2012). Sub-Doppler laser cooling of fermionic 40K atoms in three-dimensional gray optical molasses. *Epl*, 100(6).

Roy, R., Green, A., Bowler, R., and Gupta, S. (2016). Rapid cooling to quantum degeneracy in dynamically shaped atom traps. *Physical Review A*, 93(4):1–7.

Sakurai, J. J. and Napolitano, J. (1994). *Modern Quantum Mechanics*. University Press, Cambridge.

Sawyer, B. J., Horvath, M. S., Tiesinga, E., Deb, A. B., and Kjærgaard, N. (2017). Dispersive optical detection of magnetic Feshbach resonances in ultracold gases. *Physical Review A*, 96(2):1–10.

Schmidt, M., Hammer, H. W., Hammer, H. W., Platter, L., and Platter, L. (2020). Three-body losses of a polarized Fermi gas near a p -wave Feshbach resonance in effective field theory. *Physical Review A*, 101(6):62702.

Schönhals, A. (2013). *Imaging of ultracold Cesium atoms at high magnetic field*. PhD thesis, Ruprecht Karls Universität, Heidelberg.

Schunck, C. H., Zwierlein, M. W., Stan, C. A., Raupach, S. M., Ketterle, W., Simoni, A., Tiesinga, E., Williams, C. J., and Julienne, P. S. (2005). Feshbach resonances in fermionic Li6. *Physical Review A*, 71(4):1–4.

Schünemann, U., Engler, H., Zielonkowski, M., Weidemüller, M., and Grimm, R. (1998). Magneto-optic trapping of lithium using semiconductor lasers. *Optics Communications*, 158(1-6):263–272.

Shternin, P. S., Yakovlev, D. G., Heinke, C. O., Ho, W. C., and Patnaude, D. J. (2011). Cooling neutron star in the Cassiopeia A supernova remnant: Evidence for superfluidity in the core. *Monthly Notices of the Royal Astronomical Society: Letters*, 412(1):108–112.

Stamper-Kurn, D. M., Miesner, H. J., Chikkatur, A. P., Inouye, S., Stenger, J., and Ketterle, W. (1998). Reversible formation of a bose-einstein condensate. *Physical Review Letters*, 81(11):2194–2197.

Stan, C. A. and Ketterle, W. (2005). Multiple species atom source for laser-cooling experiments. *Review of Scientific Instruments*, 76(6).

Steck, D. a. (2002). Cesium D Line Data Cesium Physical and Optical Properties. *Structure*, 4710(7):1–29.

Stoof, H. T., Koelman, J. M., and Verhaar, B. J. (1988). Spin-exchange and dipole relaxation rates in atomic hydrogen: Rigorous and simplified calculations. *Physical Review B*, 38(7):4688–4697.

Strandberg, M. W. P. and Tinkham, M. (1955). Theory of the Fine Structure of the Molecular. *Physical Review*, 97(4):937–966.

Strauss, C., Takekoshi, T., Lang, F., Winkler, K., Grimm, R., and Hecker Denschlag, J. (2010). Hyperfine, rotational, and vibrational structure of the a 3Σ +u state of 87Rb 2. *Physical Review A*, 82(5):1–12.

Sun, M. and Cui, X. (2017). Enhancing the Efimov correlation in Bose polarons with large mass imbalance. *Physical Review A*, 96(2):1–7.

Sun, M., Zhai, H., and Cui, X. (2017). Visualizing the Efimov Correlation in Bose Polarons. *Physical Review Letters*, 119(1):1–6.

Suno, H., Esry, B. D., and Greene, C. H. (2003). Recombination of Three Ultracold Fermionic Atoms. *Physical Review Letters*, 90(5):4.

Takekoshi, T., Reichsöllner, L., Schindewolf, A., Hutson, J. M., Le Sueur, C. R., Dulieu, O., Ferlaino, F., Grimm, R., and Nägerl, H. C. (2014). Ultracold dense samples of

dipolar RbCs molecules in the rovibrational and hyperfine ground state. *Physical Review Letters*, 113(20):1–5.

Theis, M., Thalhammer, G., Winkler, K., Hellwig, M., Ruff, G., Grimm, R., and Denschlag, J. H. (2004). Tuning the scattering length with an optically induced feshbach resonance. *Physical Review Letters*, 93(12):10–13.

Ticknor, C., Regal, C. A., Jin, D. S., and Bohn, J. L. (2004). Multiplet structure of Feshbach resonances in nonzero partial waves. *Physical Review A*, 69(4):1–6.

Timmermans, E., Tommasini, P., Hussein, M., and Kerman, A. (1999). Feshbach resonances in atomic Bose-Einstein condensates. *Physics Report*, 315(1-4):199–230.

Tischer, R. (1967). Notizen. *Zeitrschrift für Naturforschung*, 22a(1711).

Top, F. Ç., Margalit, Y., and Ketterle, W. (2021). Spin-polarized fermions with -wave interactions. *Physical Review A*, 104(4):1–9.

Tran, B., Rautenberg, M., Gerken, M., Lippi, E., Zhu, B., Ulmanis, J., Drescher, M., Salmhofer, M., Enss, T., and Weidemüller, M. (2021). Fermions Meet Two Bosons—the Heteronuclear Efimov Effect Revisited. *Brazilian Journal of Physics*, 51(2):316–322.

Treutlein, P., Chu, K. Y., and Chu, S. (2001). High-brightness atom source for atomic fountains. *Physical Review A*, 63(5):514011–514014.

Tung, S. K., Jiménez-García, K., Johansen, J., Parker, C. V., and Chin, C. (2014). Geometric scaling of efimov states in a ^{6}Li-^{133}Cs mixture. *Physical Review Letters*, 113(24):1–5.

Tung, S. K., Parker, C., Johansen, J., Chin, C., Wang, Y., and Julienne, P. S. (2013). Ultracold mixtures of atomic ^{6}Li and ^{133}Cs with tunable interactions. *Physical Review A*, 87(1):1–4.

Ulmanis, J. (2017). *Heteronuclear Efimov Scenario in Ultracold Quantum Gases*. PhD thesis, Ruprecht-Karls Universität Heidelberg.

Ulmanis, J., Häfner, S., Pires, R., Kuhnle, E. D., Weidemüller, M., and Tiemann, E. (2015). Universality of weakly bound dimers and Efimov trimers close to Li-Cs Feshbach resonances. *New Journal of Physics*, 17.

Ulmanis, J., Häfner, S., Pires, R., Werner, F., Petrov, D. S., Kuhnle, E. D., and Weidemüller, M. (2016). Universal three-body recombination and Efimov resonances in an ultracold Li-Cs mixture. *Physical Review A*, 93(2):1–7.

Van Vleck, J. H. (1929). On σ-type doubling and electron spin in the spectra of diatomic molecules. *Physical Review*, 33(4):467–506.

Van Vleck, J. H. (1951). The coupling of angular momentum vectors in molecules. *Reviews of Modern Physics*, 23(3):213–227.

Vuletic, V., Chin, C., Kerman, A. J., and Chu, S. (1998). Degenerate raman sideband cooling of trapped cesium atoms at very high atomic densities. *Physical Review Letters*, 81(26):5768–5771.

Walraven, J. T. (2010). *Elements of Quantum Gases: Thermodynamic and Collisional Properties of Trapped Atomic Gases*. University of Amsterdam.

Wang, F., He, X., Li, X., Zhu, B., Chen, J., and Wang, D. (2015). Formation of ultracold NaRb Feshbach molecules. *New Journal of Physics*, 17.

Wang, P. J., Fu, Z. K., Chai, S. J., and Zhang, J. (2011). Feshbach resonances in an ultracold mixture of 87Rb and 40K. *Chinese Physics B*, 20(10).

Wang, T. T., Heo, M. S., Rvachov, T. M., Cotta, D. A., and Ketterle, W. (2013). Deviation from universality in collisions of ultracold $^6Li_2$ molecules. *Physical Review Letters*, 110(17):1–5.

Waseem, M., Saito, T., Yoshida, J., and Mukaiyama, T. (2017). Two-body relaxation in a Fermi gas at a p-wave Feshbach resonance. *Physical Review A*, 96(6):1–5.

Waseem, M., Yoshida, J., Saito, T., and Mukaiyama, T. (2018). Unitarity-limited behavior of three-body collisions in a p -wave interacting Fermi gas. *Physical Review A*, 98(2):1–5.

Waseem, M., Yoshida, J., Saito, T., and Mukaiyama, T. (2019). Quantitative analysis of p-wave three-body losses via a cascade process. *Physical Review A*, 99(5):1–6.

Waseem, M., Zhang, Z., Yoshida, J., Hattori, K., Saito, T., and Mukaiyama, T. (2016). Creation of p-wave Feshbach molecules in selected angular momentum states using an optical lattice. *Journal of Physics B: Atomic, Molecular and Optical Physics*, 49(20).

Weber, T. (2003). *Bose-Einstein condensation of optically trapped cesium*. PhD thesis, Universität Innsbruck, Innsbruck.

Weber, T., Herbig, J., Mark, M., Nägerl, H. C., and Grimm, R. (2003). Bose-Einstein condensation of cesium. *Science*, 299(5604):232–235.

Weidemüller, M., Esslinger, T., Ol'shanii, M. A., Hemmerich, A., and Hänsch, T. W. (1994). A novel scheme for efficient cooling below the photon recoil limit. *Epl*, 27(2):109–114.

Weidemüller, M. and Zimmermann, C. (2003). *Interactions in Ultracold Gases*. WILEY-VCH Verlag Berin GmbH.

Wigner, E. P. (1948). On the behavior of cross sections near thresholds. *Physical Review*, 73(9):1002–1009.

Wu, C. H., Park, J. W., Ahmadi, P., Will, S., and Zwierlein, M. W. (2012). Ultracold fermionic Feshbach molecules of ^{23}Na-^{40}K. *Physical Review Letters*, 109(8):18–21.

Yan, Z. Z., Ni, Y., Robens, C., and Zwierlein, M. W. (2020). Bose polarons near quantum criticality. *Science*, 368(6487):190–194.

Ye, X., Guo, M., González-Martínez, M. L., Quéméner, G., and Wang, D. (2018). Collisions of ultracold ^{23}Na-^{87}Rb molecules with controlled chemical reactivities. *Science Advances*, 4(1):1–7.

Yoshida, J., Saito, T., Waseem, M., Hattori, K., and Mukaiyama, T. (2018). Scaling Law for Three-Body Collisions of Identical Fermions with p -Wave Interactions. *Physical Review Letters*, 120(13):133401.

Zhang, J., Van Kempen, E. G., Bourdel, T., Khaykovich, L., Cubizolles, J., Chevy, F., Teichmann, M., Tarruell, L., Kokkelmans, S. J., and Salomon, C. (2004). P-wave Feshbach resonances of ultracold ^{6}Li. *Physical Review A*, 70(3):4–7.

Zhou, L. and Cui, X. (2017). Stretching p-wave molecules by transverse confinements. *Physical Review A*, 96(3):1–5.

Zhu, B., Stephan, H., Tran, B., Gerken, M., Tiemann, E., and Weidemüller, M. (2021a). Higher partial-wave Feshbach resonances in an ultracold ^{6}Li- ^{133}Cs mixture. *arXiv*, pages 1–12.

Zhu, B., Stephan, H., Tran, B., Gerken, M., Tiemann, E., and Weidemüller, M. (2021b). Observation of spin-rotation coupling in p -wave Feshbach resonances. *arXiv*.

Zürn, G., Lompe, T., Wenz, A. N., Jochim, S., Julienne, P. S., and Hutson, J. M. (2013). Precise characterization of ^{6}Li Feshbach resonances using trap-sideband-resolved RF spectroscopy of weakly bound molecules. *Physical Review Letters*, 110(13):1–5.

Zwierlein, M. W., Abo-Shaeer, J. R., Schirotzek, A., Schunck, C. H., and Ketterle, W. (2005). Vortices and superfluidity in a strongly interacting Fermi gas. *Nature*, 435(7045):1047–1051.

Zwierlein, M. W., Stan, C. A., Schunck, C. H., Raupach, S. M., Gupta, S., Hadzibabic, Z., and Ketterle, W. (2003). Observation of bose-einstein condensation of molecules. *Physical Review Letters*, 91(25):1–4.

Acknowledgments

At this point I would like to thank everyone that supported me and this thesis as well as any other kind of support during this process. This thesis was hard work for a lot of people and it would not have been possible without you. Special thanks go to

Prof. Matthias Weidemüller. Thank you very much for taking me under your wings back in 2014 when my journey in your group started. Thank you for the possibility to work in this exciting and very solid environment with the best infrastructure of laboratories, knowledge and science exchange one could hope for. Thank you especially for your understanding and supporting moments outside of science!

Prof. Selim Jochim. Thank you for reviewing this thesis and thank you for the great possibility of exchange between your group and ours. Discussions with you are always quite fun and inspiring!

Binh Tran and Eleonora Lippi. Thank you for all your hard work that you put into this experiment and the group that also benefited this thesis a lot! This thesis would have looked much worse without your help and dedication! Thanks!

Prof. Lauriane Chomaz. Thank you for the new energy and perspectives you brought with you. I benefited a lot from our discussions and your input.

Bing Zhu, Gerhard Zürn and Stephan Häfner. Thanks for everything you taught me with patience and enthusiasm and all the advice I could rely on. You made this group an environment I (obviously) saw myself staying in!

Markus Neiczer, Melina Filzinger, Jonas Matthies, Lauritz Klaus, Michael Rautenberg, Robert Freund for your great Master theses that contributed a lot to the progress we made during my time at this experiment. New energy is always challenging, but always proved to be beneficial for our experiment!

Kilian Welz. You are down here but you got your own paragraph! Thanks for your work and contribution on the p-wave loss project. Your very pleasant and attentive way made this project exciting end enjoyable!

Michael Rautenberg and Tobias Krom for helping on the last steps of this journey. I wish you all the best for the future of this experiment!

Juris Ulmanis, Eva Kuhnle and Rico Pires. A pretty long time ago but the environment and the machine you left inspired me to continue in this group!

Rydberg, Haitraps and Lithium-6 group. Thanks for making this work environment so outstanding. Always open doors and ears for discussions and questions with pretty motivated and smart people. And thanks for letting me beat you at Kicker back in the pre-Covid days (That holds for everyone in this group)!

Tilman Enss, Moritz Drescher and Manfred Salmhofer. Thank you for the exciting collaboration within the SFB. I learned a lot from the discussions and the work on the proposal!

Claudia Krämer, the PI-backoffice and the HGSFP office. Thank you for your very kind and patient ways. You kept my back from so much paperwork and organization that I could actually work on physics!

Dominic Litsch and the Mechanical and Electronic workshop. Thank you for the great work that made it possible to build and expand this experiment!

My Heidelberg Physics crew. I'm so very thankful for this great group of people that accompanied my physics journey in Heidelberg. This thesis builds on all the late night work at KIP. Also thanks to all my friends all over the place that supported me with distraction, advice and counsel. If you read this and you are not into physics, chances are high I'm talking about you!

Leonie Adelmann for all the silly that keeps me sane!

My parents, sister and brother for all your support and an infinitely strong safety net I will always rely on!

Thanks also to everyone I didn't mention!